Multi-axis Wire Arc Additive Manufacturing Using Optimized Fabrication Sequence

Exploring Challenges In Implementation And Experimental Validation Of Fabrication Sequence Optimization For Distortion Minimization In Multi-axis Wire Arc Additive Manufacturing

Adhiraj Ravindra Pimpalkar

Department of Precision and Microsystems Engineering

Multi-axis Wire Arc Additive Manufacturing Using Optimized Fabrication Sequence: Exploring Challenges In Implementation And Experimental Validation Of Fabrication Sequence Optimization For Distortion Minimization in Multi-axis Wire Arc Additive Manufacturing

Adhiraj Ravindra Pimpalkar

Report no   : 2024.026
Coach   : Dr. ir. Vibhas Mishra
Professor   : Dr. Can Ayas, Dr. Jun Wu
Specialisation : Computational Design and Mechanics
Type of report : Master Thesis
Date   : 31st May 2024

TUDelft
Delft
University of
Technology

Challenge the future

MULTI-AXIS WIRE ARC ADDITIVE MANUFACTURING USING OPTIMIZED FABRICATION SEQUENCE

EXPLORING CHALLENGES IN IMPLEMENTATION AND EXPERIMENTAL VALIDATION OF FABRICATION SEQUENCE OPTIMIZATION FOR DISTORTION MINIMIZATION IN MULTI-AXIS WIRE ARC ADDITIVE MANUFACTURING

Master Thesis

Submitted to the Delft University of Technology
in partial fulfillment of the requirements for the degree of
Master of Science in Mechanical Engineering

by

Adhiraj Ravindra PIMPALKAR

Student Number: 5303850
Track: High-Tech Engineering
Focus: Computational Design and Mechanics (CDM)
Department of Precision and Microsystem Engineering

Thesis Committee:	Dr. Can ayas	Supervisor
	Dr. Jun Wu	Supervisor
	Dr. ir. Vibhas Mishra	Daily Supervisor
	Dr. Marcel Hermans	External Examinar

May 2024

An electronic version of this dissertation is available at
http://repository.tudelft.nl/

TUDelft Delft
University of
Technology

ABSTRACT

Wire arc additive manufacturing (WAAM) is attributed to higher material deposition rates and medium to large build volumes. Integration of multi-axis (more than three) material deposition kinematics in WAAM can bring a paradigm shift in the metal additive manufacturing industry. The material build-up mechanism employing directed energy deposition results in localized melting and solidification of feeding wire making the fabricated structure inherently prone to deposition defects such as dimensional distortion, residual stresses, solidification cracking, and porosity. Optimization of welding process parameters can improve cracking and porosity behavior. However, the problem of distortion is inevitable, and current mitigation strategies rely on post-processing or symmetric material deposition; while the former decreases the effectiveness of WAAM and increases costs, the latter could only be implemented for specific parts. Tackling this problem with the help of computational design tools is a recent approach, and Fabrication Sequence Optimization dictating material deposition is numerically predicted to limit the extent of the distortion effectively compared to conventional planar horizontal deposition; however, this still lacks experimental validation. This research presents a series of fabrication experiments using Al5356 Aluminum-magnesium alloy wire in a 6-axis robotic WAAM setup in two parts: (1) Process parameters identification for optimal bead characteristics for Al5356 wire, (2) Fabrication of single bead multi-layered thin-walled shell structures using planar and optimized material deposition. A digital image correlation-based non-contact in-situ distortion measurement setup is constructed to analyze strain development during fabrication process and 3D scanning of fabricated structures is performed to estimate dimensional deviation. The experimental findings revealed an improvement in geometrical formation and a qualitative indication of distortion minimization with an optimized fabrication sequence.

ACKNOWLEDGEMENTS

CONTENTS

1

INTRODUCTION

1.1. BACKGROUND

Additive manufacturing (AM) is a generalized term that refers to technologies that successively join material to create physical objects according to the specifications of 3D model data [1]. Additive manufacturing is essentially a 2.5D process, in which material is added to a plane configuring a cross-section of the structure being built, and such planes are stacked over each other to realize the final 3D structure [2]. Despite the numerous advantages of this method [3], stacking of planar layers introduces the need for support structures in certain cases for overhanging features, Stair-case patterns over curved features, Dimensional distortion/ Residual stresses, and Anisotropic mechanical/thermal properties. Mitigation of these issues demands the use of post-processing [4] including subtractive manufacturing, heat, and surface treatment. Post-processing drives up overall costs, material wastage forcing the engineer to make a trade-off between cost and quality. These challenges can be completely or partially addressed with the help of *"Multi-axis Additive Manufacturing"*[5]. However, when it comes to metal AM [6] regardless of the nature of the raw material (powder or wire) the capital cost of the AM process increases drastically and the use of such metal AM process is often unjustified. Multi-axis metal AM is a solution to these challenges, where with the incorporation of additional axes, the machine becomes capable of producing complex components in reduced time and cost thus its use is justified. The work of Milewski et al.[7] is one of the earliest demonstrations of multi-axis metal AM. A fully dense stainless steel hemispherical object is fabricated by depositing metal along a helical tool path using a 5-axis CNC machine.

(a) Pedestrian Bridge Fabrication [8]　　　　(b) Suspension Strut Support for Automotive Application [9]
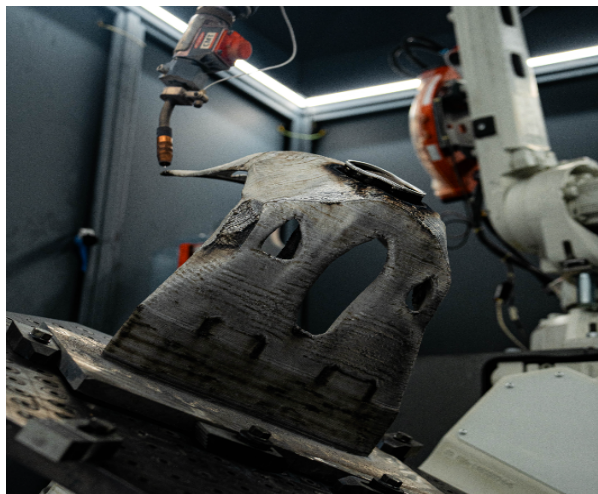
Figure 1.1: Multi-axis wire arc additive manufacturing for industrial applications

1

1

Directed energy deposition-based wire arc additive manufacturing (WAAM) process offers high material deposition (up to 10 kg/hr [10]) and shorter lead times, furthermore, integration of multi-axis deposition using advanced robotic systems improves fabrication flexibility [8], [11]. It demonstrates considerable potential in the production of expansive metallic components commonly observed within the maritime [12], aerospace [13], and automotive [14] industries.

1.2. MOTIVATION AND PROBLEM STATEMENT

In WAAM, a localized heat input in the form of an electric arc between an electrode and the substrate is used to melt the feedstock wire. It is then added to the molten metal pool and upon solidification at the melt pool boundary, the process is repeated to deposit the material in a layer-wise manner to construct the final part. Uneven thermal expansion and solidification during the process acquire special characteristics of distortion/warpage, residual stresses (often manifesting in the form of distortion), and defects in structures fabricated using WAAM as shown in Fig.1.2. These characteristics are unwanted and pose a major quality control issue, unfortunately, complete mitigation of these traits is implausible. Hence it is critical to investigate and minimize their effect on the WAAM fabricated products.

Figure 1.2: Distortion in component fabricated using WAAM [15]

Conventional strategies for mitigating distortion involve the development of tool paths with significant machining allowances to minimize dimensional deviations. Post-processing heat treatment is commonly utilized to address residual stresses. While these methods are somewhat effective, they detract from the efficiency and impede the utilization of Wire Arc Additive Manufacturing (WAAM) in metal additive manufacturing (AM) [16]. The recent developments in computational tools make them promising techniques for tackling the distortion problem in WAAM. For example, a sensor feedback-based tool path correction algorithm [17]. A part is fabricated using a tool path based on a CAD model. After deposition, the part is scanned and overlapped with CAD to calculate deviation. The correction algorithm reconstructs the tool path such that the new part upon deposition would distort to its intended shape as shown in Fig.1.3.
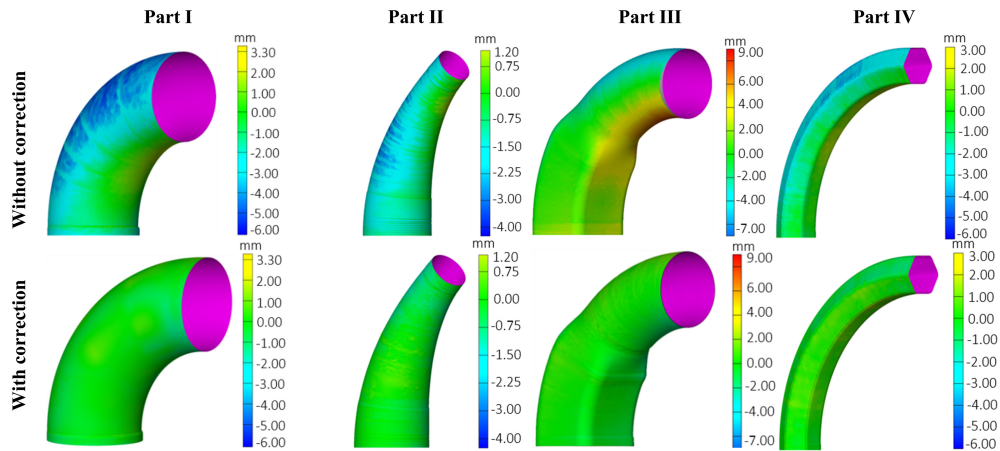
Figure 1.3: Scanned parts overlapped with CAD model: Top row parts fabricated using CAD based tool path (distortion resulted in deviation from intended shape), Bottom row parts fabricated with corrected tool path (distortion resulted in intended shape) [17]

In multi-axis WAAM, the use of practical methods like active cooling [18], continuous welding [19], symmetric material deposition [20], and modular tool path with variable process parameters [21] is highly depended on the geometrical shape and complexity of the deposited structure along with the external factors like welding source capabilities. The computational tools like tool path correction algorithm do not reduce the distortion rather, they change the course of distortion such that to nullify the negative effects of the distortion. Taking one step ahead, Wang et al.[22] developed a novel fabrication sequence optimization framework aiming to minimize the distortion in WAAM by altering the material deposition sequence. The fabrication sequence optimization generates an optimized pseudo-time field representing fabrication stages. The material deposition is decided based on corresponding pseudo-time values. The higher the time value, the later the material deposition as depicted in Fig.1.4
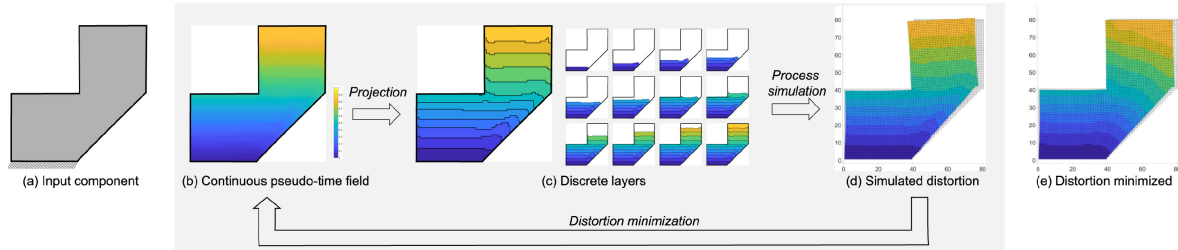
Figure 1.4: Fabrication sequence optimization Process. (a) The sequence for an input component, (b) Continuous pseudo-time field over the component, (c) Discrete layers generated by projection operators, (d) The distortion simulation by updating the pseudo-time field in an iterative optimization process, (e) Fully fabricated component with minimized distortion [22]
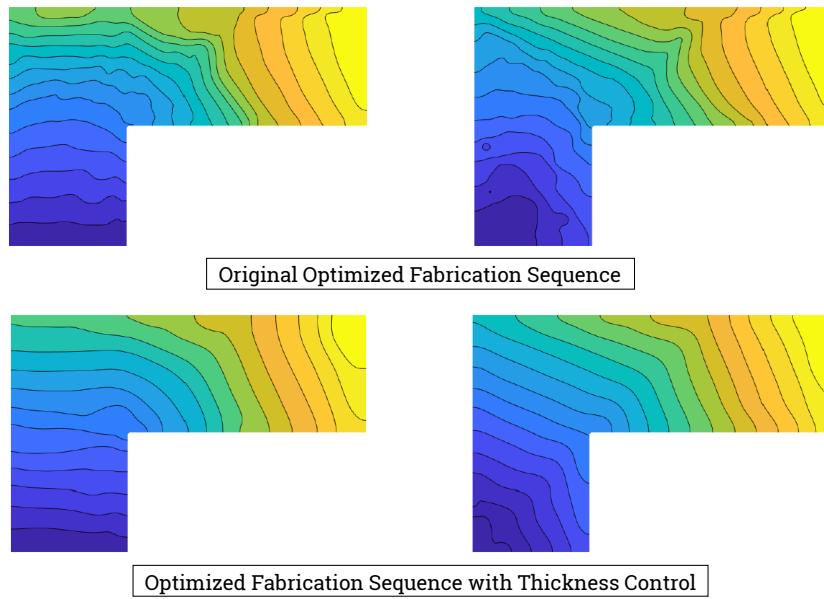
Figure 1.5: Optimized fabrication sequence with and without thickness control: Top row, different initial time fields, and no thickness control. Bottom row, same time fields as in top row with thickness control[23]

One of the major challenges with fabrication sequence optimization is the non-uniformity of thickness hence the material distribution, within a layer and in between layers. In the current stage, regardless of advanced kinematic setups, most of the WAAM setups demand uniform material distribution (indirectly constant process parameters) with little to no flexibility of varying process parameters in situ. To tackle this challenge, the objective function is modified to minimize the distortion at the same time minimize the variation in the layer thickness [23]. This is illustrated in Fig.1.4. The optimized fabrication sequence results in non-planar material deposition that can be realized by fabricating a given component using a multi-axis WAAM, thus the fabrication sequence optimization shows promising potential as a tool for generating optimized material deposition leading to a minimum distortion in the fully fabricated component.

1

Transformation of this simulation rationale into a cutting-edge engineering solution necessitates sound experimental validation. However, the pathway from simulation to experimentation is full of challenges bringing a back-and-forth joy ride between the design of experiments and simulation calibration. Henceforth, this thesis is focused on conducting a series of fabrication experiments on a multi-axis WAAM setup. This research aims to identify the challenges in fabricating a given structure with a planar and optimized fabrication sequence and to provide experimental validation.

1.3. RESEARCH OBJECTIVE

The simulation results from fabrication sequence optimization show a two-order magnitude reduction in distortion of the final deposited structure [22]. However, even with layer thickness control, the optimized sequence could generate an infeasible material deposition strategy that could not be possibly achieved in actual fabrication using multi-axis WAAM. The manufacturing feasibility of the optimized fabrication sequence is geometry-specific, material, and process-dependent. It is essential to grasp the challenges inherent in fabricating the part with an optimized sequence before embarking on the validation study. Addressing these challenges will facilitate progress towards future experimental validation studies. The research gap in fabrication with non-planar material deposition embodying the layer structure dictated by computationally determined optimized fabrication sequence forms the foundation of the scientific contribution made in this thesis. Therefore, the general research question is formulated as follows:

How can multi-axis wire arc additive manufacturing be utilized to construct structures with an optimized fabrication sequence involving non-planar material deposition, while also addressing methodologies for measuring distortion and global geometric formation to validate the optimization aimed at minimizing distortion?

To answer this research question, this thesis presents a series of fabrication experiments with the WAAM setup, with the main goal of realizing fabrication using non-planar material deposition.

To demonstrate the contributions of this work, the following objectives are formulated as follows:

1. Develop a material selection process to identify material/s,

   - When processed in WAAM, the welding characteristics make the fabricated components considerably prone to distortion.

2. Identify the optimal welding process parameters for the chosen material.

   - Investigation of the effect of process parameters on the geometric formation of the weld beads.

3. Perform in situ and ex situ strain/distortion measurement

   - To evaluate and compare strain development during fabrication on both planar and optimized deposition.

1.4. THESIS OUTLINE

This chapter presents a brief introduction to mitigation of fabrication challenges in AM using computational design tools, while also highlighting an area of research that needs further exploration. In addition, the chapter distinctly sets out the research goals for this thesis. The structure of the following thesis report is as follows:

- Chapter 2 offers an extensive literature review on the topic of tool path planning, materials used, and overall manufacturing challenges with WAAM along with situ/ex situ measurement during WAAM.

- Chapter 3 presents a detailed methodology and primary findings of this study, effectively addressing the research gap. This chapter is structured in scientific journal format to be self-contained.

- Chapter 4 delivers an in-depth discussion about fabrication experiments and various measurements.

- Chapter 5 concisely summarizes the conclusions and presents recommendations for future work.

- In the end, a series of extensive appendices A,B, and C provide detailed experimental procedures along with all the practical work undertaken. Furthermore, these appendices offer an opportunity to replicate, extend, and build upon this research.

2

LITERATURE PRELIMINARIES

2.1. MULTI-AXIS ADDITIVE MANUFACTURING

While the AM plays a significant role in realizing the complex design solutions, achieving the exact design could be limited due to the "planar layer-by-layer material addition" methodology. Depositing material in "non-planar layers" is, therefore, the next step towards reaching the intended design. To systematically describe the advantages of multi-axis AM, several design and manufacturing aspects are compared for 3-axis and multi-axis (more than 3) in Table 2.1.

	Three-axis AM	Multi-axis AM
Geometry Slicing for layer extraction	Planar horizontal slicing of the geometry with constant thickness or variable thickness	Planar horizontal as well as angular slicing along with non-planar slicing. Both approaches with constant or variable layer thickness.
The Stair-step effect	Always present in curved or overhang features of the final part	Can be eliminated with the help of multi-directional material deposition
Support Structures	If overhang is present then support structures are always needed	No support structure is required, overhang parts can be produced by rotating the deposition head or base plate.
Volumetric error	Could be significant due to planar approximation of varying surface or volume	Less than three-axis AM

Table 2.1: Three-axis versus Multi-axis additive manufacturing [5]

2.2. WIRE ARC ADDITIVE MANUFACTURING

From the metal fabrication perspective, the use of multi-axis AM is currently limited to Directed Energy Deposition and Material Extrusion metal AM. The integration of multi-axial material deposition enables the use of AM to fabricate large metallic structures and components with high deposition rates. Wire Arc Additive Manufacturing (WAAM) is a metal additive manufacturing method based on the Directed Energy Deposition. It is distinctive from other DED methods in terms of the type of raw material form utilized during AM. As the name of the method specifies, the raw material is in the form of wire and the overall process is "arc welding" at its essence. At present, most of the WAAM setups used in academic research as well as in the industry consist of an assembly of several components specifically a welding source with a wire feeding mechanism, fixed or movable mounting table, shielding gas supply, and a kinematic setup with welding torch as end effector (3-axis gantry or 6-axis industrial robot). The schematic presentation of this general setup is depicted in Fig.2.1. The material deposition during AM takes place by melting the wire with the help of an electric arc. The welding torch follows the tool path depositing material in a layer-wise manner to fabricate the final structure as illustrated in Fig.2.2

2

Wire Arc Additive Manufacturing
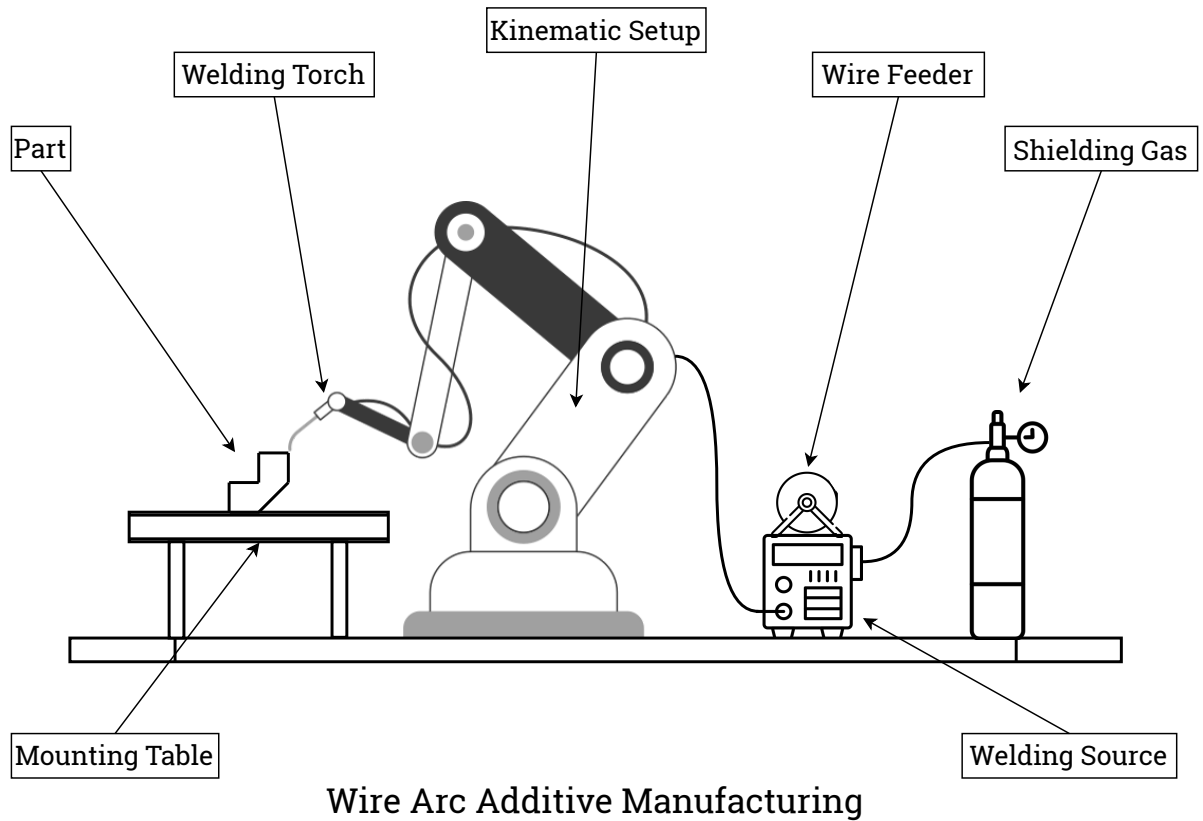
Figure 2.1: Schematic representation of multi-axis WAAM setup
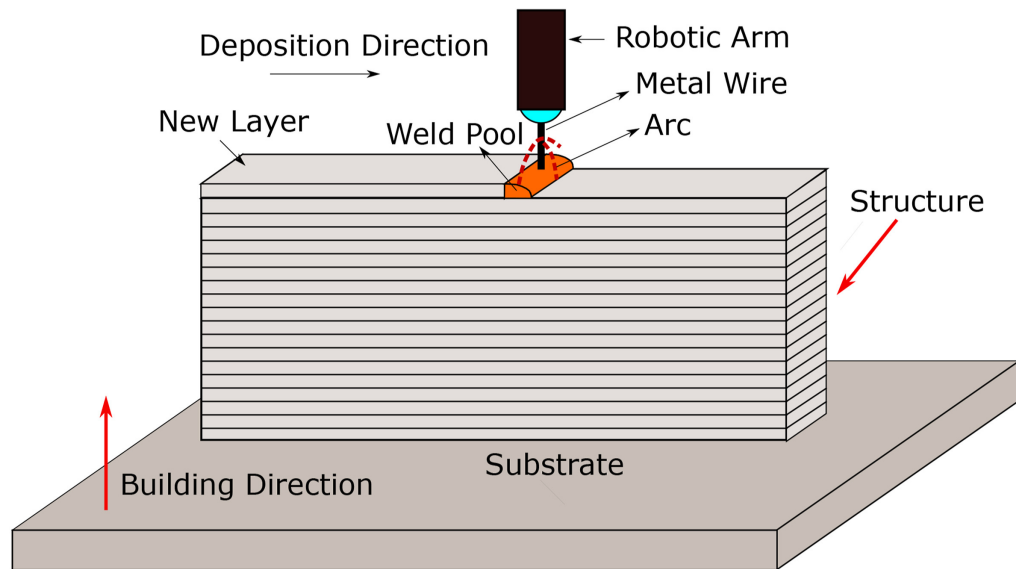
Figure 2.2: Fabrication using WAAM [24]

The welding process [25] for WAAM is further classified into

1. **Gas Metal Arc Welding** (GMAW), in which consumable electrode is used for arc generation, which is also the feed material with a higher deposition rate compared to GTAW and PAW.

2. **Gas Tungsten Arc Welding** (GTAW) with a non-consumable Tungsten electrode for arc generation and a separate material feed.

3. **Plasma Arc Welding** (PAW) with a non-consumable Tungsten electrode and water-cooled nozzle for

arc generation such that the arc ionizes the gas flowing through the nozzle creating plasma that acts as heat input to melt the separate material feed resulting in high weld quality compared to GMAW and GTAW.

Along with a welding source, a WAAM setup requires a kinematic setup to provide the necessary degrees of freedom to the welding torch. There are two types of kinematic systems,

1. **Gantry based systems**: X, Y, and Z motion of welding torch with optional rotational degrees of freedom to the baseplate [26].

2. **Robot-based systems**: Multi-axis (more than 3) robotic arm with optional rotational degrees of freedom to the baseplate [27].

WAAM is a near-net shape manufacturing process due to the melting and solidification of the wire during material deposition. Therefore, several design guidelines are suggested to efficiently use WAAM for metal fabrication. These guidelines are considered as *"Design for Wire Arc Additive Manufacturing"* (DfWAAM) and are briefly described in Table 2.2.

Design Guidelines	Notes
Component Dimensions	A minimum deposition thickness (2 mm in general) should be considered in the design phase. The minimum build volume dimension is 20mm
Symmetry of material deposition	Distortion is a prominent feature of WAAM hence the design should have some symmetry that can be utilized for symmetric material deposition.
Enclosed features	Design should consider the difficulties in post-processing and inspection of such features.
Limited post-machining	For unfunctional features/faces of a component avoid post-machining by performing stress peening-like processes.
Machining considerations	1 mm machining allowance is a standard practice in WAAM.
Infeasible features	WAAM in general are not suitable for complex components. Parts with long thin features are not suitable for WAAM e.g., lattice structures.
Sharp corners	Internal as well as external fillets are preferred for continuous deposition. Sharp corners and chamfers are undesirable.

Table 2.2: Design for wire arc additive manufacturing (DfWAAM) [28]

2.2.1. MATERIALS FOR WAAM

Technological advancement of WAAM in the last two decades has mainly revolved around high-strength steel, Titanium, Inconel, and other exotic alloys due to the high deposition rate and short lead times of WAAM, resulting in considerable savings in production time and material cost that justify the use of WAAM. However, in principle, all the filler materials utilized in arc welding can be used in WAAM. Due to the layer-by-layer deposition characteristics of AM, the material selection process and a comprehensive study of the inter-layer bonding, microstructure, porosity, mechanical, and physical properties are essential for WAAM. To select the material for WAAM, a closer look into that material's welding characteristics is necessary. In one of the earliest research of WAAM, a copper-coated mild steel wire is used to fabricate test structures like hollow cubes, and straight walls to study the effect of horizontal and vertical weld bead overlap on fabrication [29]. The same material when processed with different weld parameters or welding techniques in WAAM, can exhibit different mechanical and microstructural properties [30]. Improved tensile properties and toughness are observed for high nitrogen stainless steel using modified short-circuiting metal transfer in WAAM [31]. ER70S-6 low-carbon steel is a popular filler material in welding and it is widely studied for WAAM [32]–[35].
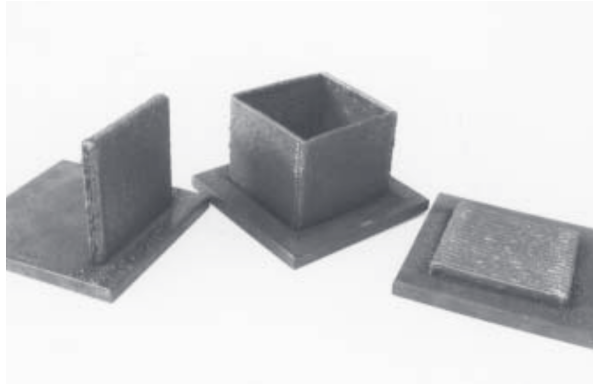
(a) Rapid prototyping of sample geometries using mild steel [29]   (b) Aerospace component using titanium [36]

Figure 2.3: WAAM using different materials

Titanium and titanium alloys [37], including Ti-6Al-4V [27], [38] and pure titanium [39], have been subjects of interest for WAAM due to their potential in achieving fully dense metal parts and for comparative studies with other additive manufacturing techniques like powder bed fusion. Similarly, nickel alloys like INCONEL 625 [40] and NiTi [41] shape memory alloys have been investigated for suitability in WAAM applications.

The processing of steel and expensive materials like titanium justify the use of WAAM for large-scale manufacturing. However, recently aluminum alloys have also been incorporated into WAAM. From a welding perspective, Aluminum alloys are highly susceptible to solidification cracking due to high coefficient of thermal expansion (CTE), and their high thermal conductivity demands high heat input during welding [42]. As WAAM is based on principles of metal welding, challenges in welding can be directly translated to the fabrication of Aluminum alloy components using WAAM [43]. High thermal expansion and the need for highly concentrated heat input can induce significant distortion in fabricated components. The wrought Aluminum alloys are utilized as welding consumable materials and are available in the form of wire with diameters ranging from 0.5 to 2mm. For WAAM applications, 2xxx series (Aluminum Copper alloys) [44], 4XXX series (Aluminum Silicon alloys) [45], and 5xxx series (Aluminum Magnesium Alloys) [46] are utilized. The commercial availability of the wire spools of the mentioned Aluminum alloys is limited and currently, a few alloy compositions from each series are available.

2.2.2. INFLUENCE OF PROCESS PARAMETERS

Optimal process parameters are key to obtaining high-quality output from a process. The process parameters affect the weld quality, surface quality, mechanical, microstructural, and physical properties, therefore an appropriate combination is needed as the desired objective of the final part fabricated using WAAM. The critical process parameters are torch speed (Travel speed), wire feed rate, input welding current, voltage, dwell time between weld pass, inter-layer temperature, heat input, and distance between torch tip- substrate (Arc length).

1. Torch Travel Speed: Stainless steels, including Hastelloy X [47] and ER70S-6 [48], exhibit distinct responses to variations in travel speed in WAAM. Adjustments in travel speed influence bead morphology and heat input, with higher speeds often resulting in narrower beads. Similarly, aluminum alloys like ER5356 [49] and ER2319 [50] demonstrate varying behaviors with changes in travel speed, highlighting the importance of parameter optimization for achieving desired part quality across different materials.

2. Wire Feed Rate: Aluminum alloy ER4043, showcases unique responses to alterations in wire feed rate in WAAM. Higher feed rates are typically associated with increased bead height but decreased width [51]. Moreover, mild steels exhibit distinct phenomena like uncontrolled humping at low wire feed rates [52]. For 316LSi steel, low WFR resulted in a final printed part accuracy of 99.6% compared to CAD [53].

3. Welding Current: In the case of Titanium Alloy Ti-6Al-4V deposition rate increases with welding current [54] and for TC11 increase in current decrease corrosion resistance with a slight decrease in ultimate tensile strength [55].

4. Heat Input: Heat input is directly proportional to current and inversely proportional to TS. Increasing heat input increases the distortion in the final part. For Super Duplex Stainless Steel With increased heat input tensile strength, yield strength, and hardness decreased [56]. On the other hand high heat input resulted in good wettability and thus low surface waviness for High Strength Low Alloy Steel ER110S-G [30].

5. Inter-layer Temperature: Inter-layer temperature defines the thermal gradient after each pass hence ultimately controlling the shape of the final part. For Aluminum and Titanium alloys, reduction in macro cracks, compressive strength, and residual stresses are observed increasing inter-layer temperature [57], [58]. Increased porosity with reduced tensile strength and hardness with increased inter-layer temperature is observed for Nickel alloys [59].

2.3. PATH PLANNING AND MATERIAL DEPOSITION STRATEGIES FOR WAAM

Unlike the other AM processes, path planning and material deposition are quite challenging for WAAM owing to its associated welding physics. Two primary concerning issues with WAAM are,

1. Large thermal gradient in the beginning of the layer causing insufficient weld penetration.

2. Heat accumulation at the end of layer casing excessive material spread resulting bead height reduction.

In order to address these issues there are two effective strategies available in the literature. The first one is keeping the travel speed and welding current larger than desired process values with a gradual decrease at the end of the layer[60]. The second is flipping the direction of deposition after each layer [61].

Medial axis transformation [62] is used to define the skeleton within each sliced layer and the tool path is generated by offsetting the skeleton geometry resulting in a gap-free material deposition in the given volume. Stable arc results in stable material deposition, however, if there are any crossings in the tool path, the previously deposited material would affect the arc stability. For such crossing, a continuous non-intersecting tool path with sufficient overlap can result in smooth material deposition [63]. For complex parts, the strategy of keeping constant process parameters could result in deposition failures due to non-uniform material deposition, to avoid this a modular path planning [21] is developed to deposit material uniformly for complex geometries with multiple crossing by dynamically adapting process parameters as shown in Fig.2.4. However, implementing this strategy is subject to the capabilities of WAAM setup such as communication between welding and kinematic systems.
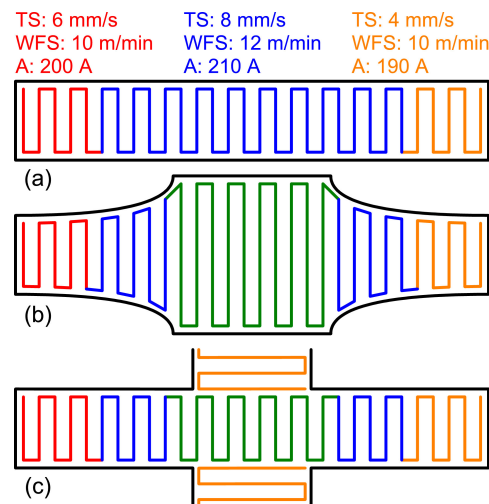
Figure 2.4: Modular tool paths for three different geometries (a), (b), and (c) [21]

Contrary to other metal AM processes, creating support structures for overhang features in WAAM is impractical as well as uneconomical. The fusion phenomenon in WAAM poses further challenges in fabricating geometries with overhangs. With multi-axial material deposition coupled with decomposition algorithm [64] that detects the overhangs and generates centroidal axes for each feature to create tool path based on multi-directional planar slicing along those axes. Embracing the multi-axial deposition with non-planar slicing is

achieved using Continuous Three-dimensional Path Planning (CTPP) [19]. In this strategy, the geometry is discretized to account for the variation in bead height in a nonplanar layer. Later the discretized parts are joined to form a continuous path for material deposition as shown in the top row of Fig.2.5. For structures with a high degree of curvature, gravity can significantly affect the bead formation when using non-planar material deposition with the help of optimized weaving patterns [20] the gravity effect can be compensated.
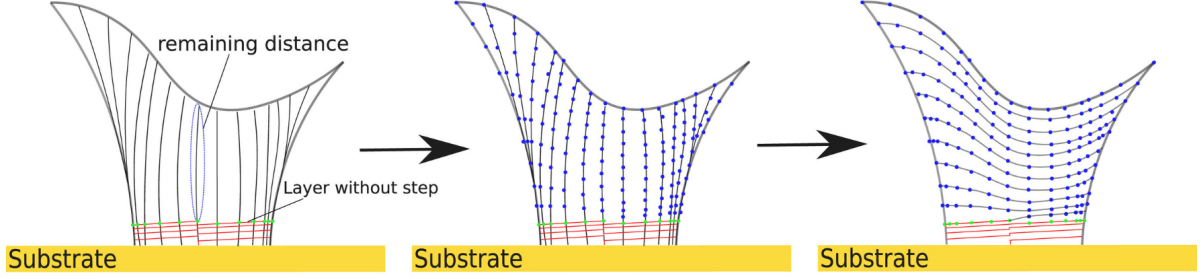
Figure 2.5: (a) Continuous tool path generated from discretization of skeletal lines [19]

2.4. Challenges in WAAM

With an extensive overview of Wire Arc Additive Manufacturing, it is understood that it is indeed a preferable metal AM process for medium to large-scale fabrication. Just like any other fabrication method, WAAM also has its limitations, nevertheless with the advent of state-of-the-art multi-axis kinematic setups, welding setups, control systems, and monitoring systems is it possible to overcome the various process-related challenges. On the other hand, parts fabricated using WAAM acquire special characteristics by the physics that governs the process. These characteristics include distortion/warpage, residual stresses (often manifesting in the form of distortion), and defects. These characteristics are unwanted and pose a major quality control issue, unfortunately, complete mitigation of these traits is implausible. Hence it is critical to investigate and minimize their effect on the WAAM fabricated products. For defects and post-processing challenges, readers are highly advised to refer to a comprehensive review of the WAAM process by Jafari et al.[16], and Bankong et al.[65].

2.4.1. Distortion

The foundation of distortion and stress analysis is the heat induced effects during the welding process in WAAM. Elastic or elastic-plastic stress fields, as well as associated local and global deformations, are produced by the time and position-dependent thermal strain ϵ_t (associated with temperature gradient) and transformation strain ϵ_{tr} (associated with phase change). The thermal strain affects the residual stress and distortion directly while transformation strain poses indirect effects [66]. Experimental investigation of all these parameters is a costly affair and oftentimes infeasible thus reliable numerical simulations (based on a few experimental calibrations) are proposed by researchers and industry experts. As the temperature field during welding in WAAM is the basis for simulation as well as experimental analysis of the process, temperature field evaluation is essential. For a simulation study, the temperature field is established by solving the 3D transient heat transfer equation,

$$\rho C_p \frac{\partial T}{\partial t} = -\nabla.\mathbf{q}(\mathbf{x}, t) + \dot{Q}(\mathbf{x}, t) - \dot{q}_{\text{Convection}}(\mathbf{x_s}, t) - \dot{q}_{\text{Radiation}}(\mathbf{x_s}, t) \tag{2.1}$$

Where $\dot{Q}(\mathbf{x}, t)$ is heat input from the arc, ρ is density of material, C_p is specific heat capacity, and T is temperature. Heat conducted, convected, and radiated is given by $\mathbf{q}(\mathbf{x}, t)$, $\dot{q}_{\text{Convection}}(\mathbf{x_s}, t)$, and $\dot{q}_{\text{Radiation}}(\mathbf{x_s}, t)$ respectively.

Thermal data is then incorporated into the mechanical analysis for the simulation of distortion and residual stresses. The temperature gradient and coefficient of thermal expansion (CTE) are used to evaluate thermal strains using,

$$\epsilon_{\text{Thermal}} = \text{CTE} \times \Delta T \tag{2.2}$$

In order to proceed with mechanical simulation linear momentum balance equation needs to be solved,

$$\nabla \cdot \boldsymbol{\sigma} + \mathbf{b} = \mathbf{0} \tag{2.3}$$

Where $\boldsymbol{\sigma}$ is the Cauchy stress tensor, $\mathbf{b}$ is the body force vector. During the welding process, total strain can be divided into elastic, plastic, thermal, and miscellaneous strains (including phase change, creep, etc.)

$$\epsilon_{\text{Total}} = \epsilon_{\text{Elastic}} + \epsilon_{\text{Plastic}} + \epsilon_{\text{Thermal}} + \epsilon_{\text{Misc}} \tag{2.4}$$

For the thermomechanical simulation of WAAM, a temperature-dependent elastic-plastic constitutive model is commonly utilized,

$$\epsilon_{\text{Elastic}} = \epsilon_{\text{Total}} - \epsilon_{\text{Plastic}} - \epsilon_{\text{Thermal}} - \epsilon_{\text{Misc}} \tag{2.5}$$

$$\boldsymbol{\sigma} = \mathbf{C} : \boldsymbol{\epsilon}_{\text{Elastic}} \tag{2.6}$$

$\mathbf{C}$ is the elastic constitutive tensor. Thermal strain is calculated using the coefficient of thermal expansion and temperature gradient. Plastic strains are estimated using an appropriate plasticity model with a suitable yield criterion (Von Mises yield criterion is quite popular in the literature) and misc. strain can be neglected as its effect is not significant. Thus solving equations 2.3, 2.5 and 2.6 with appropriate boundary conditions, the distortion and residual stresses can be estimated.

However, a fully coupled transient thermo-mechanical FE simulation could be computationally expensive as it involves non-linear and transient thermomechanics. There are a few strategies developed in the literature to tackle this problem, one popular method is the use of "Inherent Strain" concept [67].

$$\epsilon_{\text{Total}} = \epsilon_{\text{Elastic}} + \underbrace{\epsilon_{\text{Plastic}} + \epsilon_{\text{Thermal}}}_{\text{Inherent strain}} \tag{2.7}$$

To reduce the computational complexity, the following methodology is implemented in the FE simulations. As the weld bead cools down to the ambient temperature, thermal strain vanishes hence the inherent strain is defined as

$$\text{Inherent strain} = \epsilon_{\text{Plastic}} \tag{2.8}$$

These inherent strains are estimated using the maximum temperature in the welding process. The estimated value of inherent strains is used to estimate the nodal displacements and once the nodal displacements are known the total strains are estimated using the strain-displacement relation. As the total and inherent strains are estimated the elastic strains are calculated using equation 2.7 and the residual stresses are calculated using equation 2.6. Although the inherent strain method is effective for welding simulations, the assumption of neglecting other strains in the formulation of inherent strains and only using inherent strains for nodal displacement could result in erroneous estimates of residual stresses and distortion in WAAM.

2.4.2. DISTORTION MITIGATION STRATEGIES

Insightful literature is available on the prediction of the distortion on different scale models. As a complete mitigation of distortion is infeasible, it is essential to understand standard practices to minimize the distortion in WAAM. Distortion is primarily caused by thermal shrinkage that takes place due to the continuous melting of the feeding wire and rapid solidification of molten metal forming weld bead. Repetitive thermal cycles owing to layer-wise material addition in WAAM together with reduced cooling rate along build direction causing heat accumulation further augment the distortion. One of the straightforward practical approaches is to provide controlled external cooling either to the substrate or directly to the deposited structure. In WAAM of structures using Titanium alloys a compressed CO_2 based sequential cooling between layer deposition resulted in 81% and 69% reduction in longitudinal and transverse distortion [18]. Contrary to the cooling, uniform heating specifically pre-heating of the substrate could be beneficial for distortion minimization. Such pre-heating reduces the thermal gradient and thereby associated thermal strains. This technique is useful for aluminum alloys as they demand concentrated high heat input during welding. These distortion mitigation techniques are effective however, direct application is subjected to the complexity of the deposited structure, also implementing such strategies can substantially drive up the cost.

2
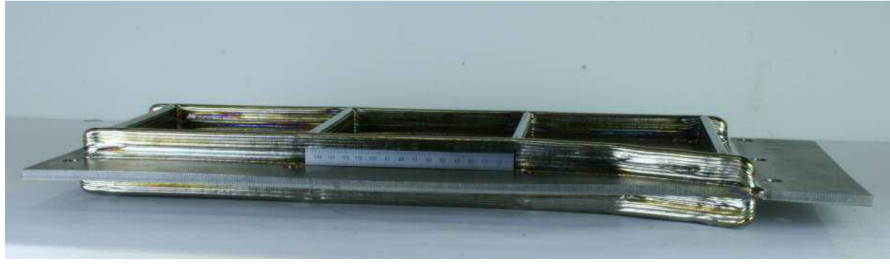
Figure 2.6: Balanced material deposition by printing on both sides of the substrate [68]
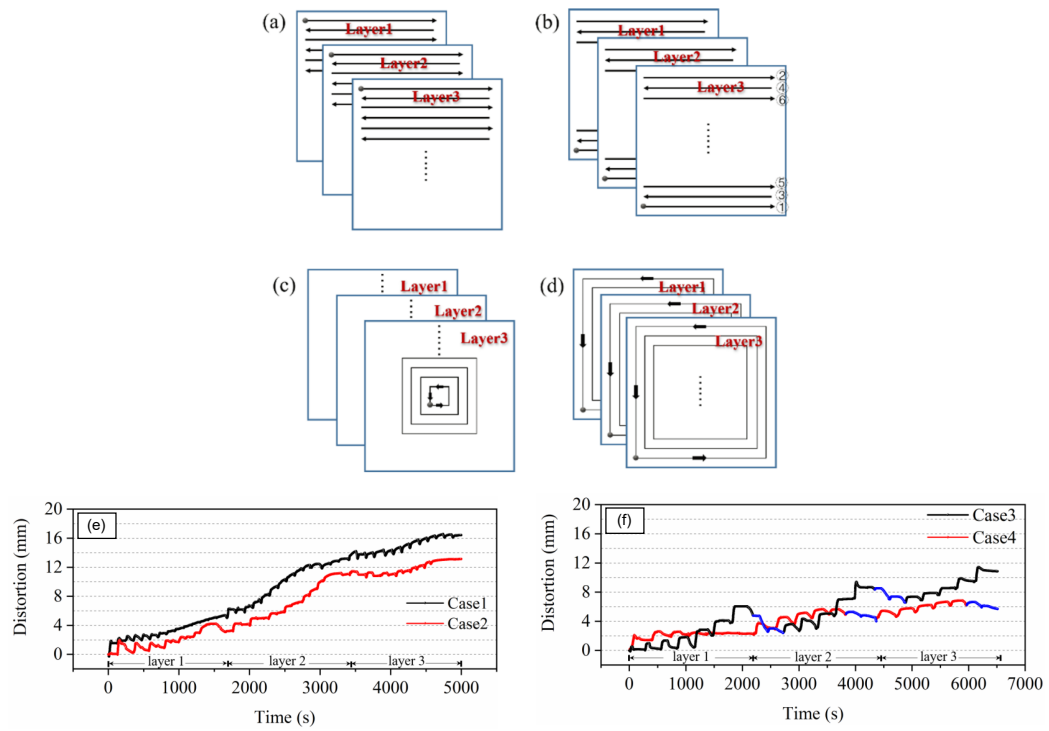
Figure 2.7: Effect of welding strategies on distortion: (a) Raster, (b) Symmetric Raster, (c) Contour-outward, (d) Contour-inward, (e) Distortion during fabrication for (a) and (b), and (f) Distortion for (c) and (d) [69]
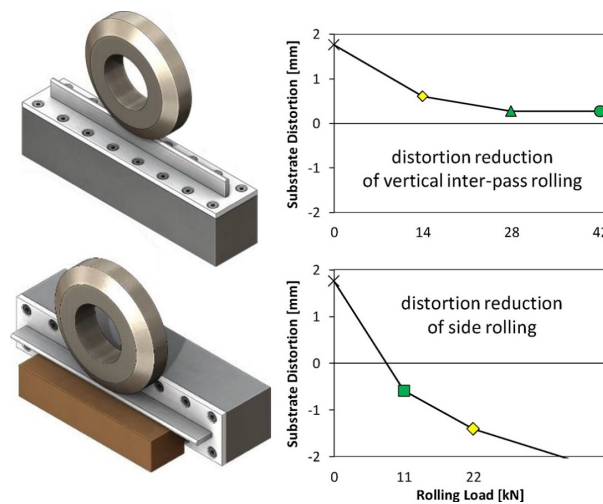
Figure 2.8: Effect of rolling on distortion[70]

2

Apart from actively or passively cooling or heating the substrate/deposited structure, heat input can be controlled using material deposition strategies. One technique is to deposit material on both sides of the substrate such that the plane passing through the center of the substrate is the plane of symmetry. This way the distortion in one direction is compensated by distortion in the opposite side as shown in Fig.2.6. The application of such a strategy is suitable only for structures with axis-symmetric features. When balanced deposition is not possible symmetric tool path-based material deposition can significantly reduce the distortion as depicted in Fig.2.7 where around 68 % out-of-plane distortion could be reduced. Application of external force is also an option for distortion reduction as shown in Fig.2.8, however, this method is not practical not complex shapes and sizes.

2.5. DISTORTION MEASUREMENTS

Measuring the distortion can range from being straightforward to exceedingly intricate, contingent upon various factors,

1. The quantification of distortion, i.e., the manner in which distortion is characterized.

   - Displacement of point or feature in the deposited part

   - Flatness of a feature

   - Geometrical relationship between features

   - Bending or torsion

2. Region of interest

   - Distortion of additively manufactured structure/part

   - Distortion of the substrate

Since the substrate is a fixed entity, unlike the deposited part which is constructed progressively, there are different innovative ways to measure distortion in the substrate. The simplest method is to attach a strain gauge (or series of strain gauges) either on the bottom or faces of the substrate before starting WAAM. Strain gauges give a localized measurement hence during the post-processing appropriate strain-displace relation is used to quantify the distortion. To measure deflection directly without the need for strain measurement, laser displacement sensors could be utilized as shown in Fig.2.9. The laser displacement sensor detects the reflected laser beam to calculate the distance between the sensor and the object within a specified range with high accuracy (typically 0.01 mm). With laser displacement, a change in focus of the laser during measurement can induce errors, so a physical contact sensor like a differential variable reluctance transducer (DVRT) has been utilized in the literature. The core of the DVRT is surrounded by a coil arranged in a Whetstone's bridge. Before printing the free end of the core is in contact with the substrate as shown in Fig.2.10 and since there is no motion the Whetstone's bridge is balanced. During printing the core is displaced as per the distortion resulting in an unbalanced Whetstone's bridge. Change in voltage is calibrated with core displacement, and distortion is measured accordingly.
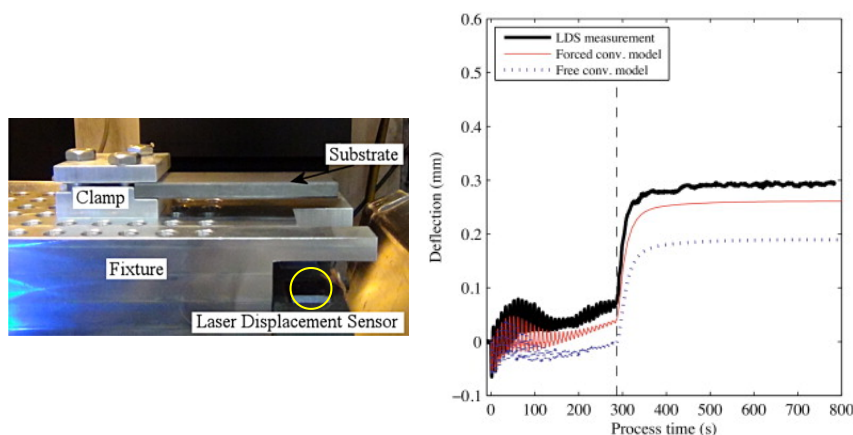
Figure 2.9: Laser displacement measuring deflection of the free end of the substrate [71]

2
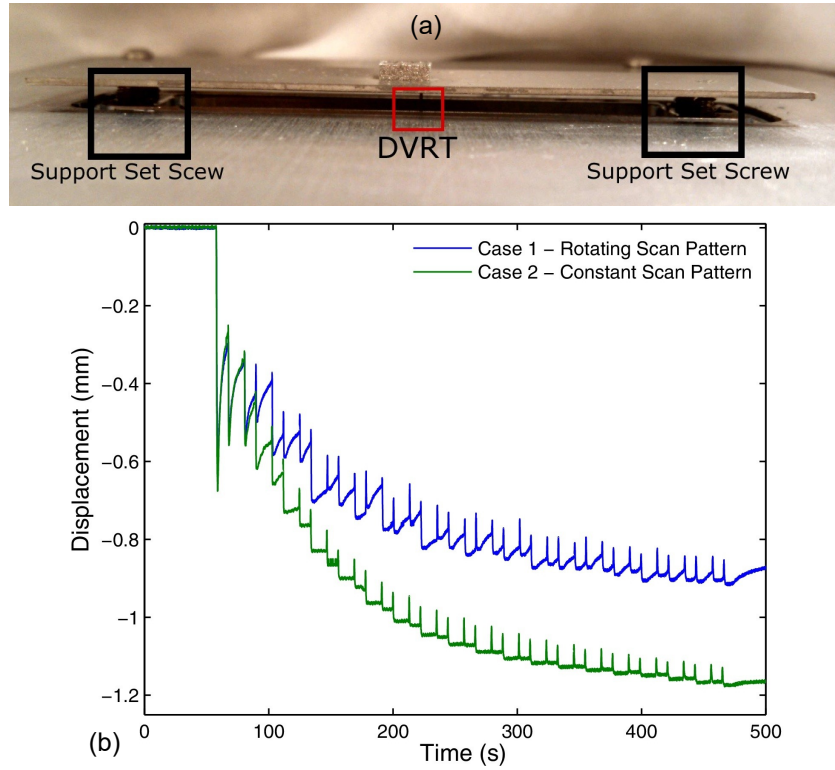
Figure 2.10: DVRT for distortion measurement of the substrate [72] : (A)Actual setup, (B) Schematic of distortion behavior, and (C) Distortion during printing
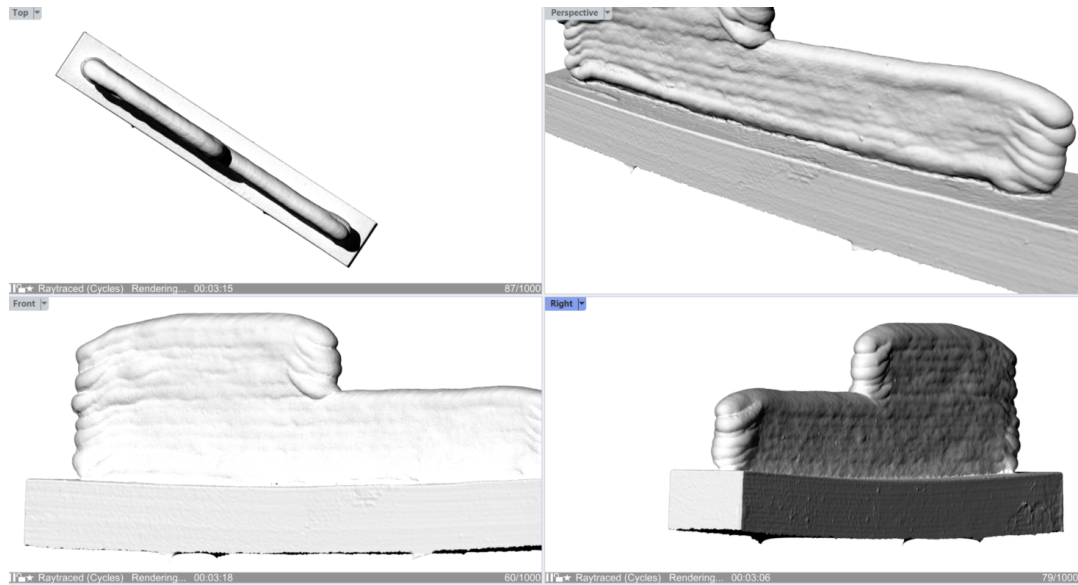
Figure 2.11: 3D Optical/ laser Scanning of the additively manufactured structure

A coordinate measurement machine (CMM) [73] can be employed to measure distortion on a local as well as global scale with very high accuracy (up to 0.001 mm). The above-mentioned techniques are appropriate for measuring the distortion of the substrate as all of these techniques compare geometrical data of the substrate with a reference state i.e., substrate before deposition material. To measure the distortion of the printed structure, the only reference is the CAD geometry, therefore, using strain gauges, and or displacement sensors might not be suitable in this case. Also, from a practical perspective mounting and calibrating such physical measurement devices during WAAM is not feasible. In such scenarios, non-contact type strain/distortion measurement techniques can be utilized. 3D scanning of the deposited structure using a laser/optical scan-

ner like Artec Space Spider [74]. 3D scanned models can be compared with original CAD models to calculate geometrical deviations indicating distortion.

3D scanning is an ex-situ measurement method, nevertheless, in AM it is also crucial to study the in situ distortions or strain development. In material characterization, a non-contact measurement technique called digital image correlation (DIC) is extensively used to measure strain evolution during different types of loading, and in recent years it has been integrated into metal AM [75]. In DIC, a random, isotropic, and high-contrast pattern is applied in situ on the partly fabricated structure, and then a camera captures a series of frames with a suitable frame rate as depicted in Fig.2.12 (a). These frames are further analyzed to track the speckle pattern to construct a displacement/strain field as shown in Fig.2.12 (b) and (c).
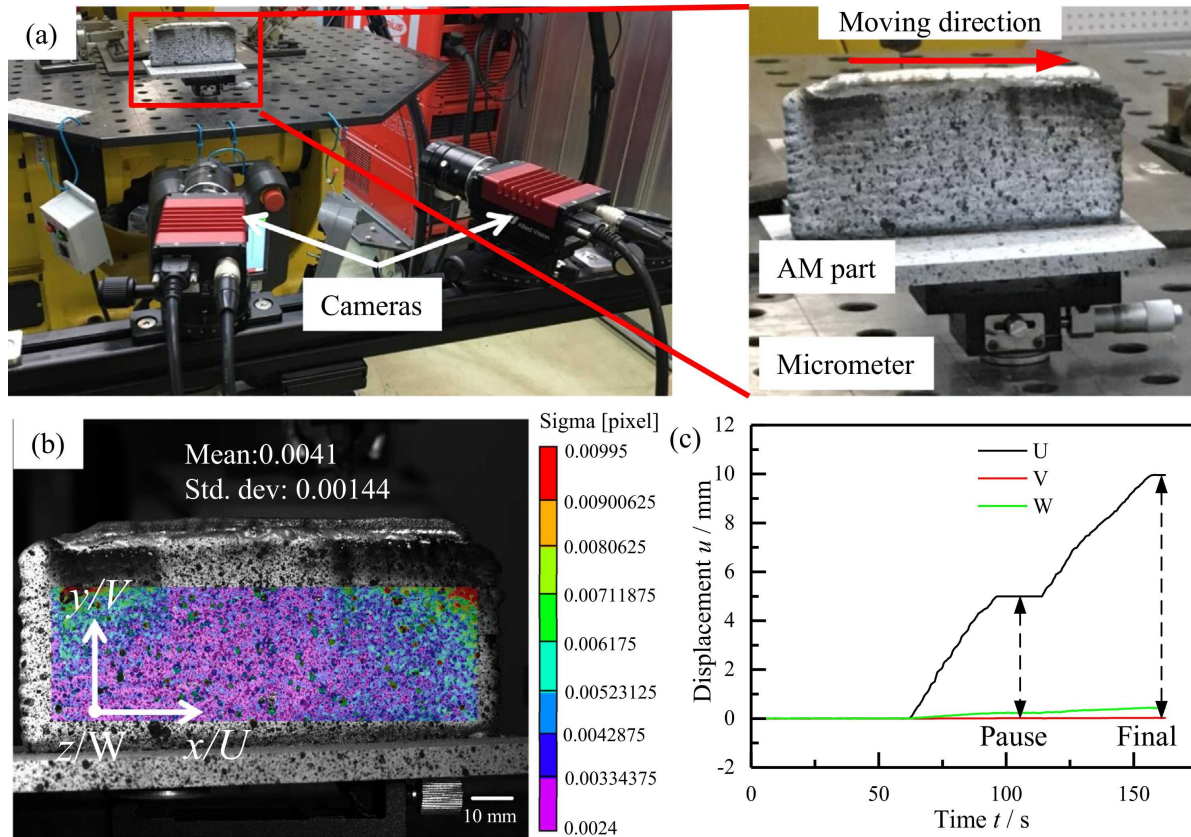
Figure 2.12: DIC measurements tracking speckle pattern on the fabricated wall to evaluate distortion [76]

3

Multi-axis Wire Arc Additive Manufacturing Using Optimized Fabrication Sequence

Abstract

Wire arc additive manufacturing (WAAM) enables higher material deposition rates and accommodates medium to large build volumes. Integrating multi-axis (more than three) kinematics into WAAM holds the potential to revolutionize the metal additive manufacturing industry. The material build-up with directed energy deposition results in localized melting and solidification of the feeding wire, rendering the fabricated structure prone to deposition defects such as distortion, residual stresses, solidification cracking, and porosity. Optimization of welding parameters can improve cracking and porosity behavior, but distortion remains inevitable. Current mitigation strategies rely on post-processing or symmetric material deposition; however, these approaches either reduce the effectiveness of WAAM with increased costs or can only be implemented for specific parts. Addressing distortion with computational design tools is a recent approach. Fabrication Sequence Optimization, dictating material deposition, is predicted numerically to limit distortion compared to conventional planar horizontal deposition; nevertheless, experimental validation is lacking. This research presents a series of fabrication experiments using Al 5356 aluminum-magnesium alloy wire in a 6-axis robotic WAAM setup in two parts: (1) Process parameter identification for optimal bead characteristics and (2) fabricating single-bead multi-layered thin-walled shell structures using both planar and optimized deposition. A digital image correlation-based non-contact distortion measurement setup is constructed to analyze strain development during fabrication, and 3D scanning of fabricated structures is performed to analyze dimensional deviation. Experimental findings reveal improved geometrical formation and a qualitative indication of distortion minimization in structures fabricated with optimized material deposition, laying the groundwork for experimental validation and calibration of fabrication sequence optimization.

Keywords: WAAM, Distortion, Aluminum, DIC, 3D scanning

3.1. INTRODUCTION

Multi-axis additive manufacturing (AM) holds substantial promise for catalyzing a paradigm shift within the manufacturing industry. Directed energy deposition-based wire arc additive manufacturing (WAAM) process offers high material deposition (up to 10 kg/hr [36]) and shorter lead times, furthermore, integration of multi-axis deposition using advanced robotic systems improves fabrication flexibility [8], [11]. In WAAM, a localized heat input in the form of an electric arc between an electrode and the substrate is used to melt the feedstock wire. It is then added to the molten metal pool and upon solidification at the melt pool boundary, the process is repeated to deposit the material in a layer-wise manner to construct the final part [6]. Uneven thermal expansion and solidification during the process acquire special characteristics of distortion/warpage, residual stresses (often manifesting in the form of distortion), and defects in structures fabricated using WAAM. These characteristics are unwanted and pose a major quality control issue, unfortunately, complete mitigation of these traits is implausible. Hence it is critical to investigate and minimize their effect on the WAAM fabricated products.

The conventional methods [16] of tackling distortion involve tool path development with high machining allowances to nullify dimensional deviations, and for residual stresses, the use of post-processing heat treatment is common. Such methods are effective up to an extent, however, they diminish the effectiveness and undermine the application of WAAM for metal AM. A new approach to address distortion is using computational tools during the design of the additive manufacturing (DfAM) process. However, this approach demands accurate measurement or prediction of strain development during the fabrication process and uses that in a feedback loop to modify the AM process. Thermo-mechanical simulations using finite element analysis have been used to predict the strain and in turn, distortion [77], [78]. In-situ/ex-situ distortion measurements using Laser Displacement Sensor [71], Digital Image Correlation system [75], [76], 3D scanning [79] are also carried out in the scientific literature. The computational techniques modify fabrication aspects like feature size, tool path, and layer sequence based on measured/predicted distortion data [17].

Fabrication sequence optimization [22] is an innovative approach of employing a novel computational framework to optimize the material deposition sequence of a given structure to minimize various distortion measures. In the optimization process, a pseudo-time field representing the fabrication sequence is optimized to determine the material deposition sequence for which a given distortion measure is minimum. Material deposition for a region based on its pseudo-time value. The higher the time value, the later the material deposition in the course of fabrication. Optimized fabrication sequence for distortion measures like absolute displacement, flatness, and perpendicularity of geometric features exhibited distortion minimization by two orders of magnitude compared to conventional planar fabrication sequence. However, this numerical study needs sound experimental validation to prove the effectiveness of the fabrication sequence optimization.

This paper presents a series of experiments on a multi-axis WAAM setup using Al 5356 Aluminum-Magnesium alloy wire as deposition material. The experiments are broadly classified into two categories;

1. Process parameter identification for optimal weld bead for Al 5356 wire

2. WAAM of 3D thin-walled single-bead multi-layer structures using both planar and optimized fabrication sequence followed by distortion measurements

The paper is structured as follows: Section 3.2 describes the WAAM setup, and material selection along with its welding characteristics for multi-axis WAAM with an optimized fabrication sequence. Section 3.3 presents the experiments performed to identify suitable welding process parameters for optimal bead quality. In section 3.4, the fabrication experiments for single-bead multi-layer walls and 3D thin-walled shell structures are explained in detail along with the strain measurements. The results of all experiments are discussed in section 3.5 and finally, section 3.6 summarizes the conclusions drawn from the study.

3.2. MATERIAL SELECTION AND MULTI-AXIS WAAM SETUP

The fabrication sequence optimization aims to reduce distortion and improve the overall quality of the components during and after fabrication, therefore, for the primary investigation the high coefficient of thermal expansion (CTE) along with the low cost (€/kg) are given priority during the material selection process. A comprehensive database by Ansys Granta EduPack [80] is utilized for the initial screening among the popular

material choices for WAAM. A penalty function is defined as

$$Z = \alpha_{CTE}\left(\frac{1}{CTE}\right) + \alpha_{Cost}(Cost) \tag{3.1}$$

Where α_{CTE} and α_{Cost} are weights assigned to each objective, equal weights are assigned during the screening. It is constructed such that part of objective $\frac{1}{CTE}$ upon minimization along with cost, rank the materials from the database with high CTE and low cost.
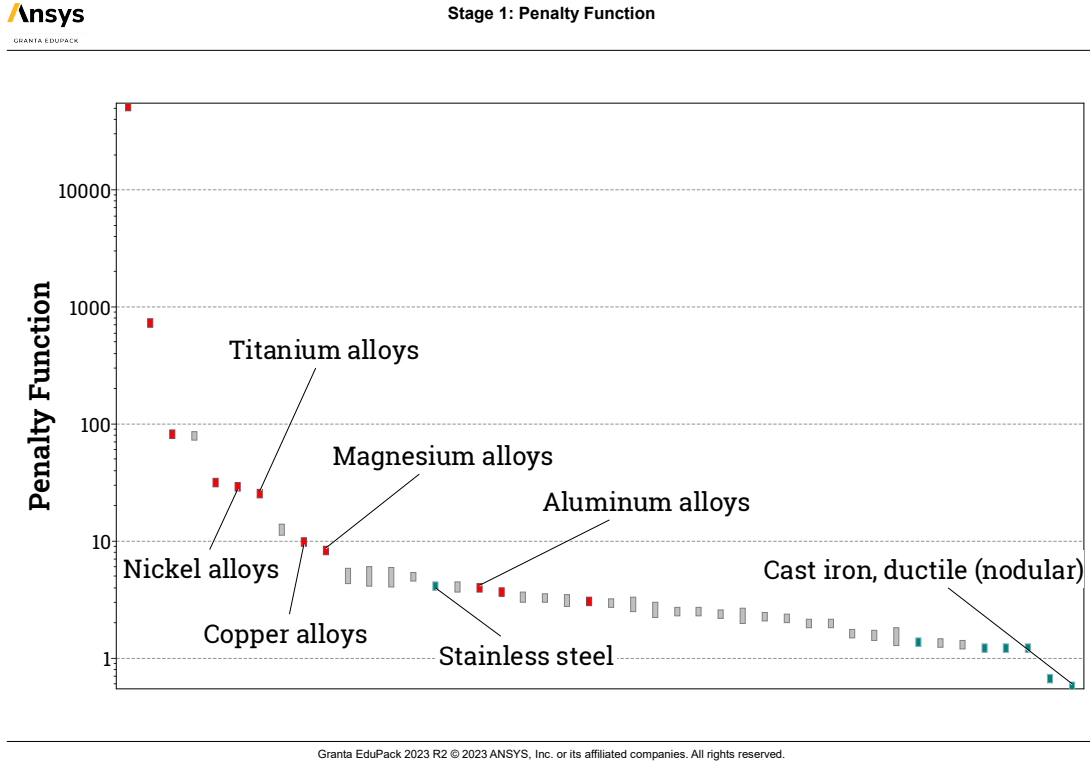
Figure 3.1: Penalty function value for all materials in the database: Low value indicates material with high CTE and low cost

The penalty function reached its minimum value for Cast Iron as shown in Fig.3.1 however, it is not used in WAAM because of its brittleness and inferior weldability. In between cast iron and aluminum alloys, there are several polymers as well as metals that exhibit a low value for the penalty function, however, they are either brittle or unsuitable for WAAM. Technological advancement of WAAM in the last two decades is mainly revolved around High Strength Steels [29], [56], Titanium [27], Inconel [40], and other exotic alloys due to high deposition rate and short lead times of WAAM, resulting in considerable saving in production time and material cost. On the other hand, Aluminum alloys are relatively inexpensive, readily available, and excellent engineering materials due to their high strength-to-weight ratio, high corrosion resistance, and formability. From a welding perspective, Aluminum alloys are highly susceptible to solidification cracking due to high CTE, and their high thermal conductivity demands high heat input during welding [42]. As WAAM is based on principles of metal welding, challenges in welding can be directly translated to the fabrication of Aluminum alloy components using WAAM [43]. High thermal expansion and the need for highly concentrated heat input can induce significant distortion in fabricated components. Therefore, fabrication sequence optimization can be a useful tool for WAAM using Aluminum alloys.

The wrought Aluminum alloys are utilized as welding consumable materials and are available in the form of wire with diameters ranging from 0.5 to 2mm. For WAAM applications, 2xxx series (Aluminum Copper alloys) [44], 4XXX series (Aluminum Silicon alloys) [45], and 5xxx series (Aluminum Magnesium Alloys) [46] are utilized. The commercial availability of the wire spools of the mentioned Aluminum alloys is limited and currently, a few alloy compositions from each series are available. Among the available choices, the

5xxx series shows a high average CTE for the temperature range of 20-300° C [81]. Solidification cracking associated with high CTE is also taken into consideration. In aluminum welding the base material chemistry affects the tendency of solidification cracking and the appropriate selection of filler material further reduces this tendency. For 5xxx and 6xxx series base material relative crack sensitivity decreases with increased Mg content as shown in Fig.3.2. However, in WAAM welding of filler material takes place in a layerwise manner, and using 5xxx series filler wire could minimize cracking tendency. Components fabricated using WAAM with 5xxx series wire exhibit a well-formed interlayer structure, improved surface finish, and uniform build-up compared to components fabricated using 4xxx series wire [82]. The popular 5xxx series filler wires and their chemical composition are mentioned in Table 3.1, and based on the commercial availability as well as cost a high Mg content Al 5356 wire of 1.2mm diameter is chosen for this research.
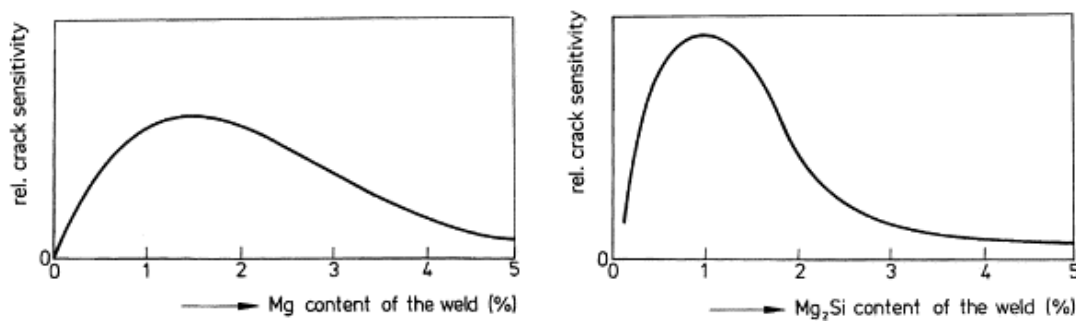
Figure 3.2: Effect of alloying elements crack sensitivity [83]

Wire type	Elements (% w/w)									
	Si	Fe	Cu	Mn	Mg	Cr	Zn	Ti	Be	Al
Al 5356	0.05	0.09	0.03	0.12	4.9	0.08	<0.01	0.15	0.0002	
Al 5183	0.03	0.13	0.001	0.65	4.99	0.1	0.02	0.07	0.0002	Remaining
Al 5554	0.06	0.13	0.01	0.7	2.6	0.08	-	0.09	0.0002	
Al 5754	0.07	0.13	0.01	0.29	3	0.06	-	0.05	0.0004	

Table 3.1: Chemical composition of the Al 5xxx alloy wires (% Weight)

(a) 3-axis Gantry Setup

(b) 6-axis Robotic setup
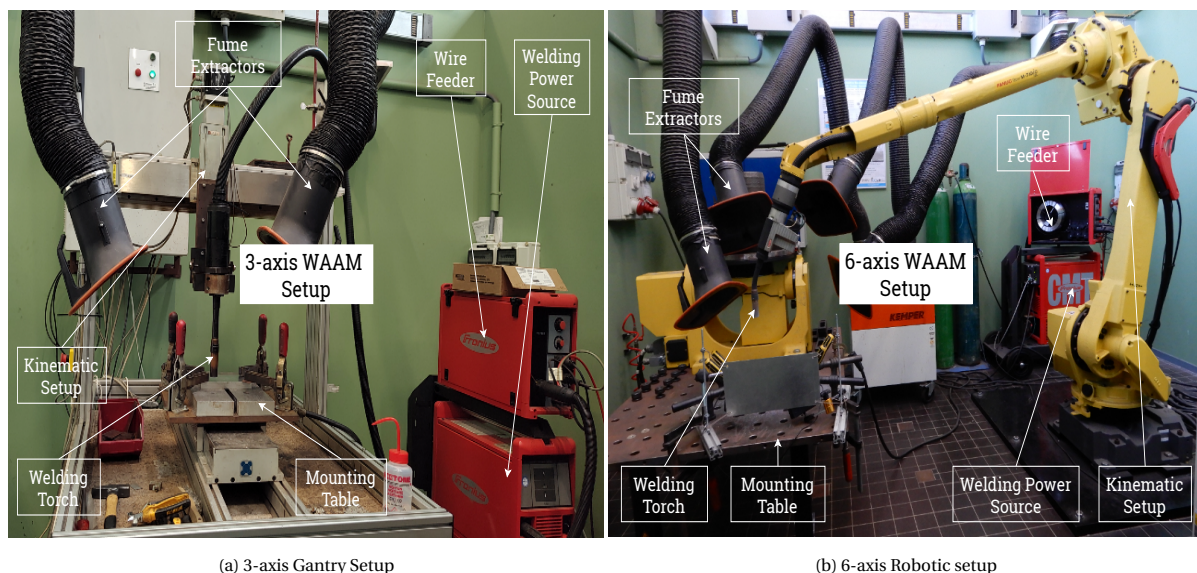
Figure 3.3: Multi-axis WAAM setup utilized in the fabrication of aluminum structures

Gas metal arc welding (GMAW) is most suitable for multi-axis WAAM setup and different metal transfer modes can be easily adopted. The 3-axis WAAM setup as shown in Fig.3.3a, consists of Fronius *"TransPuls*

Synergic 5000 Remote" GMAW welding power source with a water-cooled welding torch, VR 7000 wire-feeder with push mechanism, and a gantry-based kinematic setup with mounting table. The 3-axis motion is achieved by moving the table along the X-axis and the welding torch along the Y and Z-axis. The kinematic setup for multi-axis WAAM setup as shown in Fig.3.3b, comprises of 6-axis *"M-710iC/12L"* robot by FANUC with welding torch attached to the end effector. The robot provides 6-axis motion while the mounting table is fixed. The GMAW welding power source is *"TransPuls Synergic 3200 CMT R"* with a water-cooled welding torch, VR 7000 CMT wire feeder with push-pull mechanism. For both setups, 100 % Argon is used as shielding gas.

Processing Aluminum/Aluminum alloys in WAAM are subjected to employing low and controlled yet concentrated heat input to the weld bead. Spray metal transfer mode is preferred for welding Aluminum alloys, as other modes of metal transfer such as short-circuit, and globular can result in incomplete fusion, and premature solidification of molten metal droplets respectively. Although spray transfer is suitable for welding Aluminum, it can be problematic for Aluminum WAAM due to continuous arc with high current density and limited welding positional capabilities. The pulsed-spray and modified short-circuit metal transfer (e.g. Cold Metal Transfer (CMT) [84]) modes are, therefore, appropriate for WAAM using Aluminum alloys. Both metal transfer modes provide low and concentrated heat input, however, heat input in the pulsed-spray transfer is relatively higher than CMT, thus pulsed-spray metal transfer mode is considered for this experimental study.

A state-of-the-art Pulsed Synergic GMAW with a special 2-step current trigger is used in the fabrication. In the pulsed-spray transfer mode, the current pulses between a lower and an upper bound, the upper bound is known as the peak current which pinched the drop away from the wire tip, and the lower bound is the background current that keeps the arc on throughout the process. Continuously on arc with pulsating current maintains low heat yet concentrated heat input to overcome the high thermal conductivity of the Aluminum alloy. The pulsed mode characterizes local fluctuations in welding current as depicted in Fig.3.4a, whereas the special 2-step current trigger characterizes fluctuations in welding current at a global scale, during the beginning of the welding it overshoots the local average value of the welding current and then gradually brings it back to the set average current value during welding and undershoot it towards the end of the welding as shown in Fig.3.4b. This overcomes the high heat sink effect of Aluminum alloys due to their high thermal conductivity.

(a) Welding current variation in a complete single weld   (b) Current variation during metal transfer
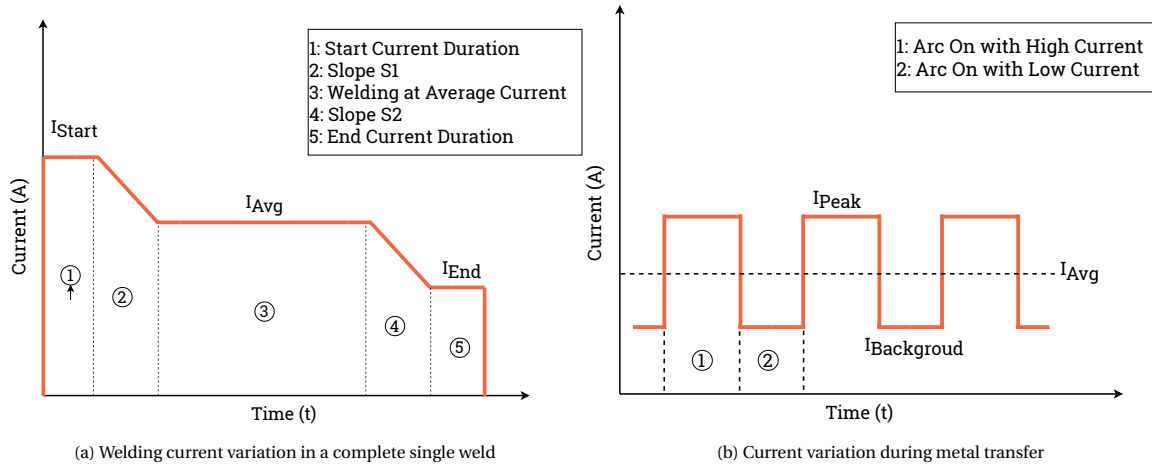
Figure 3.4: Welding current behavior at global scale (a) and at local scale (b)

3.3. Welding Parameter Study for Optimal Bead Quality

In the current stage, the development of a WAAM setup is not standardized and most of the setups are assembled from a variety of kinematic and welding sources, thus it is crucial to evaluate optimal process parameters for the specific welding and kinematic setup used in the study from the suitable range available in the literature. The average heat input Q_{avg} (J/mm) in GMAW is given by,

$$Q_{avg} = \eta \frac{V_{avg} I_{avg}}{v_{Torch}} \tag{3.2}$$

where, V_{avg}, I_{avg}, v_{Torch}, and η are average welding voltage (Volt), average welding current (Ampere), Torch speed (mm/s), and welding source efficiency respectively.
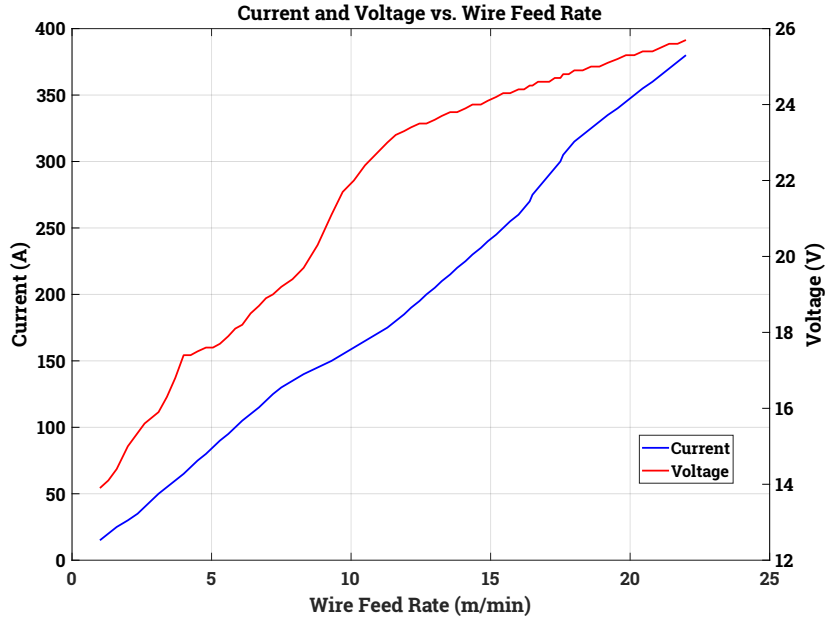
Figure 3.5: Relation between current-voltage and wire feed rate for pulsed Synergic GMAW of Al 5356 1.2mm diameter wire

In the Pulsed Synergic GMAW, the wire feed rate (WFR) is an independent variable, and V_{avg}, I_{avg} are set accordingly. For the Al 5356 1.2mm wire with pulsed-spray metal transfer mode, the current-voltage-wire feed rate characteristics are shown in Fig.3.5, and process optimization revolves around determining optimal combinations of wire feed rate and torch speed. A 2x2 factorial experiment is designed to obtain the primary response of the single bead 5xxx series Aluminum alloy WAAM on the extreme wire feed rates and torch speeds, as described in Table 3.2. The minimum and maximum values for v_{Torch} are based on realistic welding speeds and similarly, WFR correspond to 50 and 300 Ampere current. Welding current below 50 is possible however, it is impractical for Aluminum welding/WAAM.

		v_{Torch} (mm/s)	
		Low (2)	High (2)
WFR (m/min)	Low(1)	3.1, 1	3.1, 20
	High(1)	17.5, 1	17.5, 20

Table 3.2: 2x2 factorial experiment with wire feed rate and torch speed

The factorial experiment directed another investigation with gradually increasing wire feed rate (thus welding current and voltage) with different torch speeds between 2 and 20 mm/s. The WFR and v_{Torch} being independent parameters in the Pulsed synergic GMAW, a dimensionless parameter λ is defined as

$$\lambda = \frac{WFR}{v_{\text{Torch}}} \tag{3.3}$$

to give a qualitative estimation of the behavior of weld bead with given process parameters. The direct proportionality of WFR, I_{avg}, and V_{avg} as depicted in Fig.3.5 along with the equation 3.3, λ can be used to estimate the average heat input,

$$\lambda \propto Q_{avg} \tag{3.4}$$

λ is a dimensionless quantity, however, in welding/WAAM WFR and v_{Torch} are described in m/min and mm/s respectively. Therefore, another parameter λ' is defined such that to consider the dimensional conversion.

$$\lambda' = \frac{3}{50}\lambda \tag{3.5}$$

For the same value of λ', the average heat input can be different due to V_{avg}, I_{avg}, and WFR characteristics of the selected Pulsed synergic welding. For $\lambda' = 1$, a combination of $WFR = 20$ m/min with $v_{Torch} = 20$ mm/s results in 25.7 % more Q_{avg} than a combination of $WFR = 10$ m/min with $v_{Torch} = 10$ mm/s, provided unaltered welding efficiency. Therefore, the optimal range of λ' for different current ranges is investigated further. The process parameters corresponding to the suitable range of λ' would result in a weld bead with the following features.

- Complete and sufficient fusion

- Uniform surface finish without any humps or scallops

- Uniform and proportional geometrical dimensions

The Above experiments give a qualitative estimation of the geometric formation of the single bead deposition, to estimate the cross-sectional dimensions, area, and shape of the bead another set of experiments is carried out in which a total of 9 single beads are printed using the process parameters given in Table 3.3. The cross-section of a bead is illustrated in Fig.3.6, a local coordinate system is placed at the bead and substrate interface such that the origin is at the center of the interface. With total bead height h measured from the origin along the y-axis and the total width w is measured across the origin along the x-axis, spanning from $\frac{-w}{2}$ to $\frac{w}{2}$. Different shapes can be used to describe the bead cross-section. In this study parabolic, cosine, and arc shapes are considered. For a given bead height and width, all three shapes are fitted on the local coordinate system shown in Fig.3.6. Table 3.4 describes the equations for parabolic, cosine, and arc shapes along with their area for bead cross-section shown in Fig.3.6.

Bead number	Current (A)	WFR (m/min)	v_{Torch} (mm/s)	λ'
1			5	1.18
2	100	5.9	4	1.48
3			3	1.97
4			7	1.07
5	130	7.5	6	1.25
6			5	1.5
7			7	1.33
8	150	9.3	6	1.55
9			5	1.86

Table 3.3: Welding process parameters for 9 single bead printing
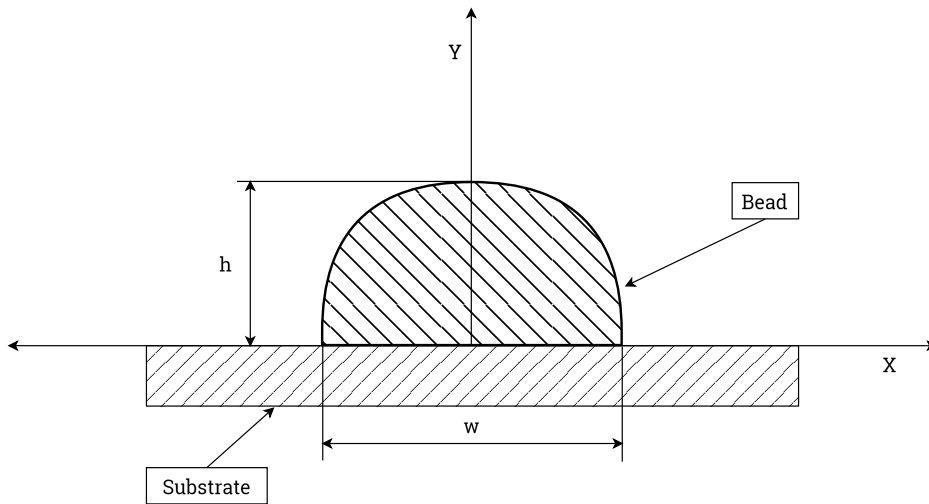
Figure 3.6: Bead cross-section profile with origin at bead center and substrate interface

Shape	Equation	Area	Constants	
			a	b
Parabola	$y = ax^2 + b$	$\frac{2hw}{3}$	$\frac{-4h}{w^2}$	h
Cosine	$y = a\cos(bx)$	$\frac{2hw}{\pi}$	h	$\frac{\pi}{w}$
Arc	$\sqrt{a^2 - x^2} + b$	$\arccos\left(\frac{-b}{a}\right)a^2 + \frac{wb}{2}$	$\frac{4h^2 + w^2}{8h}$	$\frac{4h^2 - w^2}{8h}$

Table 3.4: Geometrical shapes with their areas in terms of bead width and height

(a) Welding current variation in a complete single weld   (b) Current variation during metal transfer
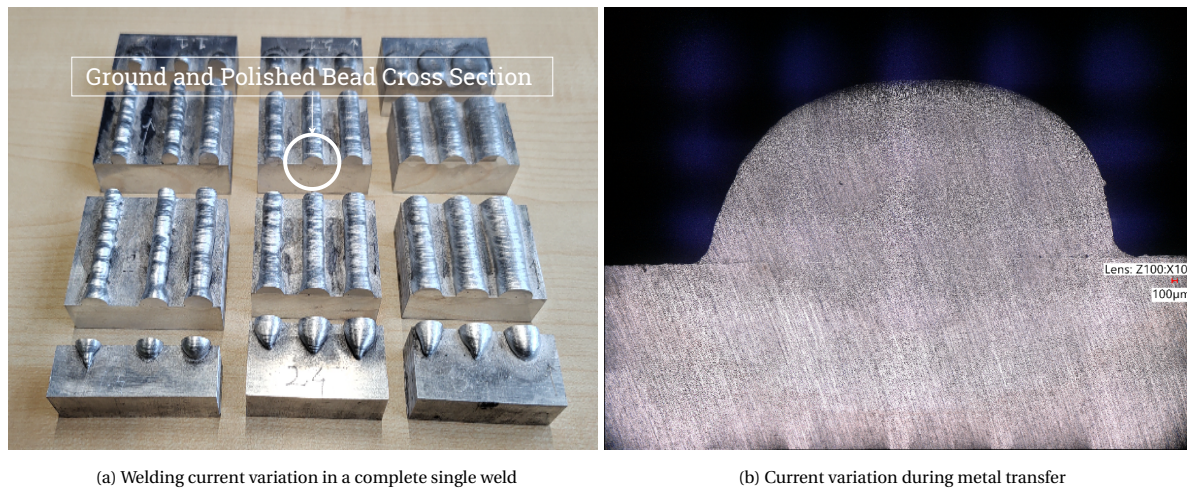
Figure 3.7: 9 beads printed, cut, grind, and polished to analyze cross-sectional shape

To analyze the shape of beads, all beads are cut at three locations with a cutting plane perpendicular to the length of the bead as depicted in Fig.3.7a. After cutting each sample is grind and polished to view under a microscope for generating high-resolution images of the bead cross-section as shown in Fig.3.7b. Bead width, height, and area are measured using image processing software *Fiji-Image J* [85]. The measured height and width are used to calculate the area using equations given in Table 3.4 as if the bead shape is perfectly a parabola, cosine, and arc then compared with the measured area to evaluate the closeness of shape among three shapes.

3.4. Fabrication of Aluminum Structures using Multi-axis WAAM

3.4.1. Single-Bead Multi-layer Walls

To fabricate components using WAAM, a multi-layered material deposition is necessary. Thus, in accordance with the geometric complexity and type of part (thin-walled or fully dense solid), each layer may contain one or more overlapping beads. In the case of WAAM using 5xxx series Aluminum alloys, general bead dimensions are in the order of 10mm, hence the number of overlapping beads along with the total number of layers is significantly less than other types of metal AM. The effect of the welding process parameter is local to the bead, affecting its dimensions and geometric formation. However, when realizing a structure or component consists of multiple beads regardless of how many beads are in one layer it is crucial to understand the effect of following parameters on the overall buildup of the component,

1. Vertical distance between the torch and deposited bead in single-bead multi-layer deposition.

2. Horizontal distance between the torch and deposited bead in multi-bead multi-layer deposition.

3. Inter-layer temperature between each deposition.

4. Dwell Time between each deposition.

In component fabrication using WAAM, either a constant inter-layer temperature (increasing dwell) or a constant dwell time (increasing inter-layer temperature) approach is employed. The choice of approach is greatly dependent on the material used in the fabrication process. Aluminum alloy is highly sensitive to heat input owing to its high heat conductivity, the constant dwell time strategy with increasing inter-layer temperature would result in unstable buildup with increasing bead width as the number of layers increases during the deposition. For welding of aluminum alloys, the upper limit of inter-layer temperature is defined as 120° C [86].

Set No.	Wall no.	Length (mm)	Current (A)	WFR (m/min)	v_{Torch} (mm/s)	Interlayer Temperature (°C)	Z-axis motion after each layer (mm)
	1	160	100	5.9	5	90	2
1	2	160	100	5.9	5	70	2
	3	160	100	5.9	5	50	2
	4	160	130	7.5	7	90	2.5
2	5	160	130	7.5	7	70	2.5
	6	160	130	7.5	7	50	2.5
	7	160	150	9.3	7	90	3.5
3	8	160	150	9.3	7	70	3.5
	9	160	150	9.3	7	50	3.5

Table 3.5: Prcoess parameters, inter-layer temperatures, and torch z-axis inter-pass motion for 9 walls fabricated using WAAM

Therefore, in this study, constant inter-layer temperature with increasing dwell time is used to fabricate all components. This study is focused on the fabrication of thin-walled components, thus each layer consists of a single continuous weld bead. Three sets of process parameters are used to fabricate 9 single-bead multi-layer wall structures. In each set, 3 wall structures are fabricated with 90°, 70°, and 50° C inter-layer temperatures. Table 3.5 shows the process parameters for printed single-bead multi-layer wall structures. The temperatures are measured using a FLIR ER6000 digital infrared thermal camera. The effect of inter-layer temperature along with the distance between the welding torch and previously deposited weld bead are analyzed and the results are used to fabricate single-bead multi-layer thin-walled structures.

Figure 3.8: Inter-layer temperature measurements using thermal camera

3.4.2. 3D THIN-WALLED STRUCTURES

In a single-bead multi-layer wall (2D), fabrication of the overhanging feature is impossible due to the absence of material that either interrupts the welding process or results in poor material buildup. Therefore, to study the fabrication process using an optimized fabrication sequence, 3D thin-walled shell structures consist of a single bead per layer and are fabricated with two strategies, (1) material deposition with planar layers and (2) material deposition optimized layers.

Tool Path for Planar Fabrication Sequence

Dimensions are in mm

Figure 3.9: Tool path for planar fabrication. Left: Structure comprising of planar horizontal layers. Right: Tool path for depositing planar horizontal layers with overhang region (1) and top region (2)

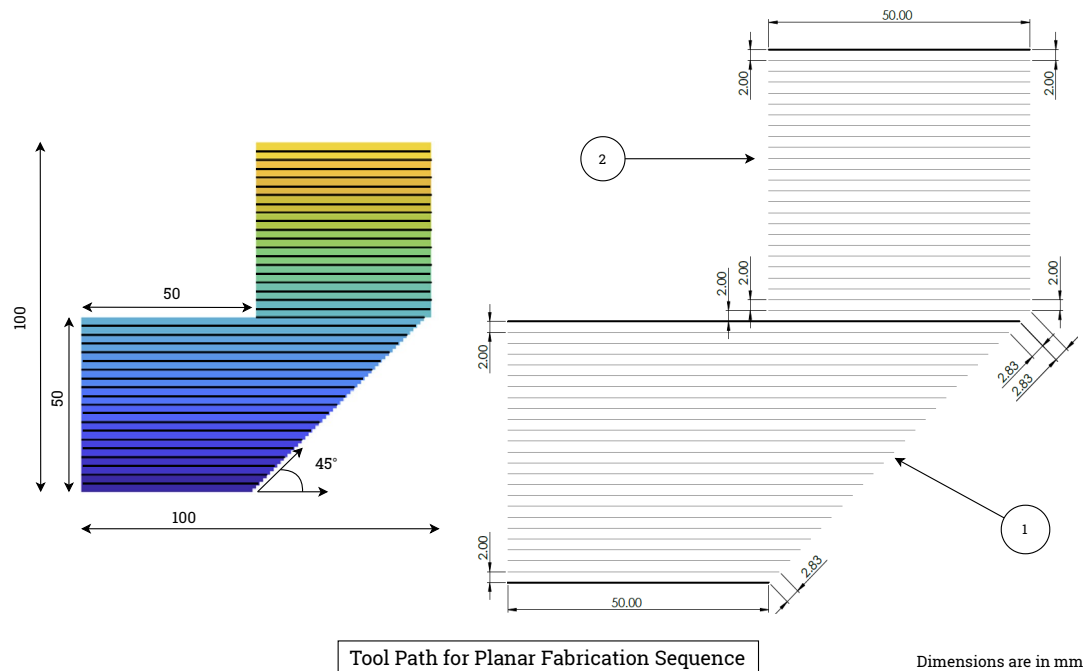Tool Path for Optimized Fabrication Sequence

Dimensions are in mm
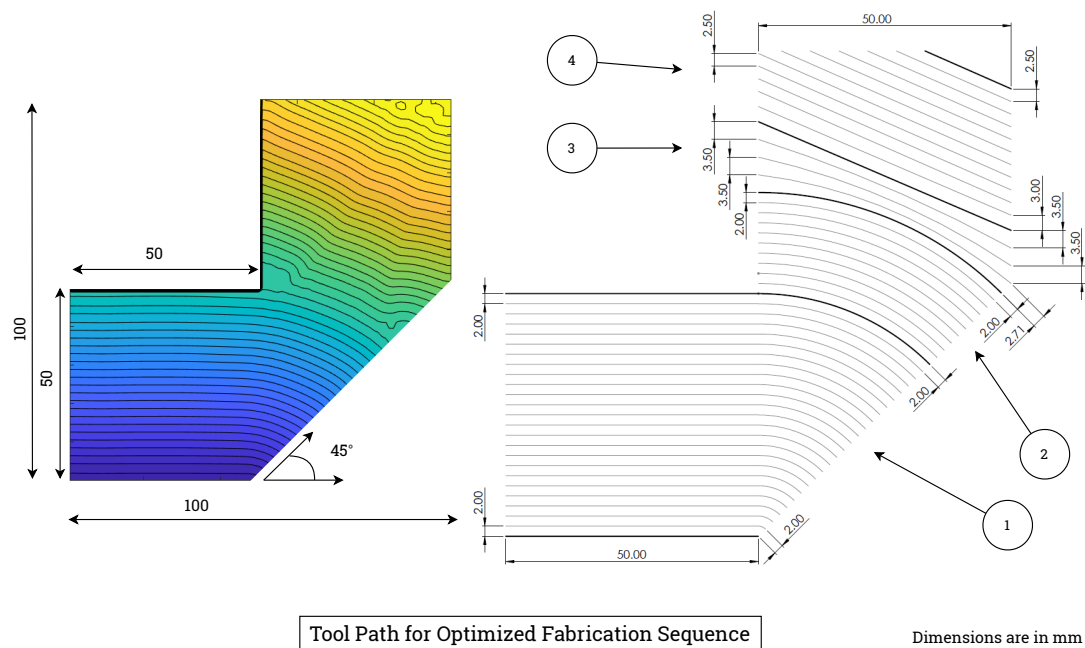
Figure 3.10: Tool path for optimized fabrication. Left: Structure comprising of non-planar layers. Right: Tool path for depositing non-planar layers with overhang regions (1) and (2), transition region (3), and top region (4)

In the case of planar fabrication, the layers are planar and horizontal. In Fig.3.9, the left figure depicts the layer orientation with conventional AM bottom-to-up build direction, and the right figure illustrates the tool path required to achieve this deposition. However, for the optimized fabrication, the layers can be non-planar or a combination of planar and non-planar as shown in the left figure in Fig.3.10, to achieve this material deposition using multi-axis WAAM, the proposed tool path is illustrated in right of Fig.3.10. These tool paths are used to fabricate the side walls of 3D thin-walled structures. The complete tool path for planar material deposition is made of straight lines parallel to the X-Y plane as depicted in Fig.3.11. For optimized material deposition, it consists of curved paths for side walls and straight lines for the region connecting two walls as described in Fig.3.12. The tool paths are created in WeldPRO software by FANUC. These components are fabricated on 200 x 100 x 15 mm Al 6061 substrates. The same welding parameters are given in Table 3.6. The minimum and maximum Z-axis motion of the welding torch after each pass for the good geometric formation of the bead is studied in the previous experiments. It is set to 2 mm for planar fabrication and for non-planar deposition, it is varied between 2mm to 3.5mm in different regions of the components based on the transition of the curved path. In the case of planar depositions, after each layer, tool path points are offset by the same distance also the tool path consists of straight lines, therefore, tool path development is relatively straightforward. However, for the non-planar deposition, the location of points defining the tool path depends on the degree of curvature desired. In the fabrication sequence optimization, the optimized time field governs the shape and size of each layer. Hence, the tool path is constructed geometrically such that the shape and size of the deposited layer will closely match the output of the fabrication sequence optimization algorithm.
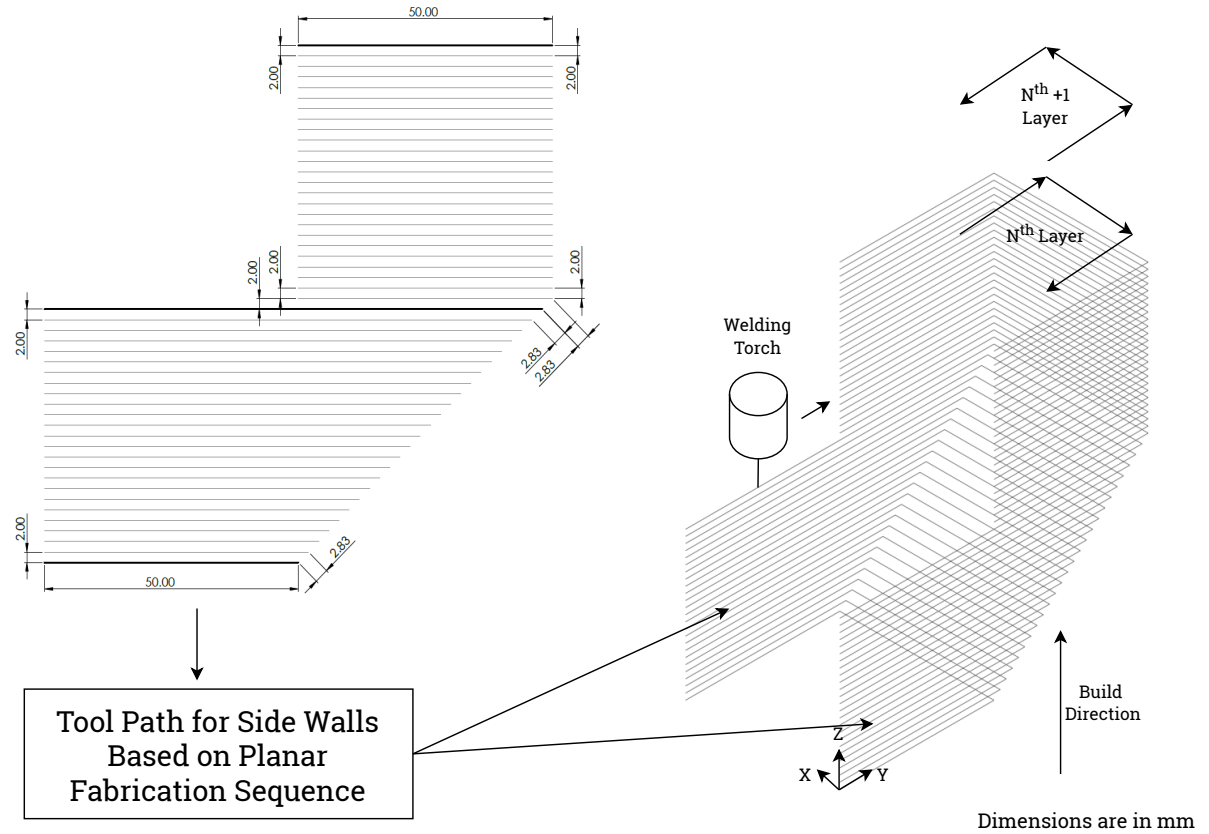
Figure 3.11: Tool path for planar fabrication sequence for 3D thin-walled structure
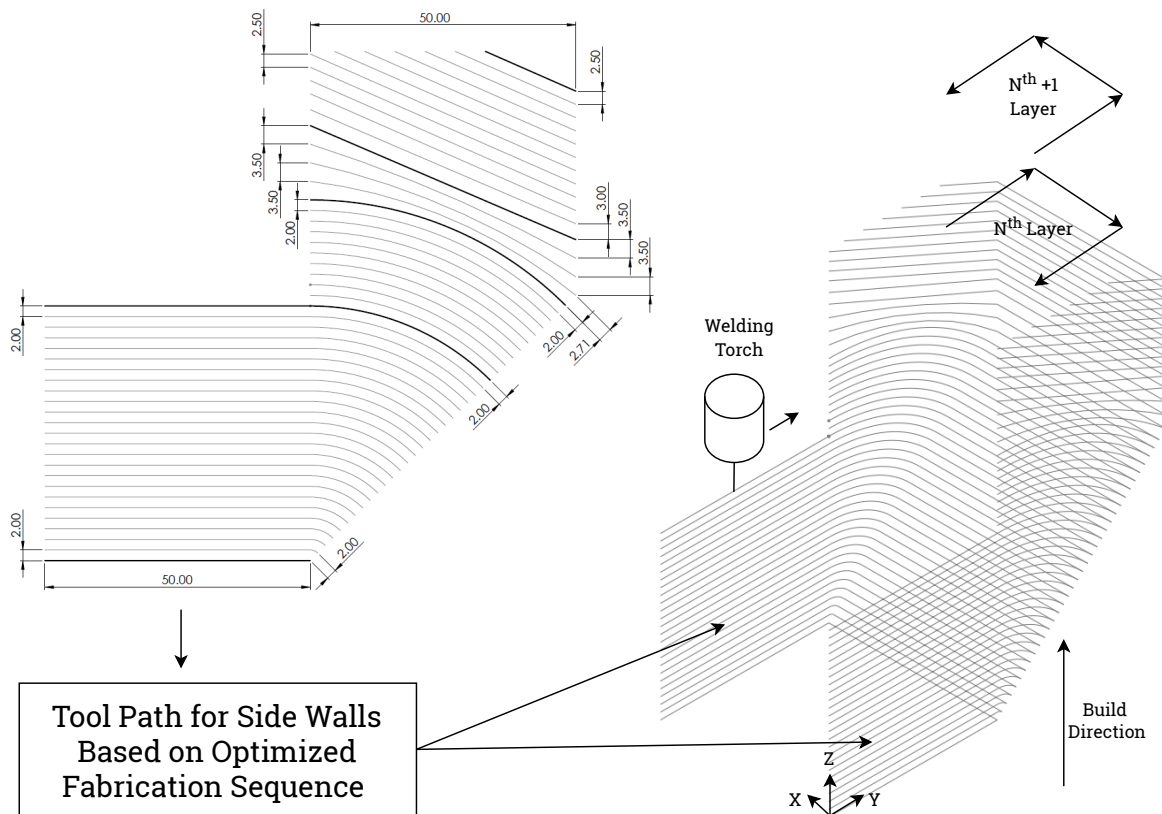
Figure 3.12: Tool path for optimized fabrication sequence for 3D thin-walled structure

Welding parameter				Substrate	Total layers	Layer height	Deposition Strategy
Wire feed rate (m/min)	Torch speed (mm/s)	λ'	Shielding Gas				
5.9	6	0.98	100 % Pure Argon at 16 lit/min	Al 6061	50	2 mm per layer	Planar
5.9	6	0.98	100 % Pure Argon at 16 lit/min	Al 6061	50	2 mm per layer	Optimized

Table 3.6: WAAM process parameters for 3D thin-walled structures

In WAAM, continuous welding is always desired, as intermittent start-stop action of welding arc within a layer can result in a large deviation from the desired shape. Regardless of continuous or intermittent welding, deviation from the intended shape at the beginning and end of deposition is always present in WAAM due to ignition and extinguishing of the arc. This problem is severe in the case of WAAM using Aluminum alloys due to a high heat sink effect as depicted in Fig.3.13a. To study the challenges in realizing WAAM with material deposition directed by fabrication sequence optimization, it is crucial to study the effects of weld start/stops in non-planar deposition from the point of view of the global geometric formation of the component. For example, it is intuitive that with symmetric material deposition if the weld start/stop are in different planes for different layers it will result in good geometrical formation. However, it is interesting to find out the geometric formation if the weld start/stop is in the same plane for different layers. To study the fabrication process with multi-weld start/stop in a single plane as described in Fig.3.13b, a fabrication sequence optimization process is carried out to maintain the flatness of the top surface of a test component as shown in Fig.3.12. The fabrication sequence optimization problem with uniform thickness control is implemented in MATLAB on a finite-element grid of 200 x 200 elements with 50 layers and solved with the help of gradient-based numerical optimization using the Methods of Moving Asymptotes (MMA) [87]. For a detailed explanation of the formulation and sensitivity analysis of this optimization problem, readers are requested to refer to [23]. The tool path is then constructed as per the layer deposition suggested by the optimized fabrication sequence

and it is used to fabricate the side walls of the 3D component as depicted in Fig.3.12.

(a) Geometric deviation due to weld start and stop

(b) Weld start/stop in multiple planes and single plane
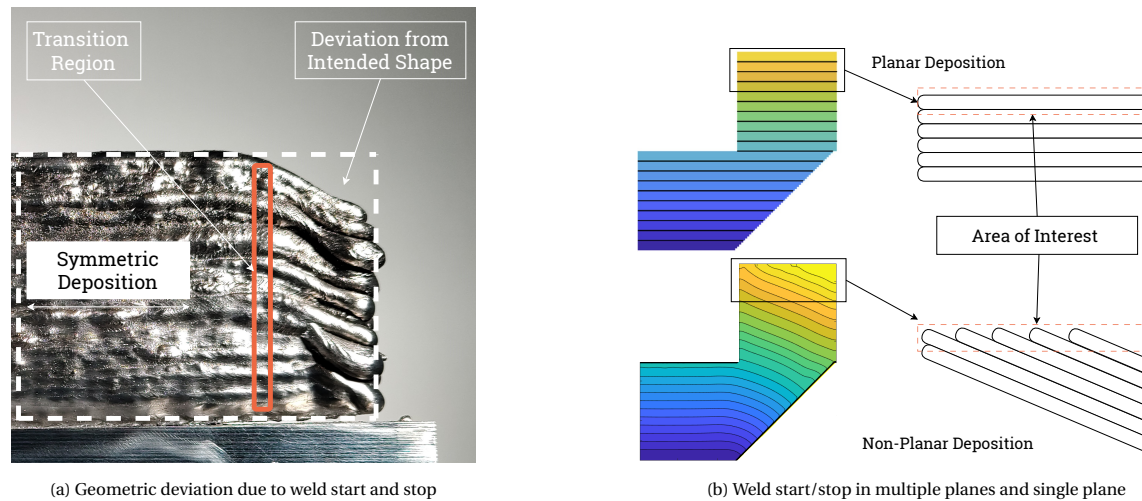
Figure 3.13: Strategies for studying the effect of weld start/stop in fabrication sequence optimization
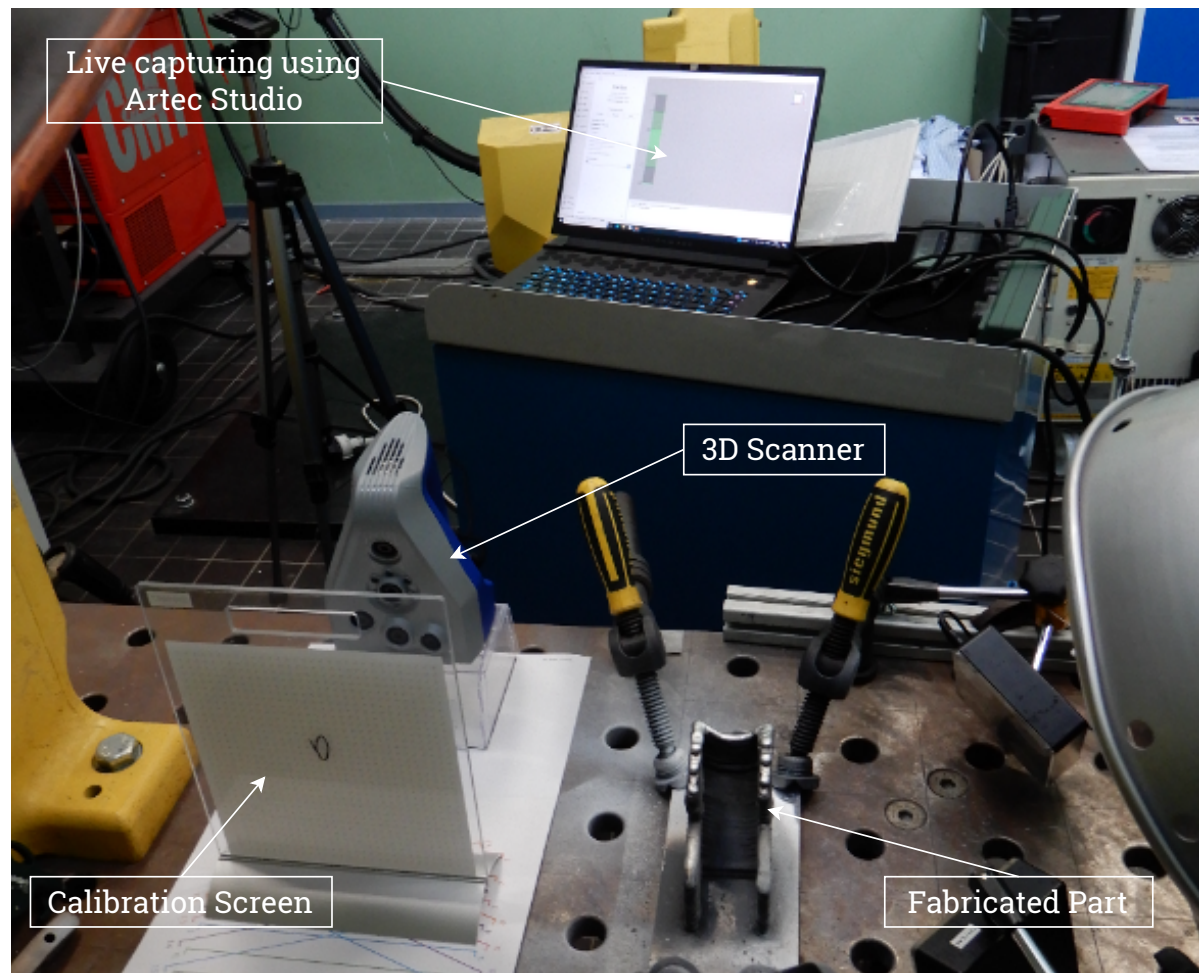
Figure 3.14: 3D scanning of the fabricated structure

Distortion measurement is necessary to study the effectiveness of fabrication sequence optimization. The fabricated structures are scanned using the Artec Space Spider 3D scanner by Artec 3D as shown in Fig.3.14. Two scans are performed for each part. The first scan is made after the fabrication is completed and the part is

cooled to room temperature and the second scan is after the part has been unclamped from the mounting table. After the post-processing, the final scanned models are aligned with the CAD models to analyze the global geometrical deviations. 3D scanning is a state-of-the-art method to quantify geometric variations, however, understanding the strain development in the previously deposited layers during a new layer deposition using a 3D scanning system is infeasible. Well-known contact-type measurement systems like strain gauges and linear variable differential transformers (LVDT) have been utilized to analyze in-situ strain development during AM processes, however, their use is justified for the strain measurement of the substrate on which the structure is fabricated. Considering the practical limitations and hurdles in implementing contact-type strain measurement, in this study in situ non-contact type strain measurements are performed using Digital Image Correlation equipment by LIMESS GmbH.
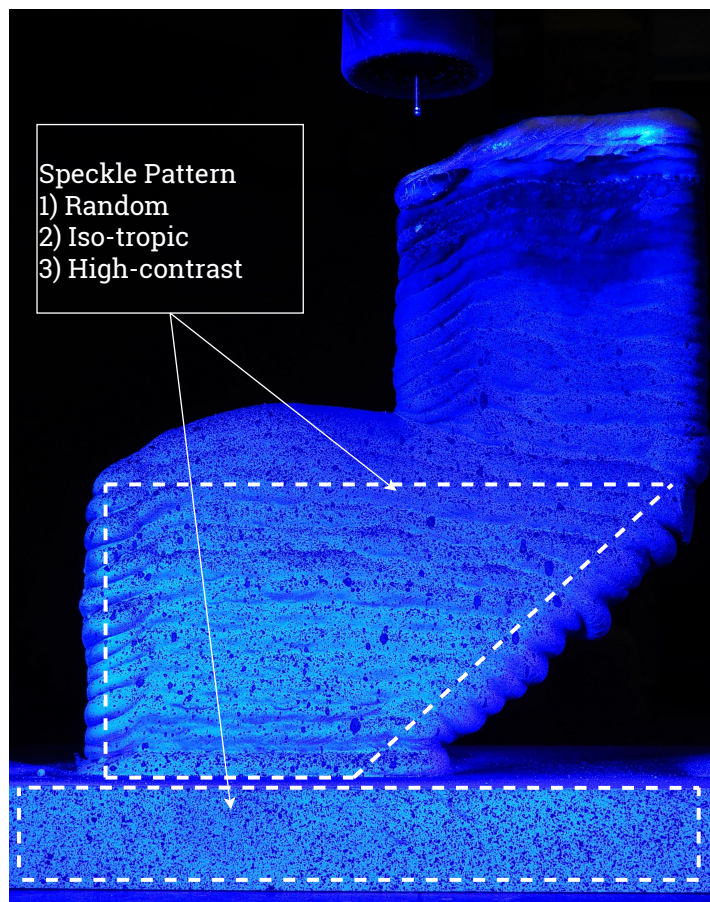
Figure 3.15: Spekle pattern on the fabricated structure and substrate

In digital image correlation, the movement of non-repetitive, isotropic, high-contrast pattern, so-called *"Speckle Pattern"* is traced throughout the deformation process, in this case during the deposition of the layers as shown in Fig.3.15. The DIC measurements are performed to study the strain evaluation of the substrate as well as the first 25 layers during the deposition of the last five layers of both deposition strategies. The measurement setup schematic is shown in Fig.3.16, it consists of a DIC camera connected to a data acquisition system and a central computer for calibration, record-triggering, and post-processing. The field of view captures the lower half of the side wall of the 3D shell structure and the substrate to track the motion of the printed speckle pattern. A metallic sheet is placed between the deposited structure and the camera to block bright arc light from the welding. To create contrast, first, a white color is applied to the deposited structure and then a black pattern is sprayed on the white background. The measurement sample is illuminated using a single wavelength (blue) light source to further enhance the contrast.

3
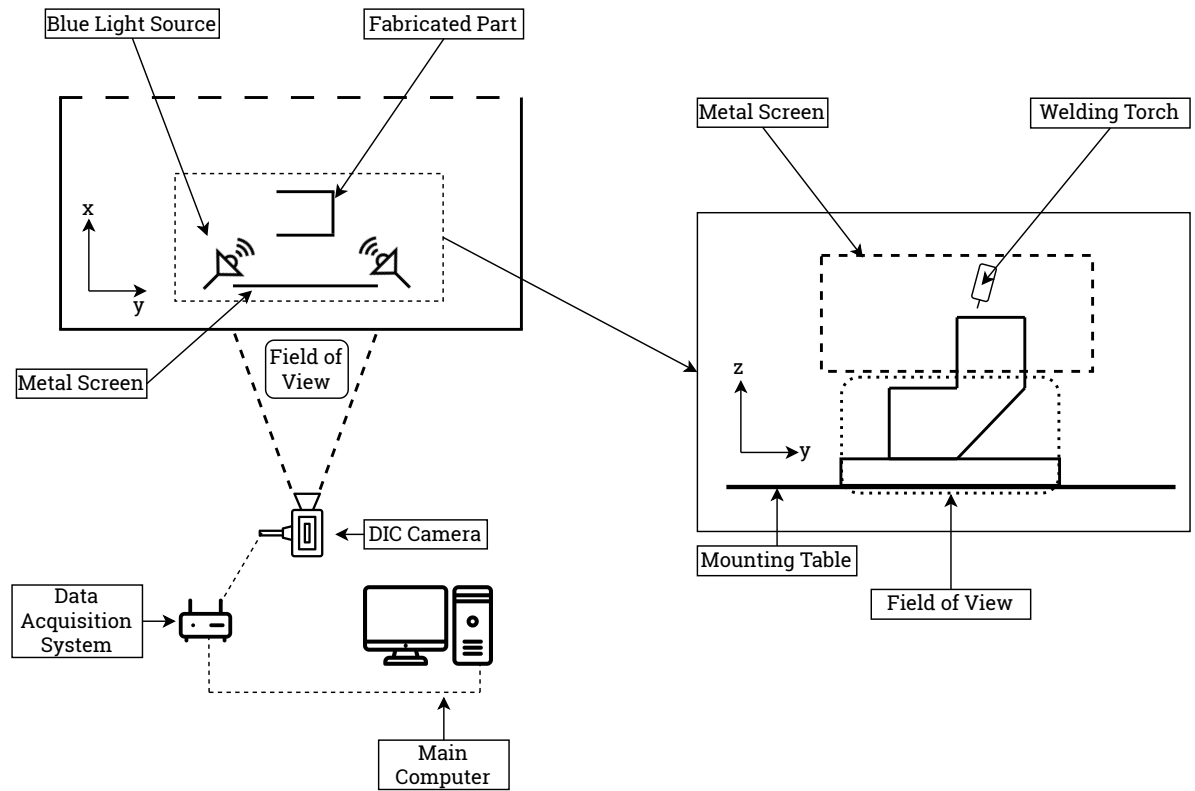
Figure 3.16: Schematic representation of DIC measurement setup
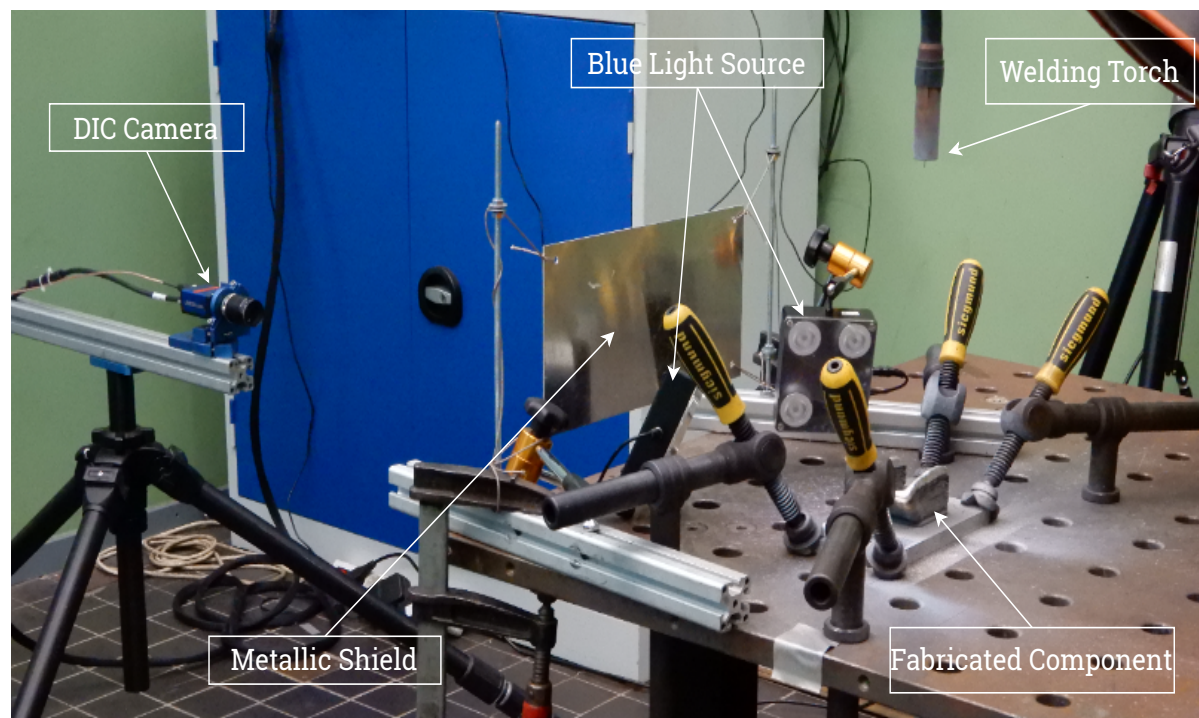
Figure 3.17: In-situ strain measurement using DIC measurement setup

3.5. FABRICATION RESULTS AND DISCUSSIONS

3.5.1. WELDING PARAMETERS FOR OPTIMAL BEAD QUALITY

The 2x2 factorial design experiment revealed the effects of extreme values of WFR and v_{Torch} on the quality of the bead formation. In Fig.3.18, the position of red squares corresponds to the values of WFR and v_{Torch} used in the factorial experiment with the left-bottommost square corresponding to Low(1), Low(2). When both parameters are low, the bead resulted in excessive material deposition, and low penetration with undercuts along with many humps as shown in Fig.3.18 (a). With low WFR and high v_{Torch}, similar results are observed except the reduced material deposition is considerably reduced, resulting in a narrow bead as depicted in Fig.3.18 (b). These two combinations are not suitable for WAAM as the deposited structure will collapse due to high-volume deposition with negligible weld penetration. For high WFR and low v_{Torch} as well as when both are high, the bead formation showed a smooth surface finish with virtually no humps as shown in Fig.3.18(d) and (c) respectively. However, in both cases, material deposition is considerably high causing flattened beads when the torch speed is low and excessively bigger beads when the torch speed is high. These combinations too are not suitable for WAAM due to their inherently high heat input.
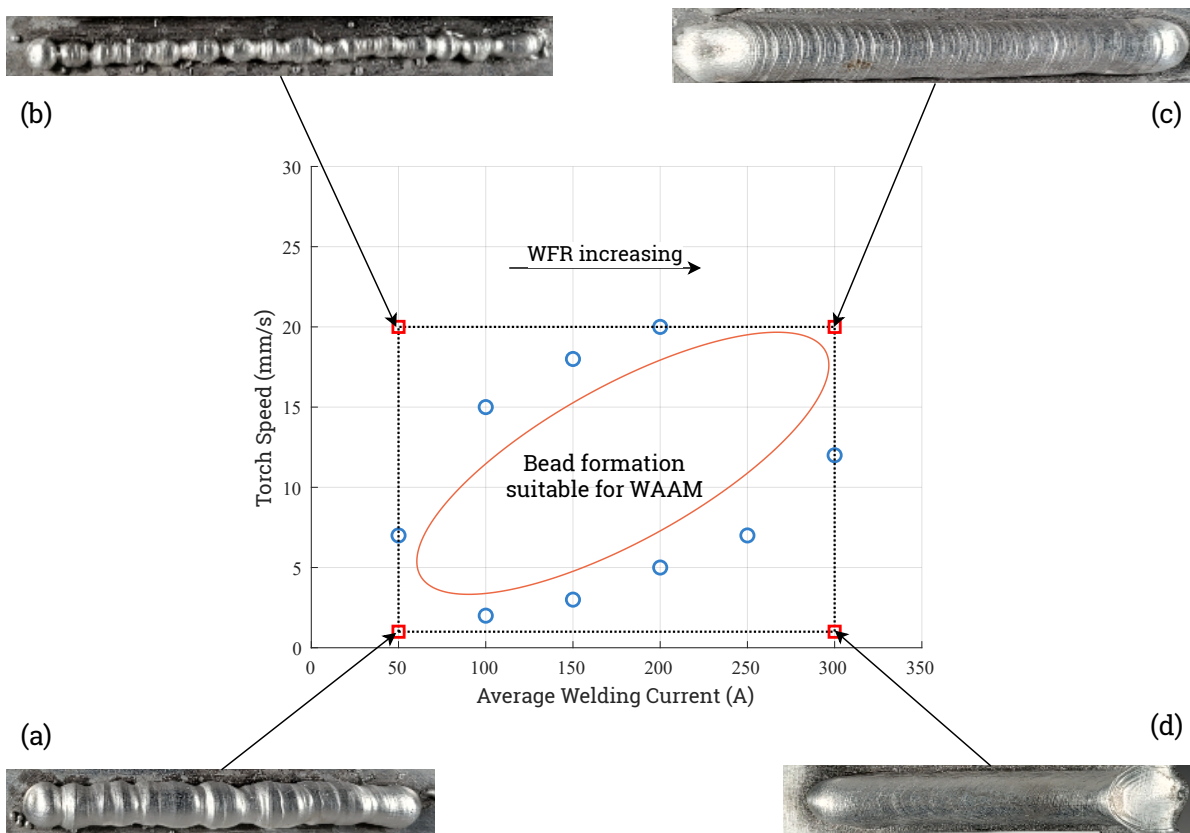
Figure 3.18: Bead formation with different combinations of WFR and v_{Torch}: (a) Both parameters Low, (b) Low WFR, High v_{Torch}, (c) Both Parameters High, (d) High WFR low v_{Torch}

After the factorial experiments, several beads are printed with WFR and v_{Torch} values corresponding to blue circles in Fig.3.18. The printed beads are observed for,

1. Welding spatter

2. Weld penetration

3. Deposition quality

4. Surface finish

5. Bead size and shape

The λ' combines WFR and v_{Torch}, thus is it calculated for all the beads, and based on the experimental ob-

servations a suitable range of λ' is presented in the table 3.7. From the factorial experiment, the value of λ' is 0.875 when both parameters are high, this value is within the suitable range, however, the heat input is considerably high, therefore, heat input has to be considered with λ' for a stable weld bead. Hence, the elliptical region presented in Fig. 3.18 gives a qualitative estimation of the suitable combinations for WFR and v_{Torch} for the WAAM using Aluminum 5xxx series alloys.

Current Range	λ' Range		Bead Characterisitcs					
			Excess Spatter	Excess Deposition	Humping	Low Penetration	Thin beads	Thick beads
Low Current 50-100 A	$0.4 < \lambda' < 3$	If below	✓		✓	✓	✓	
		If above		✓	✓	✓		✓
Medium Current 100-200 A	$0.5 < \lambda' < 3$	If below				✓	✓	
		If above		✓	✓			✓
High Current 200 A and above	$0.6 < \lambda' < 2$	If below		✓				✓
		If above		✓				✓

Table 3.7: λ' optimal range for 5xxx series aluminum WAAM

3.5.2. WELD BEAD CHARACTERIZATION

The outcome of the factorial experiment facilitated an understanding of the relationship between bead formation and the welding process parameters. The suitable process parameters are then used to print 9 beads as explained in Table 3.3. The weld bead cross-sectional measurements using image processing in *Fiji-Image J* [85] is shown in Fig.3.19. The scale presented on the microscopy images of the weld cross-sections is used to calibrate the pixel per mm data. Weld bead width is measured using a gauge (yellow line in Fig.3.19) plotted on the image, showing 12.989 mm. Similarly, a closed polygon is drawn along the shape of the bead cross-section to measure its area. Each bead is cut at four different locations, creating in total of 6 faces for measurements. The bead width w, height h, and area of the cross-section are measured for each face and the average values are reported in Table 3.8. For the measured height and width, areas for parabolic, cosine, and arc shapes are calculated with the help of equations given in Table 3.4. The calculated areas are compared with the measured area and the errors are tabulated in Table 3.9. The relative error tabulated above indicates that bead formation follows an arc shape. Arc shape beads are suitable for WAAM provided the wetting angle is more than 90° degrees to avoid undercutting as shown in Fig.3.20. From the microscope images, it is observed that the wetting angle is more than 90° for all bead cross-sections.
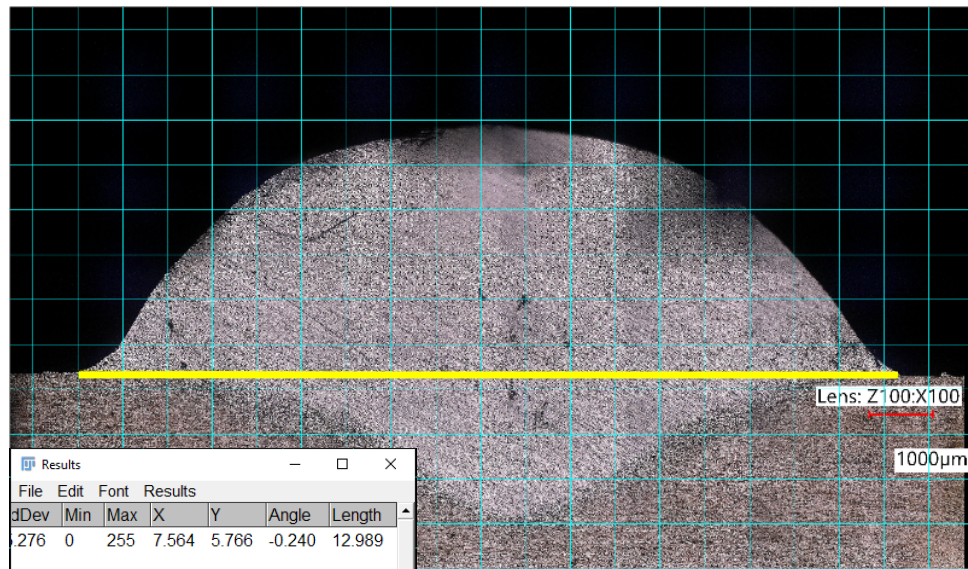
Figure 3.19: Sample bead length measurement in mm

Bead Number	Current (A)	WFR (m/min)	v_{Torch} (mm/s)	Measured Data		
				w_{avg} (mm)	h_{avg} (mm)	Area (mm²)
1			5	6.80	4.13	23.39
2	100	5.9	4	7.43	4.78	28.99
3			3	8.46	5.45	38.31
4			7	8.05	3.55	22.78
5	130	7.5	6	8.72	3.72	25.39
6			5	9.12	4.12	29.99
7			7	9.81	3.70	25.74
8	150	9.3	6	10.96	3.89	30.23
9			5	12.47	3.96	35.81

Table 3.8: Measured geometric data for 9 beads

Bead Number	Measured Area (mm²)	Calculated Area (mm²)			Error (%)		
		Parabola	Cosine	Arc	Parabola	Cosine	Arc
1	23.39	18.72	17.87	23.42	24.98	30.88	0.09
2	28.99	23.69	22.62	30.3	22.4	28.18	4.3
3	38.31	30.76	29.37	39.34	24.56	30.44	2.6
4	22.78	19.08	18.22	21.79	19.39	25.03	4.55
5	25.39	21.62	20.64	24.50	17.46	23.01	3.64
6	29.99	25.07	23.94	28.8	19.63	25.28	4.17
7	25.74	24.20	23.11	26.77	6.38	11.4	3.83
8	30.23	28.37	27.09	31.05	6.54	11.56	2.66
9	35.81	32.94	31.46	35.47	8.69	13.82	0.95

Table 3.9: Relative error between calculated and measured area for parabola, cosine, and arc shape
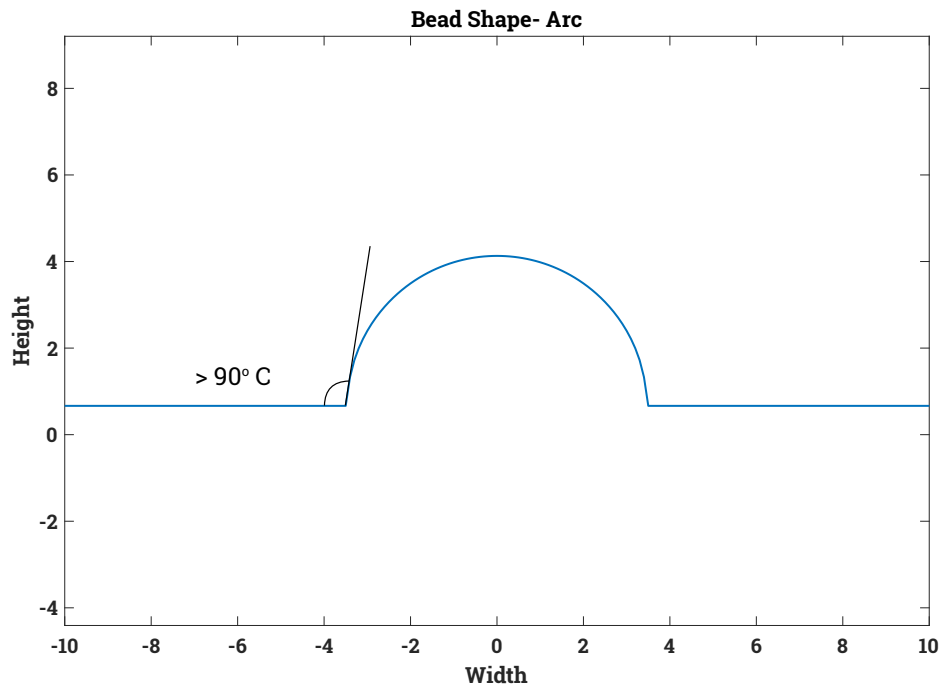
Figure 3.20: Wetting angle for arc shape bead

For this arc shape bead profile, the relationship between welding process parameters and bead dimensions can be established. The deposition volume rate ($\dot{v}_d$) during bead printing can be calculated as,

$$\dot{v}_d = Area_{Bead} \times v_{Torch} \tag{3.6}$$

$$\dot{v}_d = Area_{Wire} \times WFR \tag{3.7}$$

From equation 3.6, 3.7, and 3.3 the following relation can be established,

$$Area_{Bead} = Area_{Wire} \times \lambda \tag{3.8}$$

The area of the wire is $\frac{\pi}{4}d^2$ where d is the wire diameter, also the bead area for arc shape is stated in Table 3.4. Substituting the area of arc shape and wire into equation 3.8, the following equation can be derived to predict the dimensions of the bead.

$$\arccos\left(\frac{-b}{a}\right)a^2 + \frac{wb}{2} = \frac{\pi}{4}d^2 \quad \lambda$$

$$\arccos\left(\frac{w^2-4h^2}{w^2+4h^2}\right)\left(\frac{w^2+4h^2}{8h}\right)^2 + \frac{w}{2}\left(\frac{4h^2-w^2}{8h}\right) = \frac{\pi\lambda d^2}{4}$$

$$\arccos\left(\frac{w^2-4h^2}{w^2+4h^2}\right)\left(\frac{w^2+4h^2}{8h}\right)^2 = \frac{16\pi\lambda hd^2 - 16wh^2 + 4w^3}{64h}$$

This can be further simplified to

$$4h^2 + \cos\left(\frac{4h\left(-4h^2w + 4\lambda\pi hd^2 + w^3\right)}{\left(4h^2+w^2\right)^2}\right)\left(4h^2+w^2\right) = w^2 \tag{3.9}$$

Such that $4h^2 + w^2 \neq 0'$

3.5.3. Fabrication of Single-Bead Multi-layer Walls

The results from the bead characterization are then utilized to fabricate thin-wall structures consisting of multiple layers with a single bead in each layer. Three sets of wall structures are fabricated with process parameters and inter-layer temperature explained in Table 3.5. The constant dwell time as well as high (above 120° C) inter-layer temperature result in increasing wall width and depression in layer height along the build direction. However, inter-layer temperatures are maintained within 90-50° C and kept at those values during the entire deposition, hence, uniformity in the dimensions is observed. The measured data is tabulated in Table 3.10. The visual inspection along with measured dimensions of all 9 walls revealed the effect of the inter-layer temperature on the geometrical formation is not significant, however, the effect of z-axis motion after each pass significantly affected the fabrication. In set 3, where the displacement of the welding torch is 3.5mm after each pass, a considerable change in dimensions is observed, e.g., for walls 7,8, and 9, despite 160mm torch travel, deposited walls have lengths 130, 140, and 125mm respectively along the same direction. When the z-axis motion of the torch after each pass is 3.5mm or more, it results in a large wire stick-out. More stick-out at the same applied voltage reduces the current and therefore heat input also reduces considerably. This is the primary reason for the excessive geometric deviation at weld start-stop regions.

Set No.	Wall No.	Measured Dimensions			
		Length (mm)	Width (mm)	Height (mm)	Height per Layer (mm/layer)
1	1	170	12	62	2.067
	2	170	12.5	63	2.1
	3	166	11	65	2.167
2	4	165	12	56	1.867
	5	165	12	58	1.933
	6	162	12	55	1.964
3	7	130	13.5	62	2.067
	8	140	13.5	55	1.964
	9	125	13.5	55	2.037

Table 3.10: Single bead multi-layer walls dimensions after fabrication

Wall 7
Inter layer Temerature = 90° C

Wall 8
Inter layer Temerature = 70° C

Set 3
WFR = 9.3 m/min
v_{Torch} = 7 mm/s

Wall 9
Inter layer Temerature = 50° C
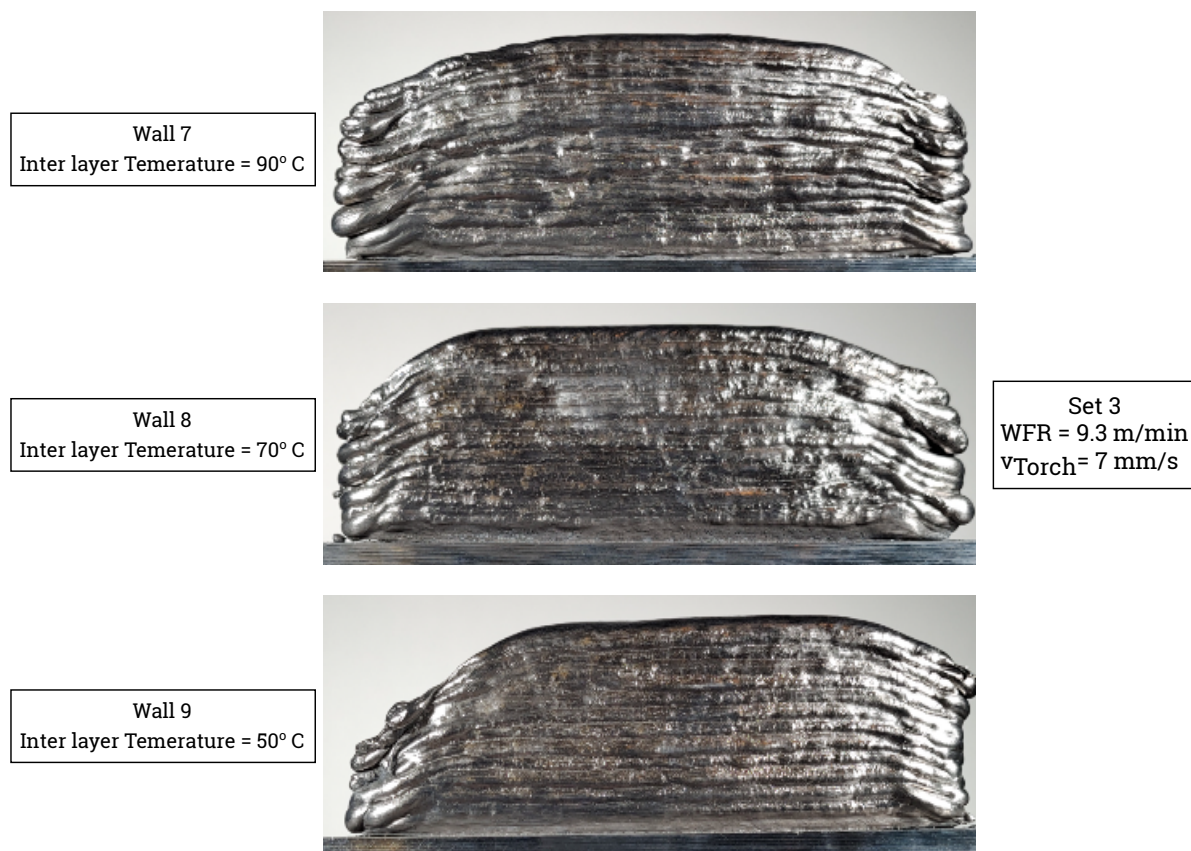
Figure 3.21: Uncontrolled material deposition due to excessive stick-out length in walls from set 3 from Table 3.5

3.5.4. FABRICATION OF 3D THIN-WALLED STRUCTURES

The study of welding parameters for a single bead formed the basis for further development. The optimized welding parameters, kinematic system motion, and inter-layer temperature determined in previous fabrication experiments are utilized to fabricate the 3D thin-walled shell structures. The fabrication of these structures is carried out by depositing the material in a planar and optimized fabrication sequence, the rest of the parameters and settings are kept the same. The purpose of this approach is to study the effect of two material deposition strategies provided everything else during the process is the same. The fabricated structures are depicted in Fig.3.22 and 3.23.
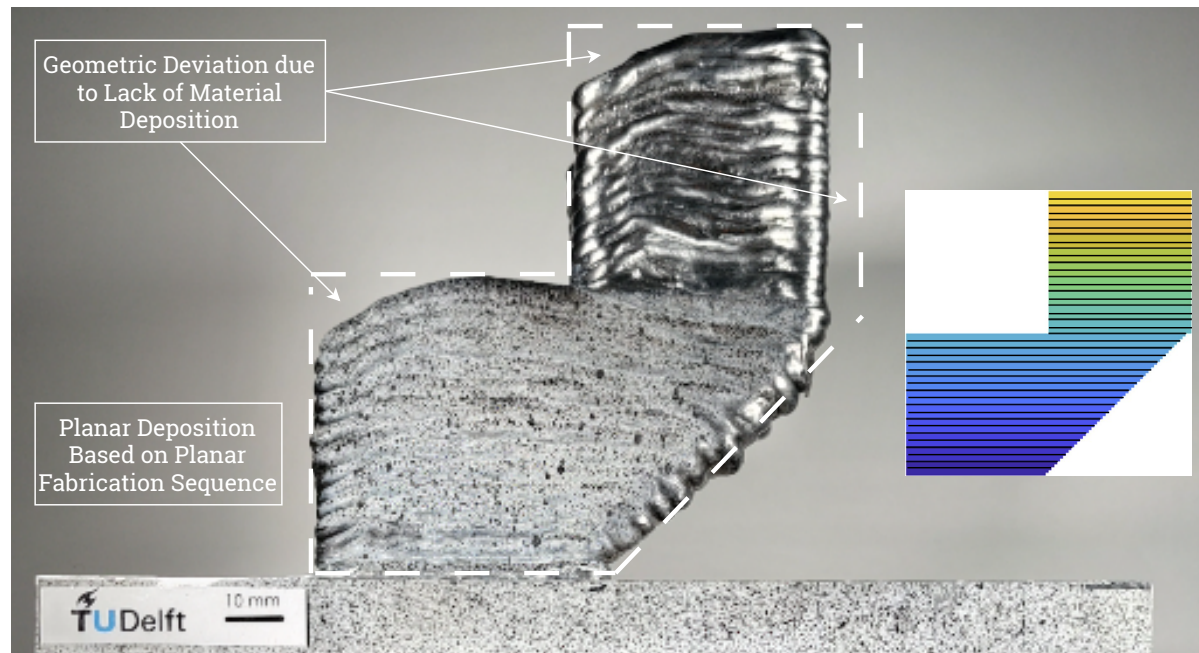
Figure 3.22: WAAM of 3D thin-walled structures using planar fabrication sequence
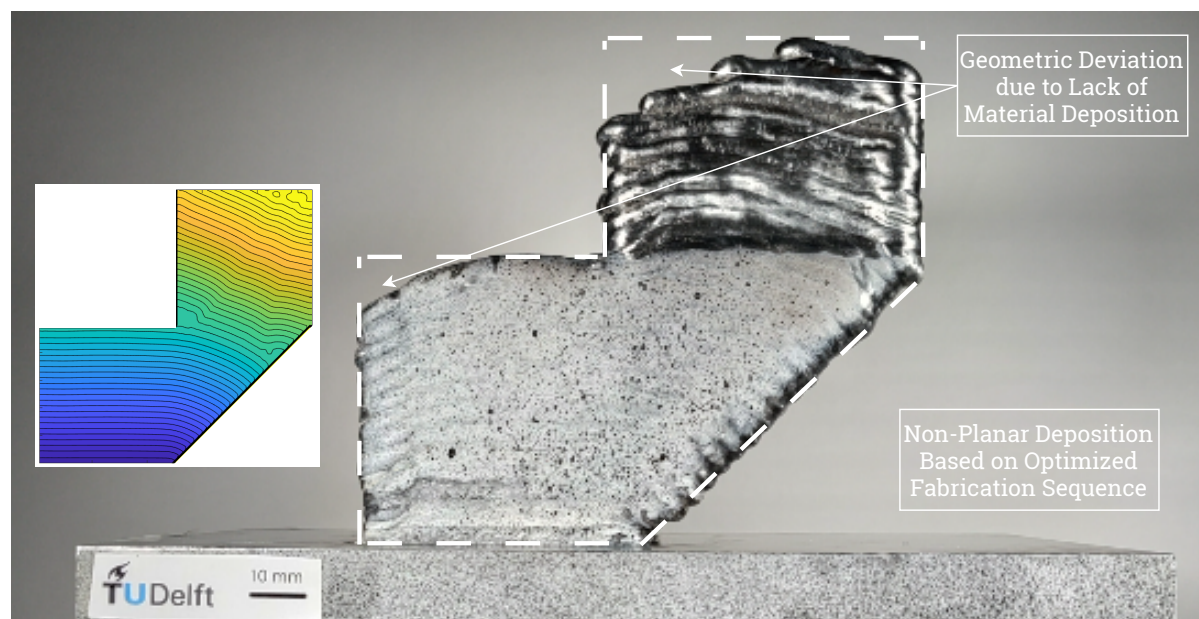
Figure 3.23: WAAM of 3D thin-walled structures using optimized fabrication sequence

The tool path for both fabrication sequences has a similar starting and ending for the first 25 layers. The height drop due to welding start/stop characteristics is observed in both strategies. In planar fabrication, the tool path advancement after each layer in the overhang region is greater than that of non-planar fabrication, as depicted in Fig.3.11. This resulted in a discontinuous material deposition and a gradual decrease in part dimensions in the overhang as well as the top region of the fabricated component as presented in Fig. 3.22. This aspect is improved in optimized fabrication as the tool path followed a curvature in the overhang region, resulting in a smooth and continuous material deposition as shown in Fig.3.24. As the overhang region formed the base for the top region, improved overhang resulted in a smaller geometric deviation of the top region as depicted in Fig.3.23. One critical observation from these experiments is that an optimized fabrication sequence can result in transition regions such that the previous layer has non-planar material deposition and the next layer has a planar deposition. Such transition can lead to uneven material distribution and seri-

ously affects the subsequent layer formations. This can be seen in Fig.3.24 (c), the transition region affected the material deposition in the top region resulting in significant sagging in the top region. This effect is not observed in the planar fabrication due to the absence of the planar-non-planar transition and it can be seen in Fig.3.24 (d).

3
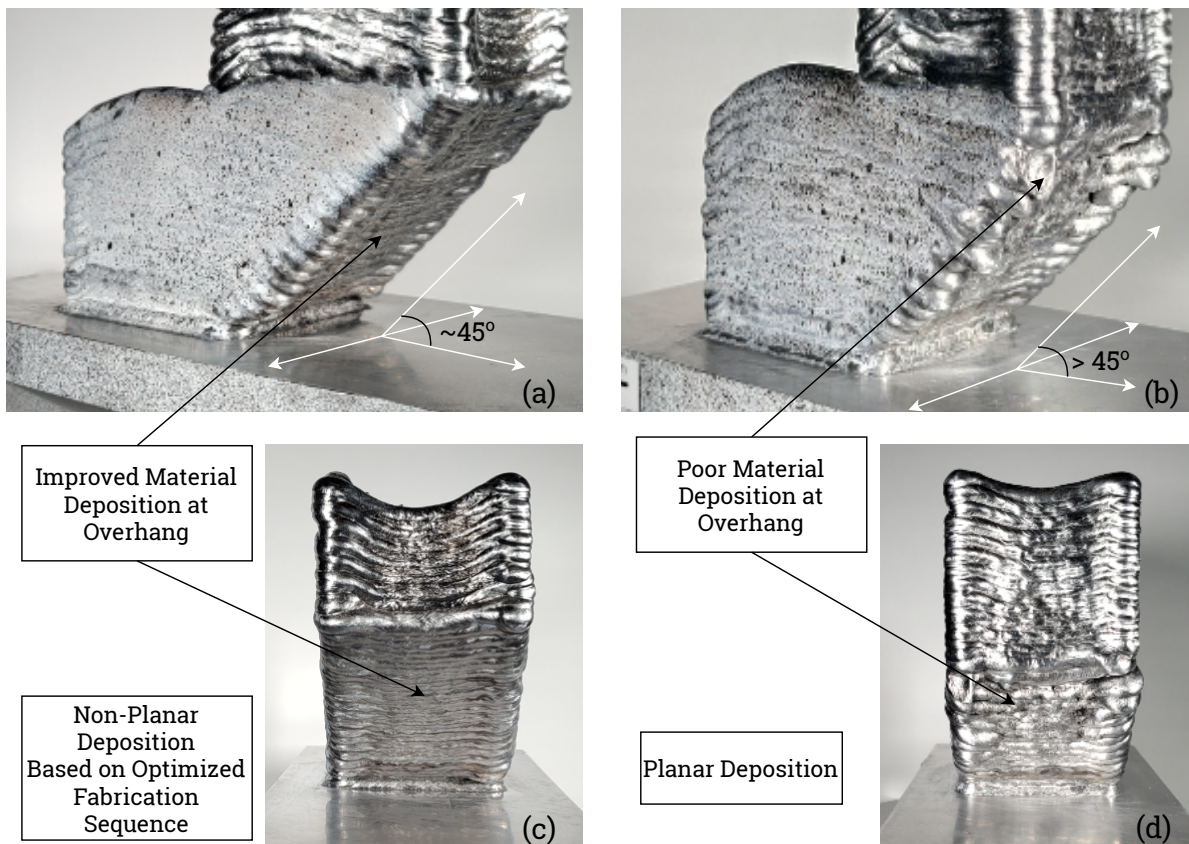
Figure 3.24: Overall geometric formation and material deposition in overhang region in WAAM of L-shaped thin-walled structures with planar and optimized fabrication sequence using aluminum 5xxx series alloy wire

3.5.5. 3D Scanning

The bead dimensions for the weld parameter used in fabricating the 3D thin-walled shell structures are in the order of 10 mm and due to the melting and solidification of the wire a straight horizontal bead with torch travel of 50mm would result in a bead of length of approximately 60mm. Considering this effect of the weld start-stop on the final dimensions of the bead, a CAD model is designed in SOLIDWORKS according to the tool path dimensions described in Fig.3.11. The constructed CAD file is then imported into Artec Studio software [88] and overlapped with the post-processed scanned geometries to study the deviations of deposited structure from the intended geometry. For planar deposition, the material deposition in the overhang region is insufficient resulting in considerable deviation of the upper part from the intended form as shown in Fig.3.25 on the other hand, this deviation is less for optimized deposition as seen in Fig.3.26. As the starting of the tool path for both fabrication sequences is similar for the first 25 layers, both depositions resulted in a bulged lower flange of the L-shaped structure, this deviation is 9.12mm for planar deposition and 8.18mm for optimized deposition. The excessive material visible in the scanned geometry shown in Fig.3.26, is due to a lack of scanned points in that region resulting in erroneous patching surface. This indicates the challenges in scanning a deposited structure when it is clamped to the mounting table, and this problem can be extrapolated for structures with complex geometries.
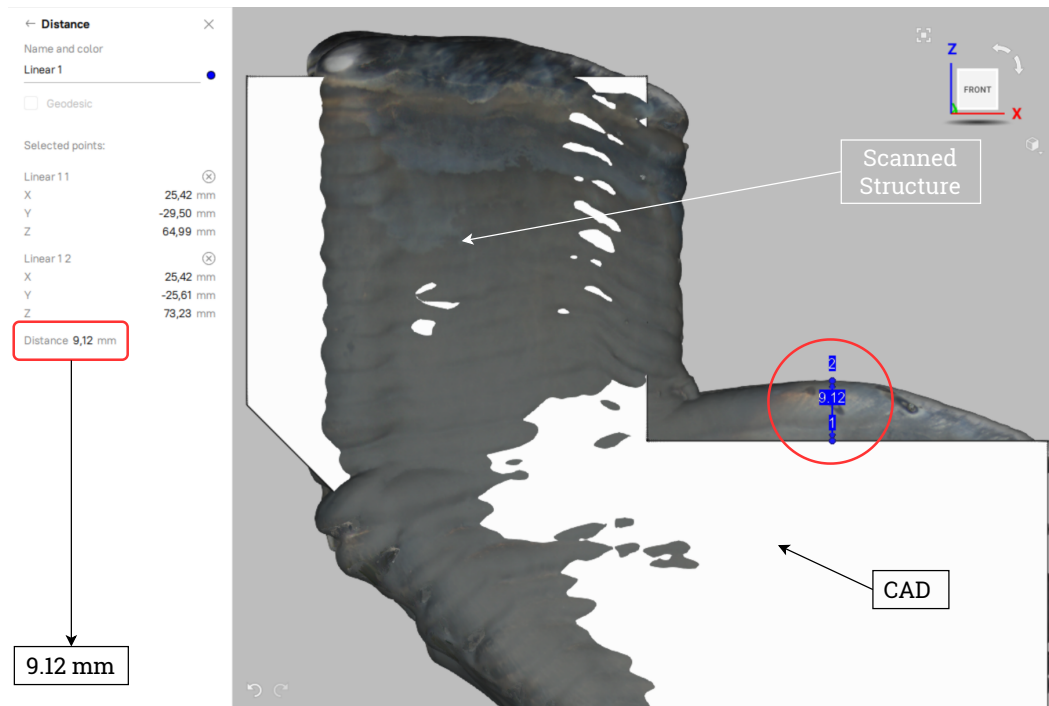
Figure 3.25: Scanned model overlapped with the deposited structure with planar fabrication
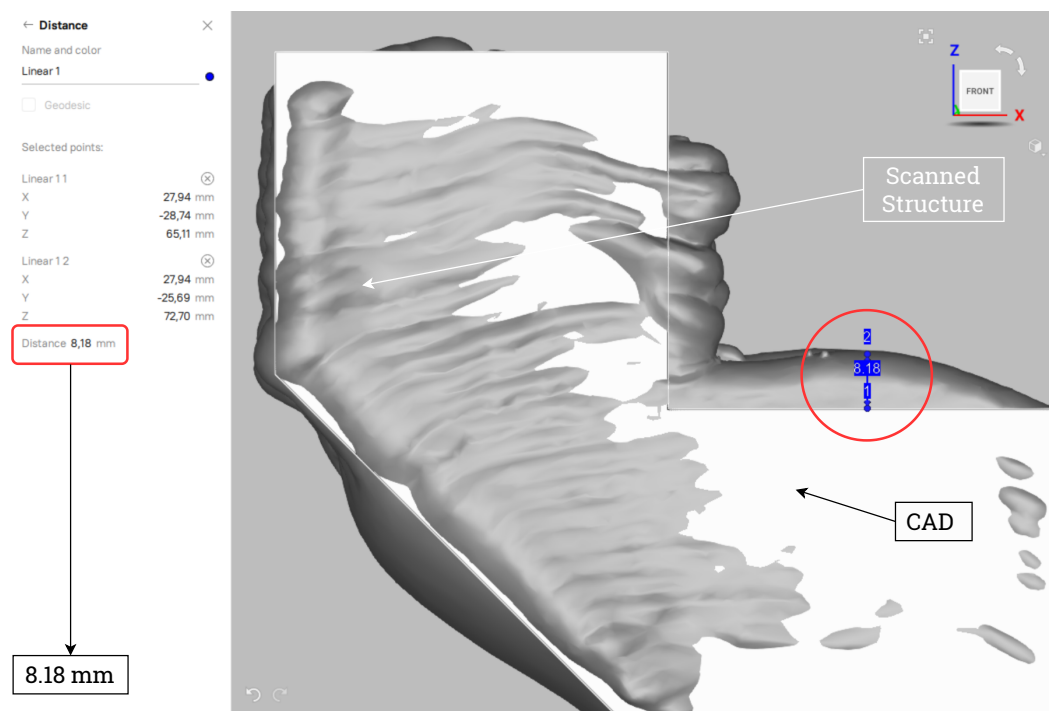
Figure 3.26: Scanned model overlapped with the deposited structure with optimized fabrication

3.5.6. STRAIN MEASUREMENT

Since the process parameters are the same for planar and optimized fabrication strategies, strain development during printing is also critical to the study. A DIC measurement is performed during and after printing for both deposition strategies. During the post-processing 4 line gauges are set in DIC frames and strain and displacement of those gauges are calculated using the image correlation process. The initial lengths of the 4

gauges are tabulated in Table 3.11 and depicted in Fig.3.27.

Gauge No.	S1	P1	P2	P3
Initial Length l' (mm)	95	40	45	75

Table 3.11: Lengths of gauges used in DIC post-processing

During the DIC measurements, for each deposition strategy, two sets of frames are captured and analyzed separately. The first set consists of frames captured during fabrication and the second set consists of frames captured during unclamping. Within each set, the length of a gauge (l) in every frame is calculated using the image correlation principle. These lengths are compared with the initial gauge lengths to calculate the change in length (Δl) for all frames. Afterward, strain in the gauge for frames is calculated using the strain-displacement relationship,

$$Line\ Strain = \frac{\Delta l}{l'} \tag{3.10}$$
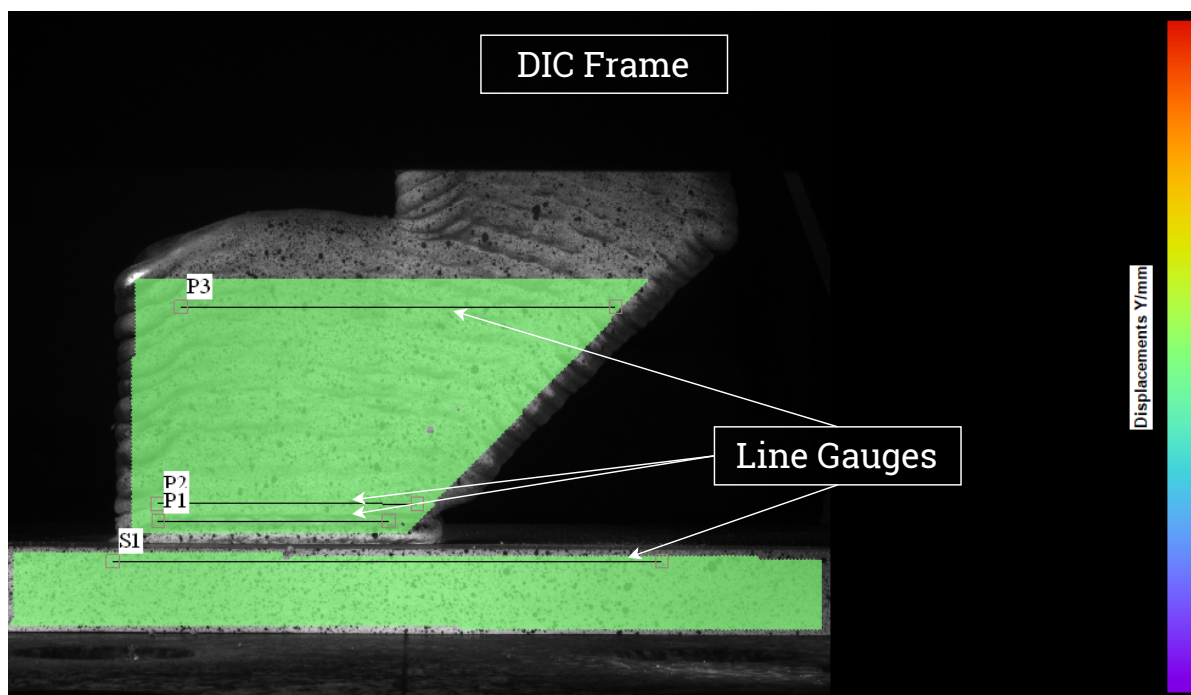
Figure 3.27: DIC screen with four line gauges S1(on substrate), P1, P2, and P3 on the previously deposited region

These strain values for gauges S1 and P3 during fabrication using both fabrication strategies are plotted in Fig.3.28 and 3.29 respectively. From the DIC measurements, the gauge placed on the substrate shows high strain for planar deposition and relatively low strain for non-planar material deposition during as well as in between depositions of the last 5 layers. The gauge placed on the deposited part, however, shows a different behavior during the deposition such that for the 46th layer, strain is relatively higher for planar deposition than non-planar deposition. But the trend is reversed for the next layer and again for the next-to-next layer till the final layer. The same gauge shows a constant trend of higher strain in planar deposition than in non-planar deposition in between the fabrication of two successive layers. In between the successive layer deposition, the inter-layer temperature is kept at room temperature thus the effect of thermal strain has vanished and therefore, the response of gauge P3 is based on the residual strain alone. Thus for gauge P3, the high-low fluctuation can be neglected. Hence for P3 as well the strain is higher for planar deposition.
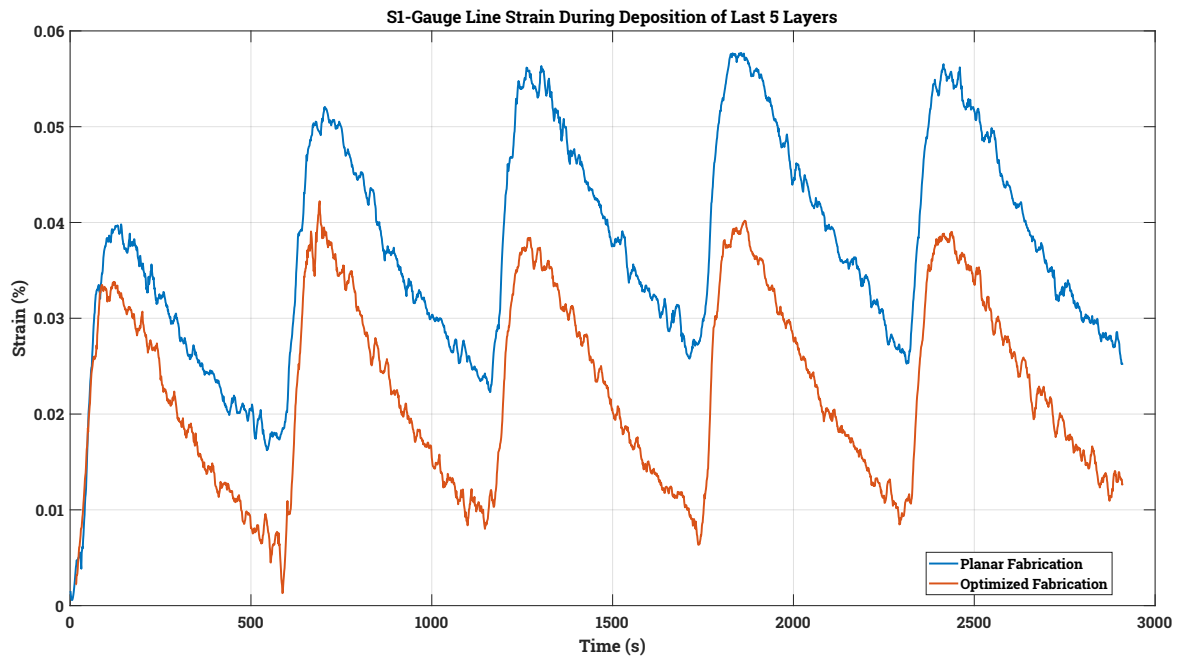
Figure 3.28: Line strain in sauge S1 placed on the substrate
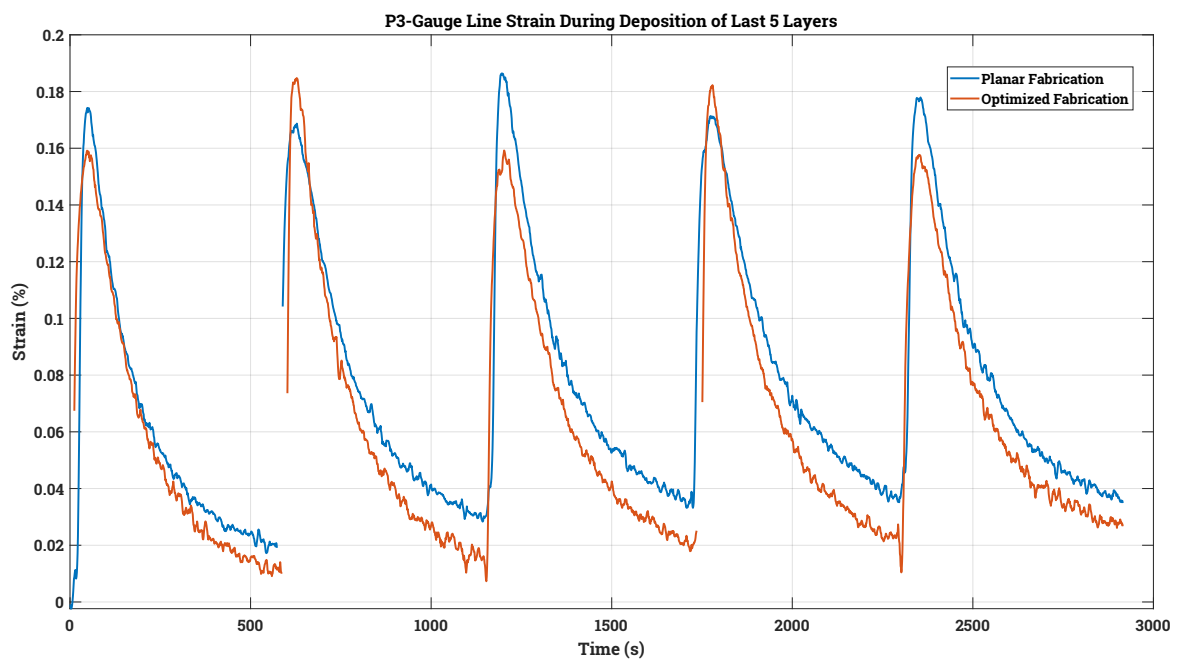
Figure 3.29: Line strain in gauge P3 placed on the deposited structure

3.6. Conclusions

In conclusion, the presented research employs Wire Arc Additive Manufacturing (WAAM) for building metal structures, with the material deposition governed by a fabrication sequence optimization algorithm to minimize a given measure of distortion. Furthermore, 3D scanning and strain measurement using DIC showed a reduction in distortion for optimized material deposition. When processing Aluminum alloys or WAAM-suitable material with a high thermal expansion coefficient (CTE), an optimized fabrication sequence results in improved geometric formation, especially overhang features. This can be translated to the effectiveness of optimized deposition for materials with low CTE. The results from distortion measurements show less strain development for optimized fabrication compared to planar fabrication, forming a qualitative experimental validation of the simulation results of distortion minimization using an optimized fabrication sequence.

The experiments revealed that the quality of the fundamental part of WAAM-a single weld bead depends particularly on wire feed rate(thus welding current/voltage) and torch travel speed. Since several beads overlap horizontally, and or vertically to form a material layer, the deposition quality of the final structure depends on the weld process parameters along with the fabrication sequence. The λ parameter captures the wire feed rate and torch speed. The relationship between λ and predicted bead dimensions can be derived for a given material similar to the one derived for aluminum 5xxx series alloy in this research. This relation can be utilized as a dimension constraint in the optimization algorithm to limit layer size during the optimization process.

The observed effect of inter-layer temperature on overall build-up during WAAm for Aluminum alloys is insignificant provided the temperature is maintained below 120 °C. However, this could not be the case for other materials, and keeping the inter-layer temperature at room temperature could result in welding defects for different materials. Therefore, strain calculation during the optimization should consider the temperature gradient between solidus and inter-layer temperature. Currently, the material accumulation and geometric devotion at weld start/stop points are not considered in fabrication sequence optimization. These deviations alter the input weld process parameters and in the end final distortion. This can be addressed by calculating strains considering the high heat input at the beginning of the weld bead.

In-situ strain measurement is highly useful for calibrating the optimization algorithm. In this research, a 2D strain field measurement is performed, however, due to the arc shape of the weld bead the surface of the deposited structure exhibits waviness, hence to accurately measure the 3D strain field an advanced multi-camera 3D DIC system can be utilized in future experimental research. Moving forward, future research should aim to process different materials in WAAm to study the response of optimized fabrication sequences on overall manufacturing and distortion. An optimized fabrication sequence considering welding aspects, predicted bead dimensions and variable heat inputs can result in a deposited structure that is a true near-net representation of the desired geometry, which further facilitates the experimental validation of the fabrication sequence optimization.

3

RESULTS AND DISCUSSION

4.1. OPTIMAL BEAD CHARACTERISTICS

The two independent factors, WFR and v_{Torch} are varied according to the 2x2 factorial experiment. The four combinations of the parameters are shown in red squares in Fig.4.1 and the beads are evaluated for welding spatter, weld penetration, deposition quality, surface finish, and overall bead size and shape. When both parameters are set to low values (case 1), the bead exhibited excessive material deposition, low penetration, undercuts, and humps on the bead surface, also when both parameters are set to high values (case 4) the bead formation demonstrated excessive material deposition, smooth surface finish with minimal humps. For the other two cases, low wire feed with high torch speed (case 2) behaves similarly to case 1, except for a significantly reduced material deposition resulting in a narrower bead. The case 3 results are similar to case 4, with a more flattened weld bead. These combinations are also unsuitable for WAAM due to the inherently high heat input.
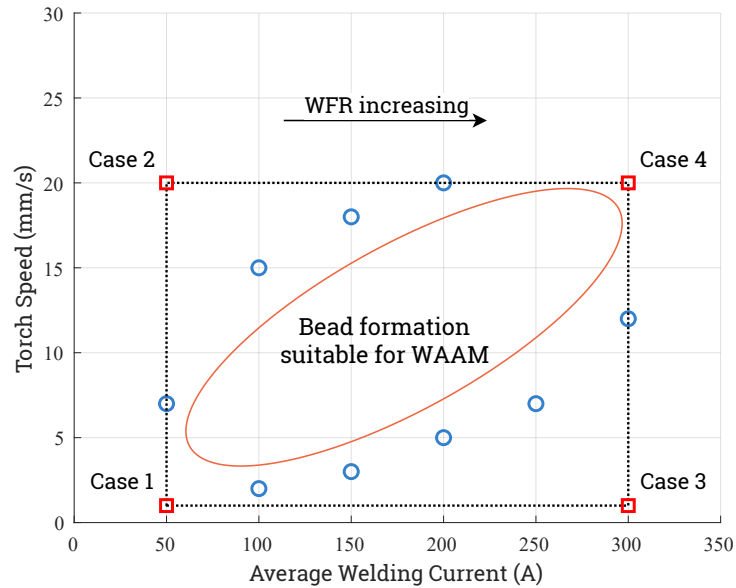
Figure 4.1: Bead formation with different combinations of WFR and v_{Torch}. Case 1:Both parameters Low, Case 2: Low WFR, High v_{Torch}, Case 3: High WFR low v_{Torch}, and Case 4: Both Parameters High

Upon printing several beads with the WFR and v_{Torch} combinations indicated by the blue circles in Fig.4.1. For Al 5356 wire, the experimentally observed ranges of $\lambda^{'}$ suitable for WAAM for different welding currents are as follows;

1. 50 to 100 A: $0.4 < \lambda^{'} < 3$

2. 100-200 A : $0.5 < \lambda^{'} < 3$

3. 200 A and above: $0.6 < \lambda^{'} < 2$

In the factorial experiment, a $\lambda^{'}$ value of 0.875 was observed when both parameters were high, falling within the suitable range. However, the heat input was considerably high, indicating that heat input must be considered alongside $\lambda^{'}$ to achieve a stable weld bead. Thus, the elliptical region in Fig.4.1 provides a qualitative estimation of the optimal WFR and vTorch combinations for WAAM using Aluminum 5xxx series alloys.

The way welding parameters affect the bead quality, they also affect the bead dimensions. In fabrication sequence optimization, in the current stage, the layer height is determined by total volume and number of stages with the number of stages being an independent parameter. Therefore, from an optimization perspective, a given part can be divided in N or M number of stages such that N < M or N > M. In actual fabrication, a certain welding parameter set results in certain bead dimensions and the number of stages for the given volume of the part. If the material deposition for the same part is optimized using fabrication sequence optimization. The layer height in the simulation could vary from the actual height. Integrating a relationship between welding parameters, wire diameter, and bead dimension into the optimization could be a way to tackle this problem. The 9 beads are printed with suitable WFR and v_{Torch} combinations corresponding to the elliptical region of Fig.4.1 to study the bead shape and dimensions. The measured height and width are used to calculate the area for three shapes parabola, cosine, and arc respectively. When calculated areas are compared with measured area values for all the beads, the results indicate that beads follow arc shape with very low relative errors as given in Table 4.1.

Bead Number	Error		
	Parabola	Cosine	Arc
1	24.98	30.88	0.09
2	22.4	28.18	4.3
3	24.56	30.44	2.6
4	19.39	25.03	4.55
5	17.46	23.01	3.64
6	19.63	25.28	4.17
7	6.38	11.4	3.83
8	6.54	11.56	2.66
9	8.69	13.82	0.95

Table 4.1: Relative error between calculated and measured area for parabola, cosine, and arc shape

For the arc shape, based on the volume deposition rate, the following relationship can be established to relate λ (capturing wire feed rate and torch speed), bead height h, bead width w, and wire diameter d,

$$4h^2 + \cos\left(\frac{4h\left(-4h^2 w + 4\lambda\pi h d^2 + w^3\right)}{\left(4h^2 + w^2\right)^2}\right)\left(4h^2 + w^2\right) = w^2 \tag{4.1}$$

Such that $4h^2 + w^2 \neq 0'$

4.2. Fabrication using Multi-axis WAAM

In WAAM, contact-type temperature measurement could be challenging and often impractical. The contact-type devices measure the temperature locally; thus, multiple devices at multiple locations are needed to get accurate data throughout the fabrication. For example, attaching/welding a thermocouple during the WAAM of Aluminum alloys is difficult and often prone to error due to high solidification rates. Therefore, the use of non-contact temperature measurement devices is justified. Hence, in this study, an IR Thermal Camera is used for temperature measurements.

Nevertheless, the application of such devices is not straightforward. The accuracy of the measurements depends on the emissivity and reflecting temperature settings of the device. The emissivity changes along with
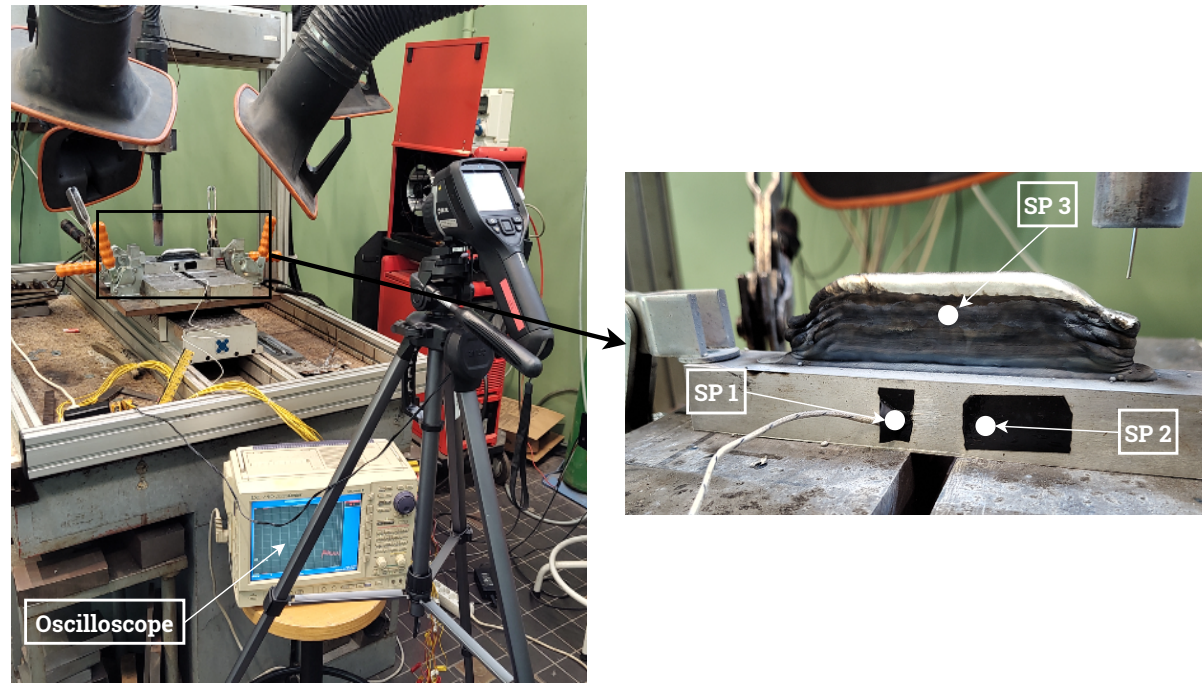
Figure 4.2: Temperature measurement setup for studying the accuracy of the thermal camera
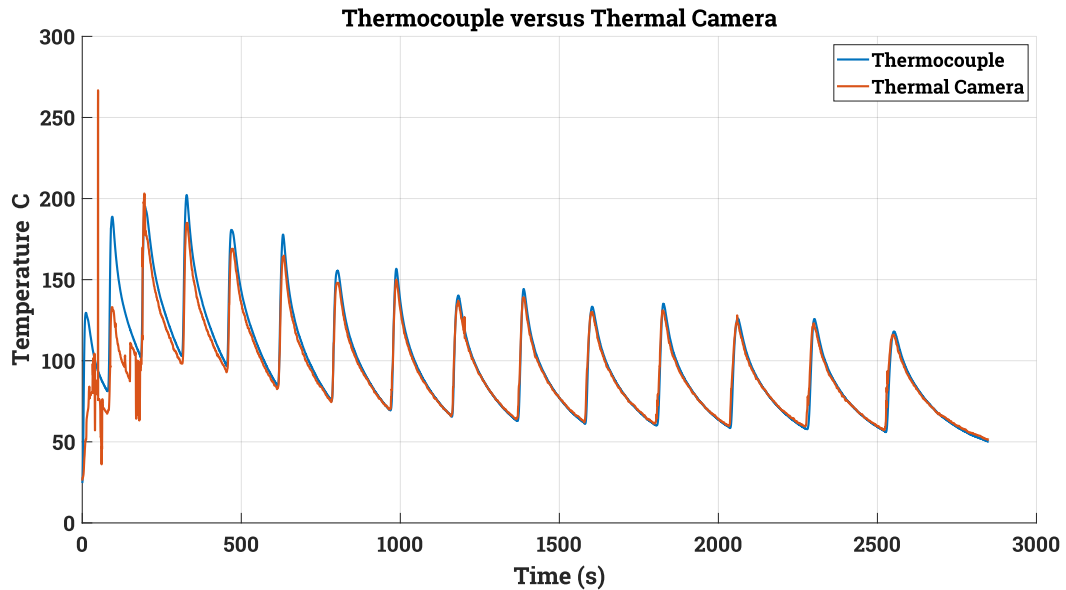
Figure 4.3: Temperature measurement: Comparison between thermocouple and thermal camera

the temperature as well as the surface finish of the measurement object. In WAAM of Aluminum, the freshly deposited layer is shiny and reflective, but the previously deposited layers are not as reflective due to the formation of an oxide layer and soot deposition. The suitable emissivity values for Aluminum WAAM are scarcely available in the literature, hence in this study the soot deposition on the previous layers is taken as a reference object with emissivity 0f 0.9 and 22° C reflecting temperature. Temperature measurements with these settings are validated using a thermocouple and black target of the same emissivity and reflecting temperature. A thermocouple is attached to the substrate and covered with black tape. Another piece of black tape is placed near the thermocouple as shown in Fig.4.2. Three non-contact measurement points are set such that SP1 is located on black tape over the thermocouple, SP2 on the other piece of tape, and SP3 on the black soot region. The thermocouple reading is compared with the SP1 reading, showing good agreement

as depicted in Fig. 4.3. In the beginning, the soot deposition is very low resulting in noisy data in the camera for the first few layers due to exposed shiny aluminum with low emissivity values. The good agreement with the IR measurements and thermocouple measurements indicated the reliability of using an IR thermal camera for fabrication experiments with constant inter-layer temperatures. The inter-layer temperatures are monitored using a thermal camera and once the specific temperature is reached a new subsequent layer is deposited.

Figure 4.4: Wall structure with 2 mm z-axis offset between each layer

Figure 4.5: Wall structure with 2.5 mm z-axis offset between each layer

Wall 7
Inter layer Temperature = 90° C

Wall 8
Inter layer Temperature = 70° C

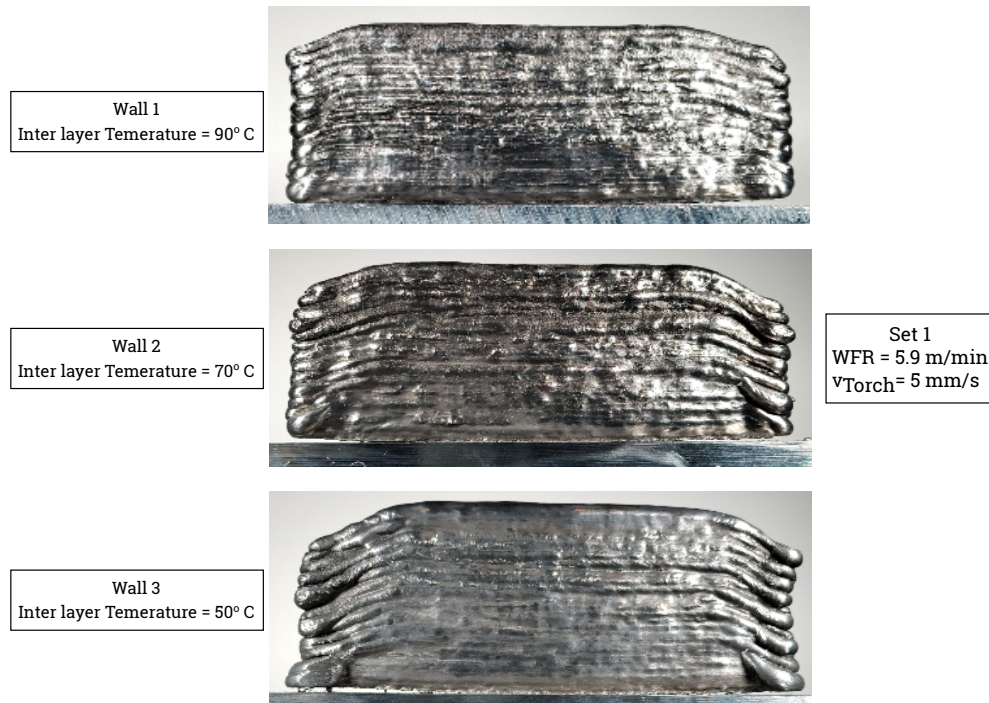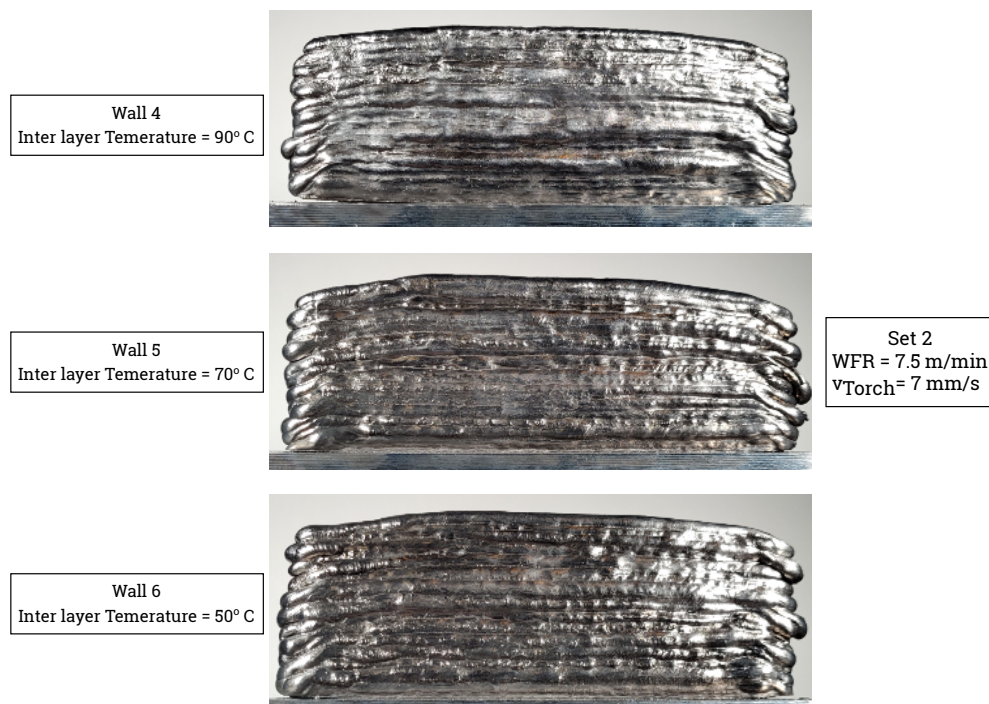Set 3
WFR = 9.3 m/min
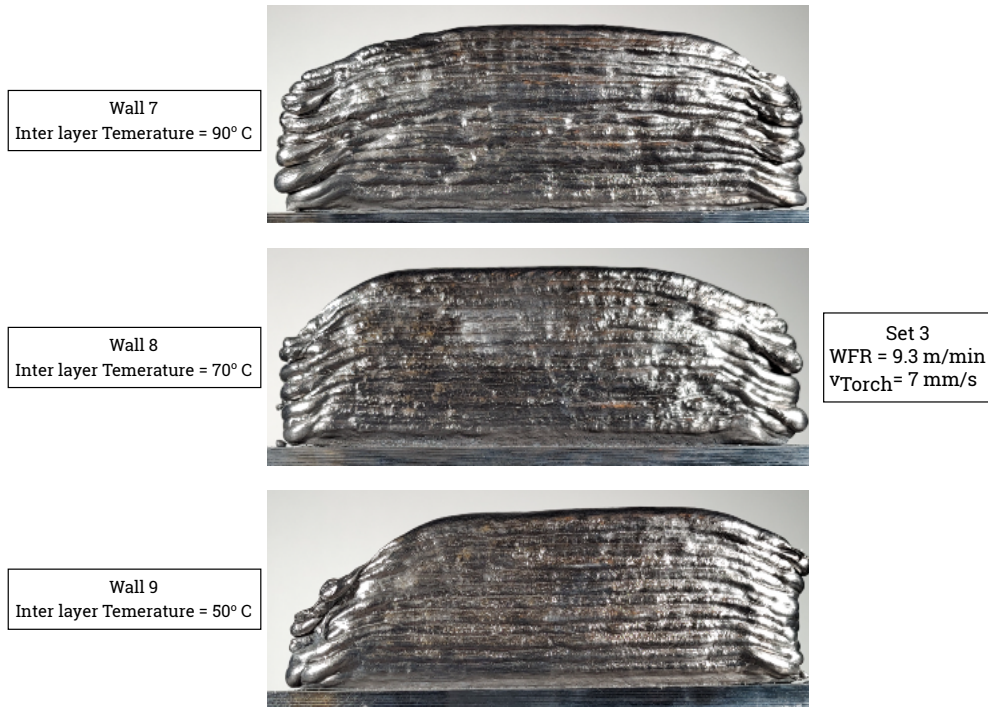v_{Torch}= 7 mm/s

Wall 9
Inter layer Temperature = 50° C

Figure 4.6: Wall structure with 3.5 mm z-axis offset between each layer

The results from the fabrication experiments of 9 single-bead multi-layered wall structures, revealed the effect of the inter-layer temperature on the geometrical formation is not significant, this can be observed in Fig.4.4, 4.5, and 4.6. The z-axis motion after each welding pass had a significant impact on the fabrication process. In set 3 shown in Fig.4.6, where the welding torch was displaced by 3.5mm after each pass, notable dimensional changes were observed. For instance, walls 7, 8, and 9 exhibited lengths of 130mm, 140mm, and 125mm, respectively, despite a torch travel distance of 160mm in the same direction. When the z-axis displacement of the torch was 3.5mm or more, it led to an increased wire stick-out. A greater stick-out at the same voltage reduces the current, consequently lowering the heat input. This substantial reduction in heat input is the primary cause of the significant geometric deviations observed at the weld start-stop regions. The use of an IR thermal camera for inter-layer temperature measurements is feasible for simple geometries like wall structures. Temperature distribution along the build direction depends on the geometry of the component being fabricated [89]. Also for Aluminum alloys, 50° C inter-layer temperature is shown to be suitable for geometric formation as well as microstructure development [90]. Therefore, for further experiments in the study, the inter-layer was maintained at room temperature.

To study the direct application of fabrication sequence optimization 3D shell structures are fabricated with planar and optimized fabrication sequences. Height reductions due to welding start/stop effects are observed in both strategies. In planar fabrication, the tool path advancement after each layer in the overhang region is more pronounced than in non-planar fabrication. This resulted in discontinuous material deposition and a gradual decrease in dimensions in the overhang region of the component. For an optimized fabrication sequence, a smooth and continuous material deposition with less geometric deviation alone with an improved overhang region is observed. The overhang angle is measured using *Fiji-Image J* [85] and illustrated in the Fig.4.7 and 4.8 for planar and optimized fabrication sequences respectively. In the optimized fabrication sequence, the layer thickness is not completely uniform and the optimizer generated a layer distribution containing a transition region where one layer is deposited with non-planar and the next layer with planar material deposition. This transition can lead to uneven material distribution, adversely affecting subsequent layers.
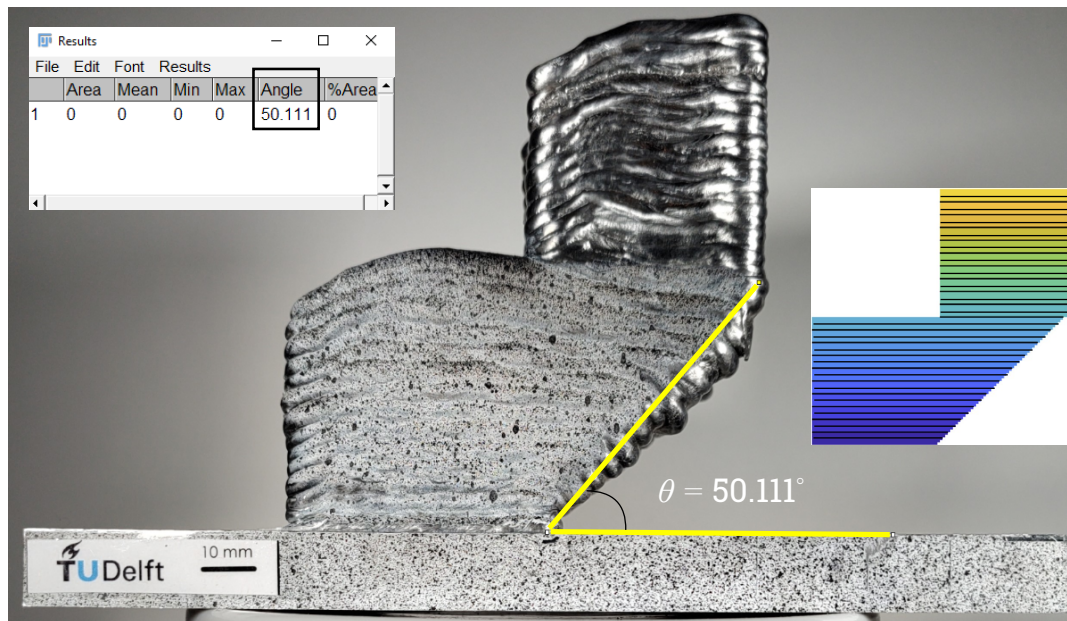
Figure 4.7: Considerable deviation from desired 45° overhang angle with planar fabrication sequence
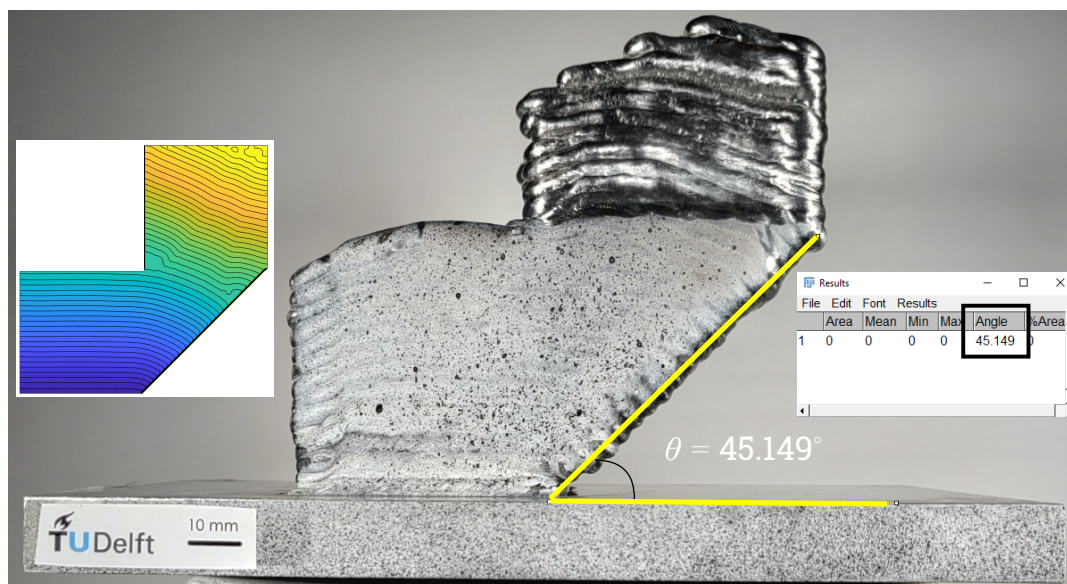
Figure 4.8: Small deviation from desired 45° overhang angle with optimized fabrication sequence

4.3. Distortion Measurements

A 3D optical scanner is utilized to scan the 3D shell structures during and after the fabrication to study the global deviations from the CAD model. The weld parameters used for fabricating structures resulted in bead dimensions around 10 mm. Due to the melting and solidification processes, a straight horizontal bead with a 50 mm torch travel would extend to approximately 60 mm in length, Taking into account the effect of weld start-stop on the final bead dimensions, a CAD model was created in SOLIDWORKS. The CAD model and scanned models are overlapped with one face and three points coinciding to analyze the deviations that arose due to WAAM. The overlap clearly indicates the deviations in the fabricated structures. Planar fabrication resulted in an uncontrolled material deposition in the overhang region that led to a significant deviation from the intended 45° overhang. The top structure is based on the development of the overhang region, the dimensions of the side wall are around 10 mm off from the CAD as shown in the top row of Fig.4.9. Optimized fabrication showed less deviation from the CAD model and can be seen in the bottom row of Fig.4.9. The

overhang angle of 45.149° indicates better material deposition. An excess material accumulation can be observed in the transition region, it is due to the varying stick-out length during fabrication that changed the process parameter resulting in uncontrolled material deposition.
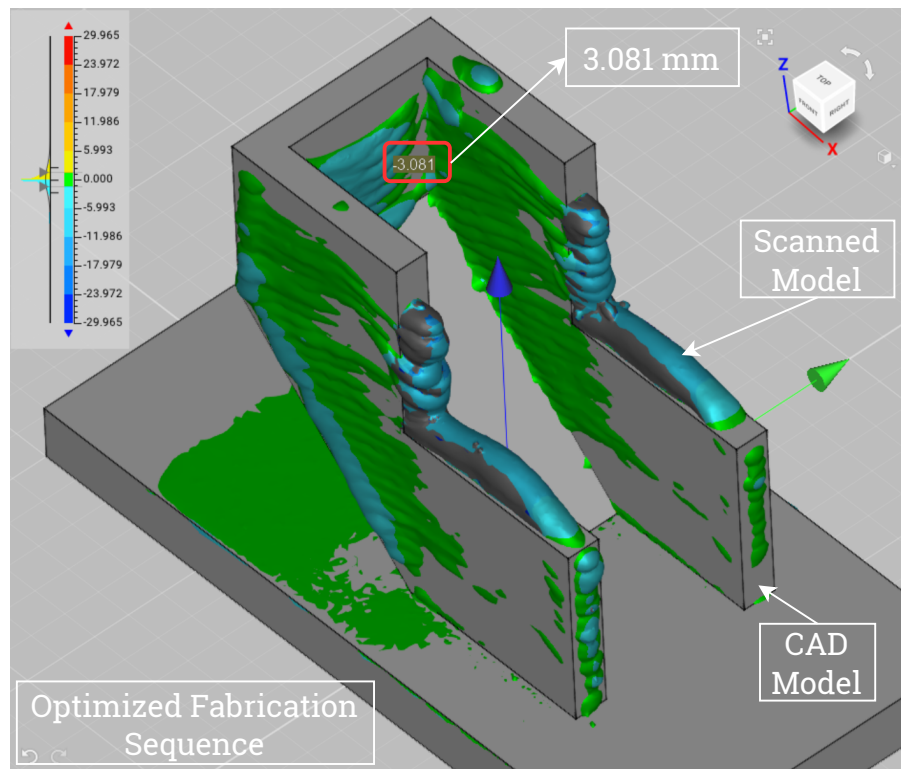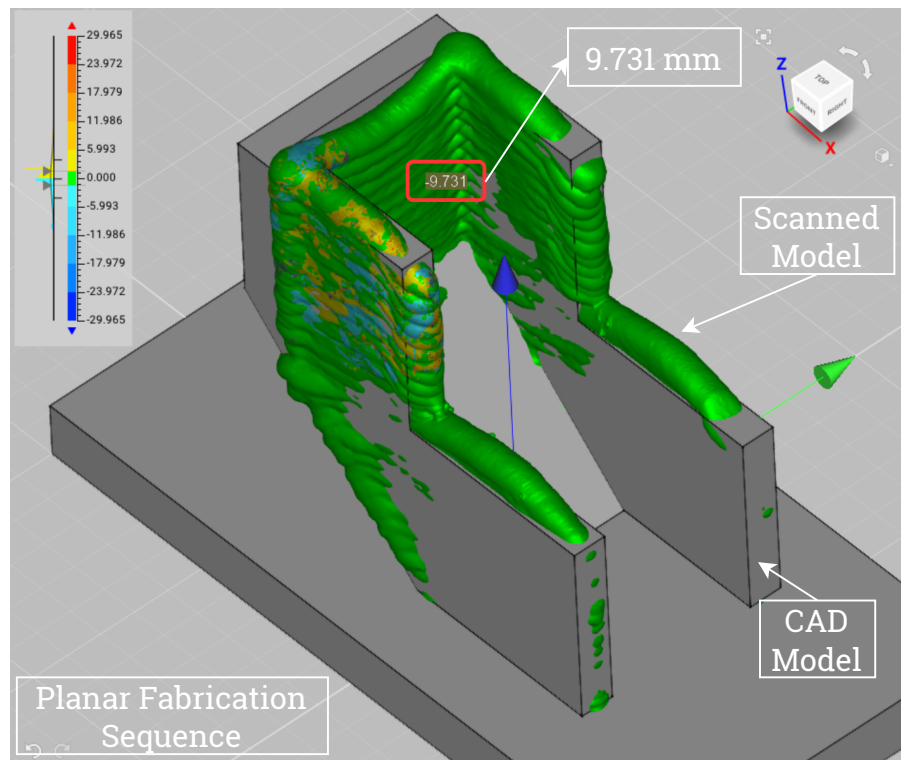
Figure 4.9: Distance mapping between CAD and scanned model. Top row: Planar fabrication, Bottom row: Optimized fabrication

In this research, planar and optimized fabrication sequence are characterized by planar and non-planar material deposition, thus with same welding parameters along with fabrication parameters, it is interesting to study the strain development for each fabrication sequence. A DIC method is used for in-situ strain measurement in the substrate as well as partially deposited structure during the deposition of the last 5 layers. In the post-processing, four line gauges are positioned within the DIC frames, and the strain in these gauges are determined using the image correlation method. Gauge S1 is placed on the substrate and P1, P2, and P3 are on the partly deposited structure with initial lengths of 95, 40, 45, and 75 respectively. For each gauge, the length with respect to the reference frame is calculated for all frames then those values are used to evaluate the change in length for all frames. Based on the change in length and initial length, gauge strain is calculated for each frame. The strain gauge for S1, P1, P2, and P3 are plotted in Fig.4.11, 4.12, 4.13, and 4.14 respectively. For all the virtual line gauges the strain value is higher for planar fabrication compared to optimized fabrication. Also, The magnitude of strain is higher for gauge P3 compared to S1, this is due to high thermal strain resulting from heat accumulation.

4
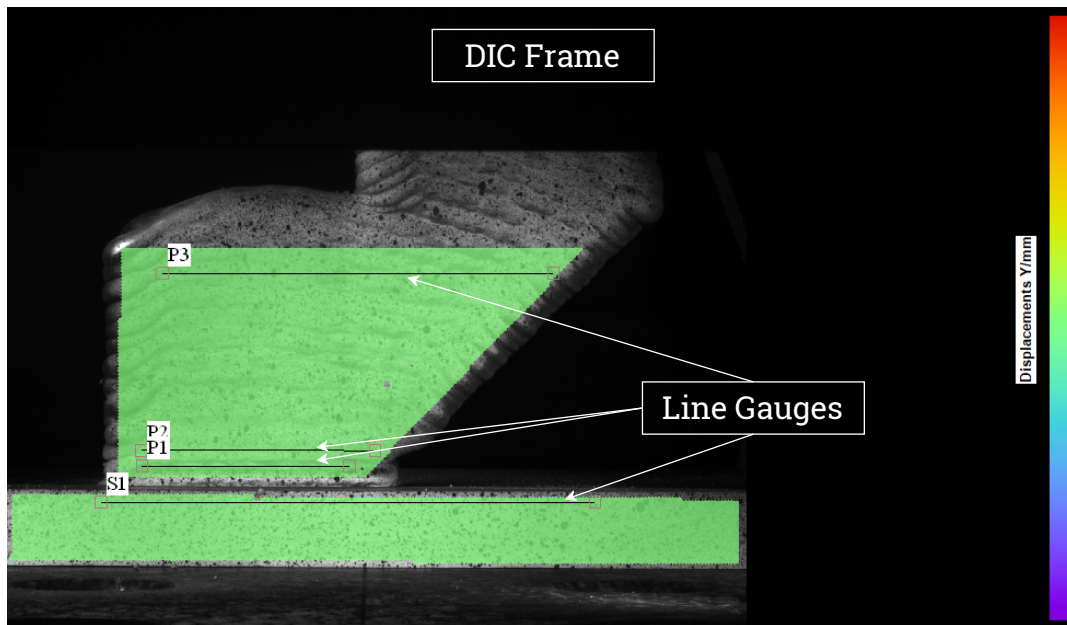
Figure 4.10: DIC screen with four line gauges S1(on substrate), P1, P2, and P3 on the previously deposited region
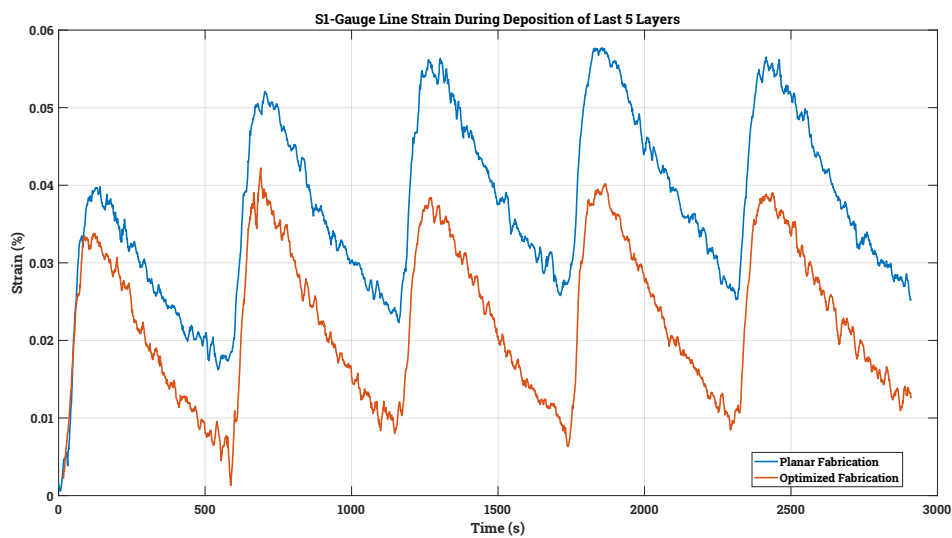
Figure 4.11: Line strain in gauge S1 placed on the substrate
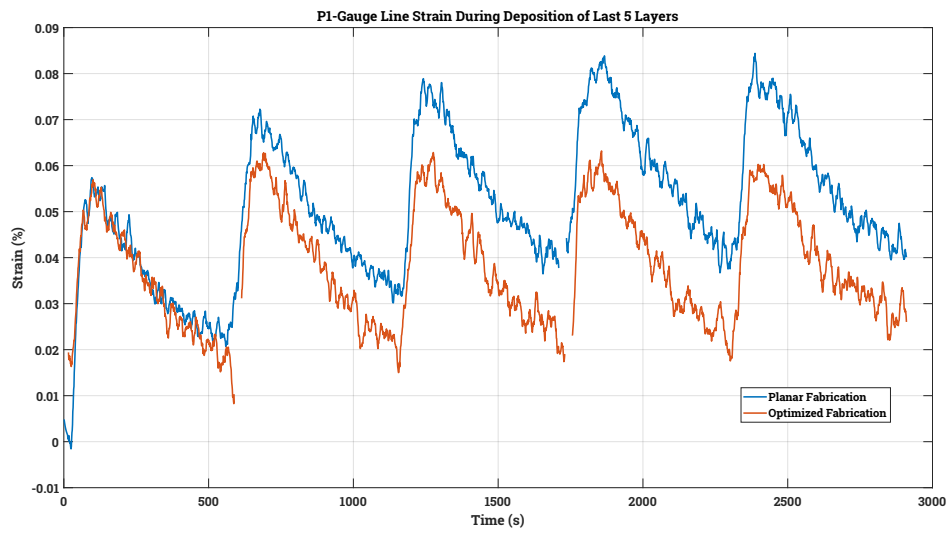
Figure 4.12: Line strain in gauge P1 placed on the partially deposited structure
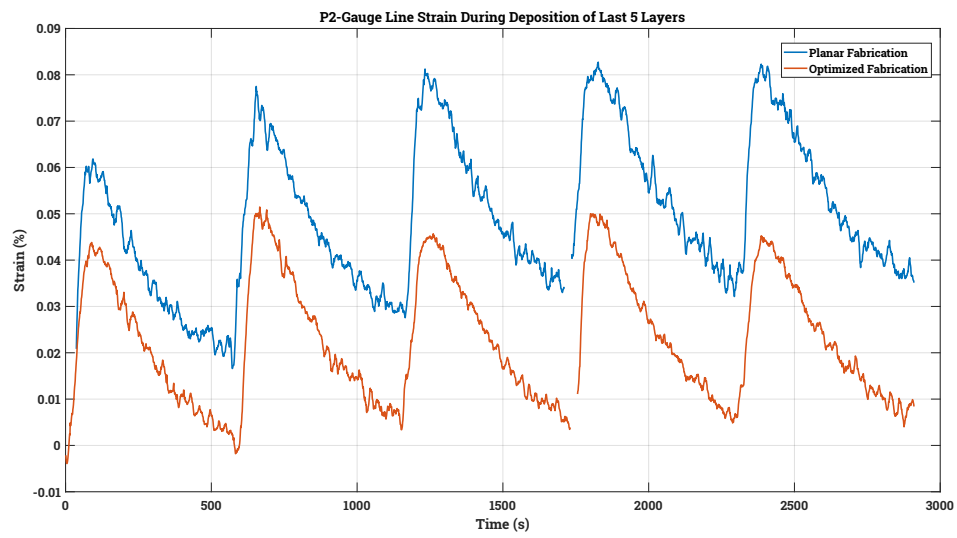
Figure 4.13: Line strain in gauge P2 placed on the partially deposited structure
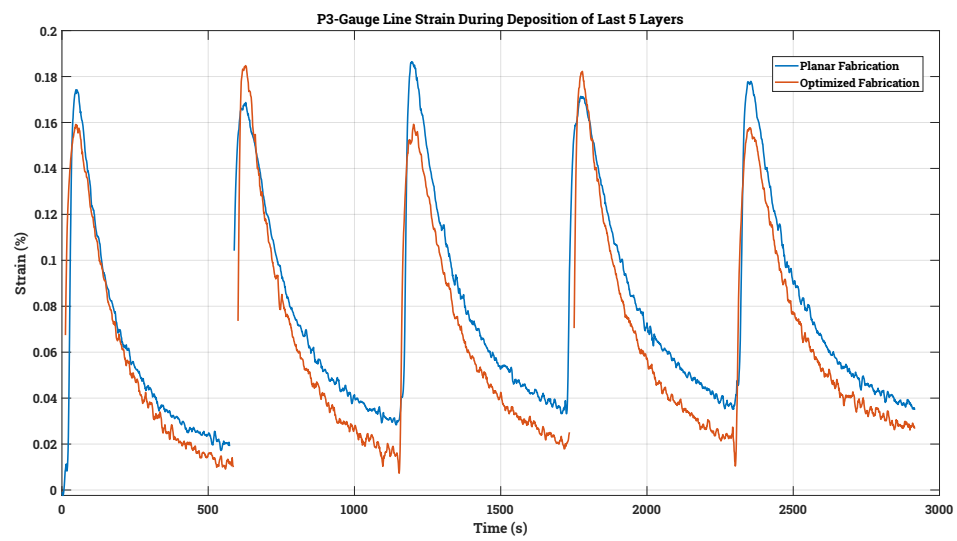
Figure 4.14: Line strain in gauge P3 placed on the partially deposited structure

3D scanning and DIC indicated less distortion and strain development with part fabricated using an optimized fabrication sequence. While physical contact-based distortion measurements of deposited structures are challenging, using such measurements for in-situ/ex-situ substrate distortion is feasible. In this study, the deflection of the substrate after fabrication is measured using a vernier height gauge as shown in Fig.4.15. The substrates are machined to 15 mm thickness before WAAM. During the measurement, the cool downed part is kept on a flat marble table (fig.4.15(a)), such that the substrate is clamped to the table from one side. The deflection on the opposite side due to WAAM is then measured using the height gauge. First, the measuring jaw is lowered completely to touch the marble plate marking a zero reading on the vernier scale as shown in Fig.4.15(b). The deflection is measured by placing the measuring jaw in three different locations as shown in Fig.4.15(c). The measurement results are tabulated in Table 4.2 indicating relatively low distortion in optimized fabrication.

(a)

(b)   (c)
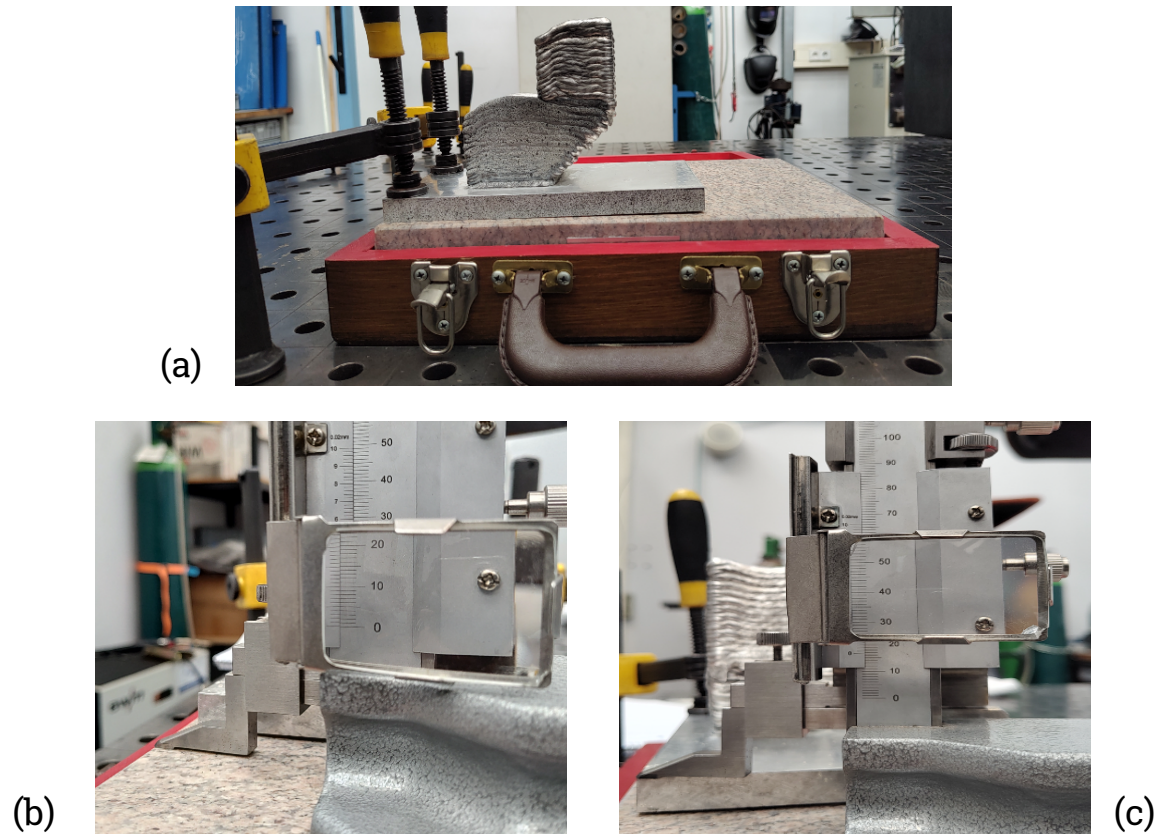
Figure 4.15: Substrate deflection. (a) Fabricated part clamped on one side, (b) Zero reading of height gauge when in contact with the marble top, and (c) Height gauge reading along the deflected edge of the substrate

	Distance (mm)	Average Distance (mm)	Δ
Planar Deposition	16.90 16.88 17.02	16.93	1.93
Optimized Deposition	16.70 16.66 16.72	16.69	1.69

Table 4.2: Deflection of the substrate for two types of fabrication sequences

5

CONCLUSION AND RECOMMENDATIONS

5.1. CONCLUSIONS

The primary objective of this research, as outlined in Chapter 1, was to fabricate metal structures using multi-axis Wire Arc Additive Manufacturing (WAAM) with an optimized fabrication sequence and to measure distortion to validate the sequence optimization for distortion minimization. Accordingly, a series of fabrication experiments were performed to investigate the challenges associated with producing parts using an optimized sequence, as well as to explore various in situ measurement techniques useful for the validation and calibration of fabrication sequence optimization. Addressing the main objective and sub-objectives, the following conclusions were drawn during the course of WAAM experiments.

- Emphasizing the significance of material choice, the study particularly underscores how specific materials, such as aluminum alloys and those with high coefficients of thermal expansion (CTE), stand to gain from optimized fabrication sequences. The optimized sequence enhances geometric accuracy, particularly beneficial for intricate overhang features. By leveraging 3D scanning and Digital Image Correlation (DIC) for strain measurement, the investigation illustrates low strain development during optimized material deposition. Distortion analyses further affirm the superiority of optimized fabrication over conventional planar methods, thereby lending qualitative validation to simulation projections and accentuating the pivotal role of optimized material deposition for chosen materials as well as other common materials processed in WAAM.

- The experiments highlighted the considerable influence of wire feed rate (and its associated welding current/voltage) and torch travel speed on the quality of individual weld beads in WAAM. As multiple beads overlap to create layers, the overall deposition quality of the final structure is shaped by both weld process parameters and the fabrication sequence. The λ parameter, which correlates with wire feed rate and torch speed, demonstrates the ability to forecast bead dimensions for particular materials, exemplified in this study with aluminum 5xxx series alloys. This correlation can serve as a dimensional restriction within the optimization algorithm to regulate layer size during fabrication.

- The impact of inter-layer temperature on the comprehensive build-up process during WAAM, particularly concerning aluminum alloys, exhibits minimal effects when maintained below the threshold of 120°C. Conversely, for alternative materials, keeping inter-layer temperatures at ambient levels may precipitate the occurrence of welding defects. Consequently, in the optimization process, strain calculations should meticulously incorporate the temperature gradient spanning from the solidus to inter-layer temperatures. Currently, the prevailing optimization strategy overlooks the accumulation of material and geometric irregularities at weld start/stops, which have the potential to modify crucial weld process parameters and ultimately distort the final product. To counteract this issue, incorporating strain calculations that accurately reflect the elevated heat input characteristic of the initial stages of the weld bead will improve optimization results.

In conclusion, an optimized fabrication sequence that takes into account welding aspects, predicted bead dimensions and variable heat inputs can yield a deposited structure closely matching the desired geome-

try. This would further validate the experimental findings and improve the accuracy and quality of WAAM-fabricated structures, broadening the range of applications and materials suitable for this advanced manufacturing technology.

5.2. RECOMMENDATIONS

The current research presents a way to bridge the gap between the effectiveness of fabrication sequence optimization in minimizing varieties of distortion measures in the simulation and reality. The computational framework of fabrication sequence optimization [22] along with the introduction of layer thickness uniformity [23] provides a state-of-the-art design tool for multi-axis AM, including WAAM. The numerical results show a promising potential by reducing the distortion by up to 2 orders of magnitude, however, the algorithm does not take into account special characteristics of WAAM, including change in heat input along the weld bead due to weld start and stop points. Also, the majority of WAAM setups demand constant welding parameters within a layer, this limits the possibility of following the material distribution given by the optimization algorithm exactly. The observed effects of welding parameters on the bead dimensions and in turn layer dimensions can be integrated into the optimization algorithm facilitating closeness between optimization results and actual fabricated parts. This will lead to a one step closer to the full experimental validation in future studies.

To improve future research, the following recommendations for the fabrication and measurement processes are suggested:

- An extension to the current research, it is interesting to use different materials, such as high-melting temperature materials to evaluate the impacts of optimized fabrication sequences on both manufacturing processes and distortion phenomena.

- For the temperature measurements, the soot formation during the welding is considered as a matt black object with high emissivity (0.9 in this case). This strategy is proven effective for WAAM using aluminum alloys. In the future for other materials and or complex structures, this method can be used to generate a temperature profile that can be utilized to calculate cooling rates for progressive layers. Estimated rates can give the desired dwell times specific to the printed geometry. An automated feedback system could also be designed that will trigger the material deposition based on the temperature profile.

- IR thermal camera can also utilized for distortion measurements. Thermal profiles generated by the camera can be compared to measure the geometric deviations. This method would be suitable for simple test geometries used in future validation studies.

- Incorporating in-situ strain measurement proves invaluable for fine-tuning the optimization algorithm. Although this study focused on conducting 2D strain field measurements, the inherent arc shape and surface irregularities of the weld bead suggest the necessity for a more comprehensive approach. Thus, future research endeavors are encouraged to employ advanced multi-camera 3D DIC systems for attaining a detailed 3D strain field measurement. A two-series strain measurement process can be designed such that, in the first measurement set, a global strain evaluation is measured for the fabrication of different segments of the geometry. A localized strain behavior is measured in the second measurement set, with a sampling frequency close to the strain rate evaluated in the first measurement set. The second set measurement duration will be very small, as the sampling frequency corresponding to the strain rate will require a very high frame rate in DIC. The average strain values from the second measurement can be used in the optimization algorithm.

- During DIC, a significant challenge was applying the speckle pattern. While literature explores using surface irregularities in deposited structures as speckle patterns, surface reflections can severely hinder this approach. In the traditional DIC methods, a novel strategy of using a fluorescent background [91] for speckle pattern shows improved results for tackling the reflection errors. From the WAAM perspective, using fluorescent colors instead of a full speckle pattern can reduce reflection errors. This enables the use of surface irregularities for strain measurement rather than as a speckle pattern.

BIBLIOGRAPHY

[1] I. O. for Standardization (2021), "Iso/astm 52900:2021, additive manufacturing — general principles — fundamentals and vocabulary," Geneva, CH, Tech. Rep.

[2] I. Gibson, D. W. Rosen, B. Stucker, *et al.*, *Additive manufacturing technologies*. Springer, 2021, vol. 17.

[3] H. Bikas, P. Stavropoulos, and G. Chryssolouris, "Additive manufacturing methods and modelling approaches: A critical review," *The International Journal of Advanced Manufacturing Technology*, vol. 83, pp. 389–405, 2016.

[4] N. N. Kumbhar and A. Mulay, "Post processing methods used to improve surface finish of products which are manufactured by additive manufacturing technologies: A review," *Journal of The Institution of Engineers (India): Series C*, vol. 99, pp. 481–487, 2018.

[5] J. Jiang, S. T. Newman, and R. Y. Zhong, "A review of multiple degrees of freedom for additive manufacturing machines," *International Journal of Computer Integrated Manufacturing*, vol. 34, no. 2, pp. 195–211, 2021.

[6] W. E. Frazier, "Metal additive manufacturing: A review," *Journal of Materials Engineering and performance*, vol. 23, pp. 1917–1928, 2014.

[7] J. O. Milewski, G. K. Lewis, D. Thoma, G. Keel, R. B. Nemec, and R. Reinert, "Directed light fabrication of a solid metal hemisphere using 5-axis powder deposition," *Journal of Materials Processing Technology*, vol. 75, no. 1-3, pp. 165–172, 1998.

[8] L. Gardner, P. Kyvelou, G. Herbert, and C. Buchanan, "Testing and initial verification of the world's first metal 3d printed bridge," *Journal of constructional steel research*, vol. 172, p. 106 233, 2020.

[9] *Bmw group with "live wire" to innovative production of vehicle components in waam process*, https://www.press.bmwgroup.com/global/article/detail/T0440485EN.

[10] S. W. Williams, F. Martina, A. C. Addison, J. Ding, G. Pardal, and P. Colegrove, "Wire+ arc additive manufacturing," *Materials science and technology*, vol. 32, no. 7, pp. 641–647, 2016.

[11] Y. Ding, R. Dwivedi, and R. Kovacevic, "Process planning for 8-axis robotized laser-based direct metal deposition system: A case on building revolved part," *Robotics and Computer-Integrated Manufacturing*, vol. 44, pp. 67–76, 2017.

[12] W. Ya and K. Hamilton, "On-demand spare parts for the marine industry with directed energy deposition: Propeller use case," in *Industrializing Additive Manufacturing-Proceedings of Additive Manufacturing in Products and Applications-AMPA2017 1*, Springer, 2018, pp. 70–81.

[13] D. Chakraborty, T. Tirumala, S. Chitral, B. Sahoo, D. Kiran, and P. A. Kumar, "The state of the art for wire arc additive manufacturing process of titanium alloys for aerospace applications," *Journal of Materials Engineering and Performance*, vol. 31, no. 8, pp. 6149–6182, 2022.

[14] A. Josten and M. Höfemann, "Arc-welding based additive manufacturing for body reinforcement in automotive engineering," *Welding in the World*, vol. 64, no. 8, pp. 1449–1458, 2020.

[15] F. Xu, V. Dhokia, P. Colegrove, *et al.*, "Realisation of a multi-sensor framework for process monitoring of the wire arc additive manufacturing in producing ti-6al-4v parts," *International Journal of Computer Integrated Manufacturing*, vol. 31, no. 8, pp. 785–798, 2018.

[16] D. Jafari, T. H. Vaneker, and I. Gibson, "Wire and arc additive manufacturing: Opportunities and challenges to control the quality and accuracy of manufactured parts," *Materials & Design*, vol. 202, p. 109 471, 2021.

[17] L. Nguyen, J. Buhl, R. Israr, and M. Bambach, "Analysis and compensation of shrinkage and distortion in wire-arc additive manufacturing of thin-walled curved hollow sections," *Additive Manufacturing*, vol. 47, p. 102 365, 2021.

[18] B. Wu, Z. Pan, G. Chen, *et al.*, "Mitigation of thermal distortion in wire arc additively manufactured ti6al4v part using active interpass cooling," *Science and Technology of Welding and Joining*, vol. 24, no. 5, pp. 484–494, 2019.

[19] A. Diourté, F. Bugarin, C. Bordreuil, and S. Segonds, "Continuous three-dimensional path planning (ctpp) for complex thin parts with wire arc additive manufacturing," *Additive Manufacturing*, vol. 37, p. 101 622, 2021.

[20] M. Ni, Y. Zhou, Z. Hu, X. Qin, X. Xiong, and F. Ji, "Forming optimization for waam with weaving deposition on curved surfaces," *International Journal of Mechanical Sciences*, vol. 252, p. 108 366, 2023.

[21] F. Michel, H. Lockett, J. Ding, F. Martina, G. Marinelli, and S. Williams, "A modular path planning solution for wire+ arc additive manufacturing," *Robotics and Computer-Integrated Manufacturing*, vol. 60, pp. 1–11, 2019.

[22] W. Wang, F. van Keulen, and J. Wu, "Fabrication sequence optimization for minimizing distortion in multi-axis additive manufacturing," *Computer Methods in Applied Mechanics and Engineering*, vol. 406, p. 115 899, 2023.

[23] M. Lansu, *Layer thickness control: Improving manufacturability in fabrication sequence optimization for multi-axis additive manufacturing*, Master Thesis, 2023. [Online]. Available: http://resolver.tudelft.nl/uuid:641fe20b-05dd-4cf6-a0e5-096576e14ac4.

[24] V. Mishra, A. Babu, R. Schreurs, K. Wu, M. Hermans, and C. Ayas, "Microstructure estimation and validation of er110s-g steel structures produced by wire and arc additive manufacturing," *journal of materials research and technology*, vol. 23, pp. 3579–3601, 2023.

[25] Z. Pan, D. Ding, B. Wu, D. Cuiuri, H. Li, and J. Norrish, "Arc welding processes for additive manufacturing: A review," *Transactions on Intelligent Welding Manufacturing: Volume I No. 1 2017*, pp. 3–24, 2018.

[26] T. Artaza, A. Alberdi, M. Murua, *et al.*, "Design and integration of waam technology and in situ monitoring system in a gantry machine," *Procedia Manufacturing*, vol. 13, pp. 778–785, 2017.

[27] P. Almeida and S. Williams, "Innovative process model of ti-6al-4v additive layer manufacturing using cold metal transfer (cmt)," 2010.

[28] H. Lockett, J. Ding, S. Williams, and F. Martina, "Design for wire+ arc additive manufacture: Design rules and build orientation selection," *Journal of Engineering Design*, vol. 28, no. 7-9, pp. 568–598, 2017.

[29] J. Spencer, P. Dickens, and C. Wykes, "Rapid prototyping of metal parts by three-dimensional welding," *Proceedings of the Institution of Mechanical Engineers, Part B: Journal of Engineering Manufacture*, vol. 212, no. 3, pp. 175–182, 1998.

[30] T. A. Rodrigues, V. Duarte, J. A. Avila, T. G. Santos, R. Miranda, and J. Oliveira, "Wire and arc additive manufacturing of hsla steel: Effect of thermal cycles on microstructure and mechanical properties," *Additive Manufacturing*, vol. 27, pp. 440–450, 2019.

[31] X. Zhang, Q. Zhou, K. Wang, *et al.*, "Study on microstructure and tensile properties of high nitrogen cr-mn steel processed by cmt wire and arc additive manufacturing," *Materials & Design*, vol. 166, p. 107 611, 2019.

[32] K. Karunakaran, S. Suryakumar, V. Pushpa, and S. Akula, "Low cost integration of additive and subtractive processes for hybrid layered manufacturing," *Robotics and Computer-Integrated Manufacturing*, vol. 26, no. 5, pp. 490–499, 2010.

[33] L. Yuan, Z. Pan, D. Ding, *et al.*, "Investigation of humping phenomenon for the multi-directional robotic wire and arc additive manufacturing," *Robotics and Computer-Integrated Manufacturing*, vol. 63, p. 101 916, 2020.

[34] J. S. Panchagnula and S. Simhambhatla, "Inclined slicing and weld-deposition for additive manufacturing of metallic objects with large overhangs using higher order kinematics," *Virtual and Physical Prototyping*, vol. 11, no. 2, pp. 99–108, 2016.

[35] J. Xiong, G. Zhang, and W. Zhang, "Forming appearance analysis in multi-layer single-pass gmaw-based additive manufacturing," *The International Journal of Advanced Manufacturing Technology*, vol. 80, pp. 1767–1776, 2015.

5

[36] *Norsk titanium*, https://www.norsktitanium.com/media.

[37] Z. Lin, K. Song, and X. Yu, "A review on wire and arc additive manufacturing of titanium alloy," *Journal of Manufacturing Processes*, vol. 70, pp. 24–45, 2021.

[38] B. E. Carroll, T. A. Palmer, and A. M. Beese, "Anisotropic tensile behavior of ti–6al–4v components fabricated with directed energy deposition additive manufacturing," *Acta Materialia*, vol. 87, pp. 309–320, 2015.

[39] H. Attar, M. Bermingham, S. Ehtemam-Haghighi, A. Dehghan-Manshadi, D. Kent, and M. Dargusch, "Evaluation of the mechanical and wear properties of titanium produced by three different additive manufacturing methods for biomedical application," *Materials Science and Engineering: A*, vol. 760, pp. 339–345, 2019.

[40] W. Yangfan, C. Xizhang, and S. Chuanchu, "Microstructure and mechanical properties of inconel 625 fabricated by wire-arc additive manufacturing," *Surface and Coatings Technology*, vol. 374, pp. 116–123, 2019.

[41] Z. Zeng, B. Cong, J. Oliveira, *et al.*, "Wire and arc additive manufacturing of a ni-rich niti shape memory alloy: Microstructure and mechanical properties," *Additive manufacturing*, vol. 32, p. 101 051, 2020.

[42] G. Mathers, *The welding of aluminium and its alloys*. Elsevier, 2002.

[43] R. Nunes, K. Faes, W. De Waele, *et al.*, "A review on the weldability of additively manufactured aluminium parts by fusion and solid-state welding processes," *Metals*, vol. 13, no. 10, p. 1724, 2023.

[44] B. Cong, Z. Qi, B. Qi, H. Sun, G. Zhao, and J. Ding, "A comparative study of additively manufactured thin wall and block structure with al-6.3% cu alloy using cold metal transfer process," *Applied Sciences*, vol. 7, no. 3, p. 275, 2017.

[45] C. Su, X. Chen, S. Konovalov, R. Arvind Singh, S. Jayalakshmi, and L. Huang, "Effect of deposition strategies on the microstructure and tensile properties of wire arc additive manufactured al-5si alloys," *Journal of Materials Engineering and Performance*, vol. 30, pp. 2136–2146, 2021.

[46] A. Horgar, H. Fostervoll, B. Nyhus, X. Ren, M. Eriksson, and O. Akselsen, "Additive manufacturing using waam with aa5183 wire," *Journal of Materials Processing Technology*, vol. 259, pp. 68–74, 2018.

[47] M. Dinovitzer, X. Chen, J. Laliberte, X. Huang, and H. Frei, "Effect of wire and arc additive manufacturing (waam) process parameters on bead geometry and microstructure," *Additive Manufacturing*, vol. 26, pp. 138–146, 2019.

[48] A. Adebayo, J. Mehnen, and X. Tonnellier, "Limiting travel speed in additive layer manufacturing," 2012.

[49] M. Tawfik, M. Nemat-Alla, and M. Dewidar, "Effect of travel speed on the properties of al-mg aluminum alloy fabricated by wire arc additive manufacturing," *Journal of Materials Engineering and Performance*, vol. 30, no. 10, pp. 7762–7769, 2021.

[50] Y. Zhou, X. Lin, N. Kang, W. Huang, J. Wang, and Z. Wang, "Influence of travel speed on microstructure and mechanical properties of wire+ arc additively manufactured 2219 aluminum alloy," *Journal of Materials Science & Technology*, vol. 37, pp. 143–153, 2020.

[51] H. Wang, W. Jiang, J. Ouyang, and R. Kovacevic, "Rapid prototyping of 4043 al-alloy parts by vp-gtaw," *Journal of Materials Processing Technology*, vol. 148, no. 1, pp. 93–102, 2004.

[52] P. Kazanas, P. Deherkar, P. Almeida, H. Lockett, and S. Williams, "Fabrication of geometrical features using wire and arc additive manufacture," *Proceedings of the Institution of Mechanical Engineers, Part B: Journal of Engineering Manufacture*, vol. 226, no. 6, pp. 1042–1051, 2012.

[53] L. Terrenoir, J. Lartigau, A. Arjunan, L. Laguna Salvado, and C. Merlo, "Influence of wire feed speed and torch speed on the mechanical properties of wire arc additively manufactured stainless steel," *Journal of Manufacturing Science and Engineering*, vol. 145, no. 10, p. 101 012, 2023.

[54] C. Wang, W. Suder, J. Ding, and S. Williams, "The effect of wire size on high deposition rate wire and plasma arc additive manufacture of ti-6al-4v," *Journal of Materials Processing Technology*, vol. 288, p. 116 842, 2021.

[55] P. Jiang, X. Li, X. Zong, *et al.*, "Multi-wire arc additive manufacturing of ti basic heterogeneous alloy: Effect of deposition current on the microstructure, mechanical property and corrosion-resistance," *Journal of Alloys and Compounds*, vol. 920, p. 166 056, 2022.

[56] M. C. F. Eriksson, M. Lervåg, C. Sørensen, *et al.*, "Additive manufacture of superduplex stainless steel using waam," 2018.

[57] K. S. Derekar, B. Ahmad, X. Zhang, *et al.*, "Effects of process variants on residual stresses in wire arc additive manufacturing of aluminum alloy 5183," *Journal of Manufacturing Science and Engineering*, vol. 144, no. 7, p. 071 005, 2022.

[58] J. Xiong, G. Liu, and G. Zhang, "Influence of interlayer temperature on microstructure and mechanical properties of tial alloys in wire and arc additive manufacturing," *Journal of Manufacturing Processes*, vol. 94, pp. 278–288, 2023.

[59] S. Singh, I. Palani, S. Dehgahi, C. Paul, K. Prashanth, and A. Qureshi, "Influence of the interlayer temperature on structure and properties of cmt wire arc additive manufactured niti structures," *Journal of Alloys and Compounds*, vol. 966, p. 171 447, 2023.

[60] Y. M. Zhang, P. Li, Y. Chen, and A. T. Male, "Automated system for welding-based rapid prototyping," *Mechatronics*, vol. 12, no. 1, pp. 37–53, 2002.

[61] Z. Hu, X. Qin, T. Shao, and H. Liu, "Understanding and overcoming of abnormity at start and end of the weld bead in additive manufacturing with gmaw," *The International Journal of Advanced Manufacturing Technology*, vol. 95, pp. 2357–2368, 2018.

[62] D. Ding, Z. Pan, D. Cuiuri, and H. Li, "A practical path planning methodology for wire and arc additive manufacturing of thin-walled structures," *Robotics and Computer-Integrated Manufacturing*, vol. 34, pp. 8–19, 2015.

[63] G. Venturini, F. Montevecchi, A. Scippa, and G. Campatelli, "Optimization of waam deposition patterns for t-crossing features," *Procedia Cirp*, vol. 55, pp. 95–100, 2016.

[64] L. Nguyen, J. Buhl, and M. Bambach, "Decomposition algorithm for tool path planning for wire-arc additive manufacturing," *Journal of Machine Engineering*, vol. 18, no. 1, pp. 95–106, 2018.

[65] B. Bankong, T. Abioye, T. Olugbade, H. Zuhailawati, O. Gbadeyan, and T. Ogedengbe, "Review of post-processing methods for high-quality wire arc additive manufacturing," *Materials Science and Technology*, vol. 39, no. 2, pp. 129–146, 2023.

[66] D. Radaj, *Heat effects of welding: temperature field, residual stress, distortion*. Springer Science & Business Media, 2012.

[67] M. Yuan and Y. Ueda, "Prediction of residual stresses in welded t-and i-joints using inherent strains," 1996.

[68] J. Mehnen, J. Ding, H. Lockett, and P. Kazanas, "Design study for wire and arc additive manufacture," *International Journal of Product Development 20*, vol. 19, no. 1-3, pp. 2–20, 2014.

[69] X. Li, J. Lin, Z. Xia, Y. Zhang, and H. Fu, "Influence of deposition patterns on distortion of h13 steel by wire-arc additive manufacturing," *Metals*, vol. 11, no. 3, p. 485, 2021.

[70] J. Hönnige, P. A. Colegrove, S. Ganguly, E. Eimer, S. Kabra, and S. Williams, "Control of residual stress and distortion in aluminium wire+ arc additive manufacture with rolling," *Additive Manufacturing*, vol. 22, pp. 775–783, 2018.

[71] J. Heigel, P. Michaleris, and E. W. Reutzel, "Thermo-mechanical model development and validation of directed energy deposition additive manufacturing of ti–6al–4v," *Additive manufacturing*, vol. 5, pp. 9–19, 2015.

[72] A. Dunbar, E. Denlinger, J. Heigel, *et al.*, "Development of experimental method for in situ distortion and temperature measurements during the laser powder bed fusion additive manufacturing process," *Additive Manufacturing*, vol. 12, pp. 25–30, 2016.

[73] N. Klingbeil, J. Zinn, and J. Beuth, "Measurement of residual stresses in parts created by shape deposition manufacturing," in *1997 International Solid Freeform Fabrication Symposium*, 1997.

[74] *Artec space spider*, https://www.artec3d.com/portable-3d-scanners/artec-spider.

[75] F. G. Cunha, T. G. Santos, and J. Xavier, "In situ monitoring of additive manufacturing using digital image correlation: A review," *Materials*, vol. 14, no. 6, p. 1511, 2021.

5

[76] Q. Wang, J. Jia, Y. Zhao, and A. Wu, "In situ measurement of full-field deformation for arc-based directed energy deposition via digital image correlation technology," *Additive Manufacturing*, vol. 72, p. 103 635, 2023.

[77] E. R. Denlinger, J. Irwin, and P. Michaleris, "Thermomechanical modeling of additive manufacturing large parts," *Journal of Manufacturing Science and Engineering*, vol. 136, no. 6, p. 061 007, 2014.

[78] X. Liang, L. Cheng, Q. Chen, Q. Yang, and A. C. To, "A modified method for estimating inherent strains from detailed process simulation for fast residual distortion prediction of single-walled structures fabricated by directed energy deposition," *Additive Manufacturing*, vol. 23, pp. 471–486, 2018.

[79] X. Meng, A. Pullen, X. Guo, X. Yun, and L. Gardner, "Applications of 3d scanning and digital image correlation in structural experiments," *ce/papers*, vol. 6, no. 3-4, pp. 1674–1679, 2023.

[80] *Ansys Granta EduPack | Software for Materials Education*. [Online]. Available: https://www.ansys.com/products/materials/granta-edupack#tab1-1.

[81] C. Kammer, "Aluminum and aluminum alloys," *Springer Handbook of Materials Data*, pp. 161–197, 2018.

[82] M. Köhler, S. Fiebig, J. Hensel, and K. Dilger, "Wire and arc additive manufacturing of aluminum components," *Metals*, vol. 9, no. 5, p. 608, 2019.

[83] T. Luijendijk, "Welding of dissimilar aluminium alloys," *Journal of Materials Processing Technology*, vol. 103, no. 1, pp. 29–35, 2000.

[84] S. Selvi, A. Vishvaksenan, and E. Rajasekar, "Cold metal transfer (cmt) technology-an overview," *Defence technology*, vol. 14, no. 1, pp. 28–44, 2018.

[85] *Fiji: Imagej*, https://imagej.net/software/fiji/.

[86] B. S. I. (2000), "Bs en 1011-4:2000 recommendations for welding of metallic materials - arc welding of aluminium and aluminium alloys," Tech. Rep.

[87] K. Svanberg, "The method of moving asymptotes—a new method for structural optimization," *International journal for numerical methods in engineering*, vol. 24, no. 2, pp. 359–373, 1987.

[88] *Artec studio 18*, https://www.artec3d.com/3d-software/artec-studio.

[89] M. Köhler, J. Hensel, and K. Dilger, "Effects of thermal cycling on wire and arc additive manufacturing of al-5356 components," *Metals*, vol. 10, no. 7, p. 952, 2020.

[90] K. S. Derekar, D. Griffiths, S. S. Joshi, *et al.*, "Influence of interlayer temperature on microstructure of 5183 aluminium alloy made by wire arc additive manufacturing," *International Journal of Microstructure and Materials Properties*, vol. 15, no. 4, pp. 267–286, 2020.

[91] K. König, M. Reis, M. Vielhaber, and A. Jung, "Application of ultraviolet (uv) radiation and fluorescence for dic measurements-quality improvement," *Optics and Lasers in Engineering*, vol. 158, p. 107 140, 2022.

[92] I. C. Solutions, "Digital image correlation: Overview of principles and software."

Appendices

A

Computational Experiments

This appendix chapter explains the computational experiments carried out to determine simulation parameters necessary to optimize the fabrication sequence which can be realized with the in-house Multi-axis WAAM setup. The simulation parameters are adjusted such that the resulting optimized fabrication sequence maintains constant thickness for all layers.

A.1. Weight Parameter Study in Fabrication Sequence Optimization

In the fabrication sequence optimization with uniform thickness, the objective function consists of two parts; the first minimizes the distortion and the second minimizes the thickness variation within the layers [23]. The uniform thickness part is controlled by a weighting factor, with high-value results in uniform material distribution with a tradeoff in distortion minimization as depicted in Fig.A.1.

(a) Obj: distortion = 1.0E-2
weight: 0.01

(b) Obj: distortion = 3.06E-2
weight: 1

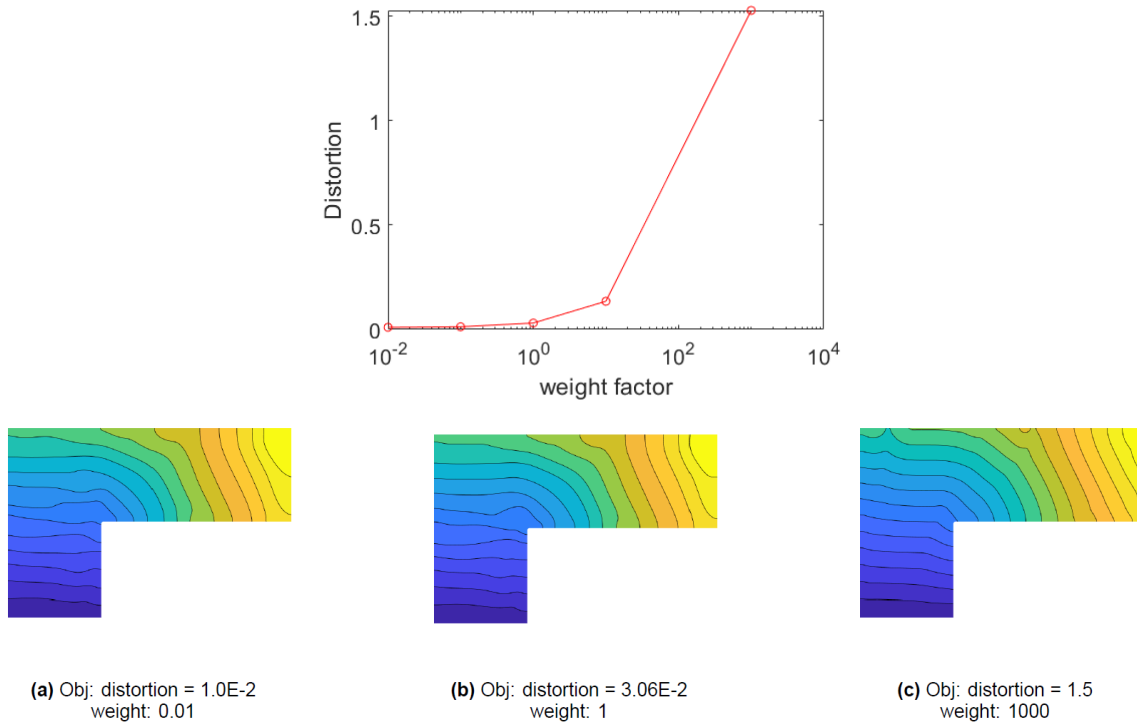**(c)** Obj: distortion = 1.5
weight: 1000

Figure A.1: Distortion values for varying weight factors [23]

From these results, it is clear that the weight factor has to be more than 1 in order to get a material distribution that can be realized with the in-house WAAM setup. For the 3D thin-walled shell structure, the side walls are

61

fabricated as per the optimized fabrication sequence. To get the optimized sequence with uniform thickness, the simulation experiments are carried out with a weight factor ranging from 25 to 1000.
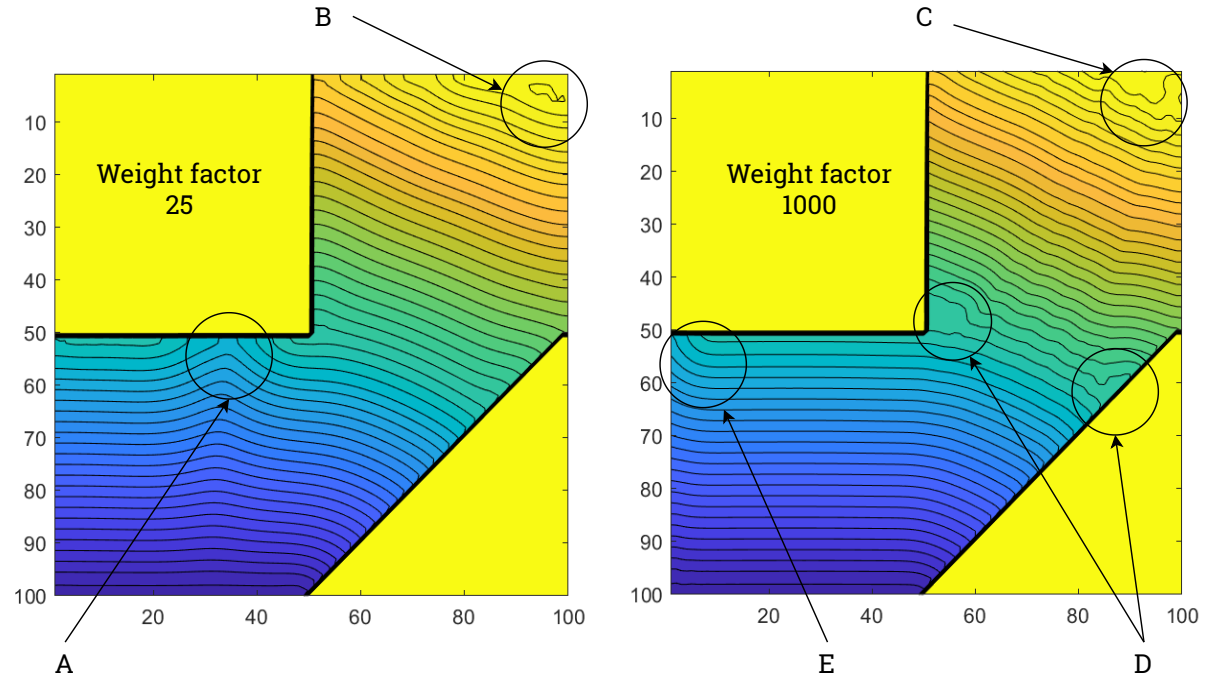

Figure A.2: Layer thickness variation for different weight factors with infeasible regions A to E

From Fig.A.2, it can be observed that several regions could not be fabricated in the optimized sequence with the in-house WAAM setup. When the weight factor is 25, region A consists of discontinuous layers, which means it will take more than the prescribed layers to fabricate the same structure also region B, gives an enclosed material distribution that is unrealistic. When the weight factor is set to a high value in this case 1000, the uniformity between layers is improved considerably. However, the objective function also minimizes distortion so with highly informed uniformity, the optimizer changed the layer orientation as shown by regions E and C. In region D, there is a significant layer thickness change which is impossible to fabricate using in-house WAAM. Considering the other results obtained with weighting factors 50, 100, 150, and 500, the optimized fabrication sequence with weighting factor 500 showed few infeasible regions and hence was used for the fabrication of 3D thin-walled shell structures.

WAAM Experiments

This appendix chapter contains supplementary information about available material choices, WAAM setup, and results of fabrication experiments performed in this research.

B.1. Materials and Available Choices

The material property chart or Ashby chart is plotted for the coefficient of thermal expansion and cost per kg during the material selection process in Ansys GrantaEdu Pack [80] as shown in Fig.B.1. This chart helps to visualize the suitable choices for the validation study of fabrication sequence optimization. This chart can be modified in the future to account for other mechanical/thermal properties along with practical aspects like cost.
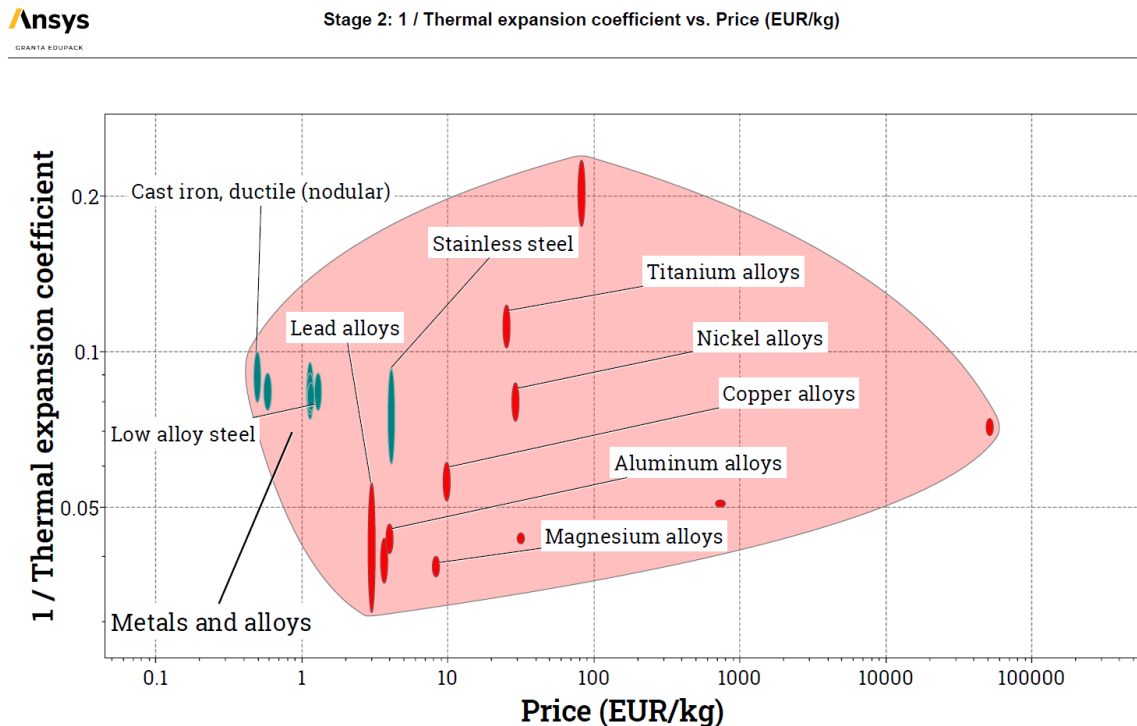

Figure B.1: Ashby plot for inverse CTE and cost for the material database in Ansys GrantaEdu Pack

The Al 5356 Aluminum Magnesium alloy wire is used for this research due to desired thermal properties, cost, and availability. However, there are a few other aluminum wire choices with similar properties that can be utilized as well, these options are tabulated in Table B.1.

Identification	ER1450	ER2319	ER4043	ER4047	ER5087	ER5180	ER5183	ER5356	ER5556	ER5754
Composition	Pure Al	AlCuMn 6% Cu	AlSi 5% Si	AlSi 10-13% Si	AlMg 4% Mg	AlZnMg 3.5-4.5 % Mg	AlMnMg 4.3-5 % Mg	AlMg 5% Mg	AlMg 5.1% Mg	AlMg 3% Mg
0.8	✓							✓		
Available 0.9	✓		✓	✓	✓		✓		✓	✓
Di- 1	✓	✓	✓					✓		
ame- 1.2	✓	✓	✓	✓	✓		✓	✓	✓	✓
ter 1.6	✓	✓	✓	✓	✓	✓	✓	✓	✓	✓
(mm) 2.4					✓		✓		✓	✓
3.2					✓		✓		✓	✓

Table B.1: Aluminum Alloy wires for WAAM
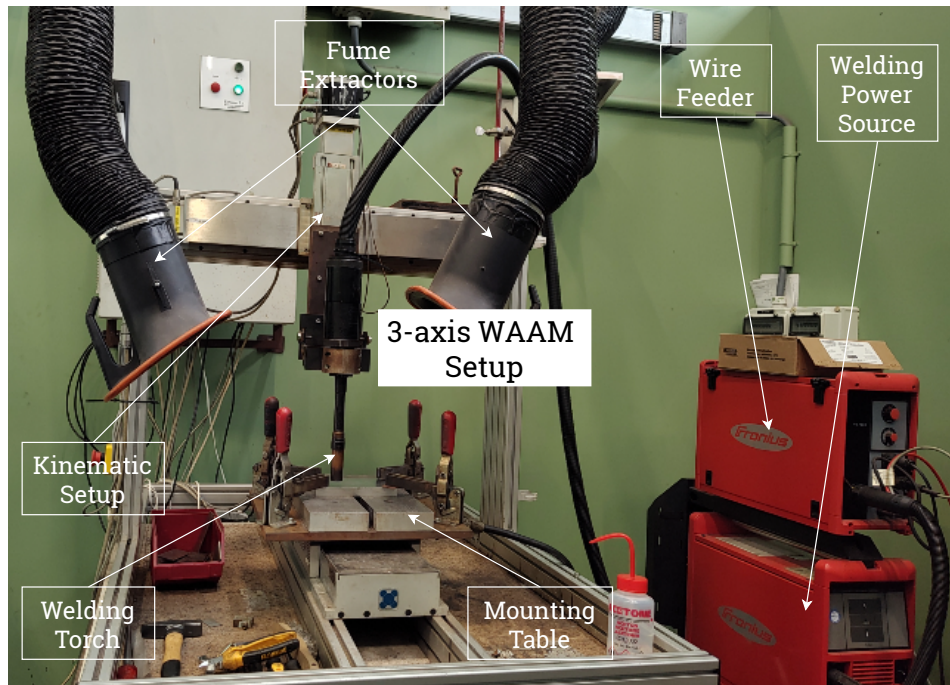
B.2. FABRICATION SETUP

Figure B.2: 3-axis Gantry Setup

A 3-axis gantry-based WAAM is used for fabrication experiments of single beads and single bead multi-layered wall structures. The gantry-based WAAM setup is shown in Fig.B.2. It consists of an advanced welding system manufactured by Fronius International GmbH. The welding setup includes the "TransPuls Synergic 5000 Remote" gas metal arc welding power source with a water-cooled welding torch and "VR 7000" wire feeder with a push mechanism. The welding torch is mounted on the gantry frame such that it has 2 translational degrees of freedom. The mounting table is also placed on the gantry frame allowing 1 translational degree of freedom. A 100% pure Argon is used for all the WAAM experiments.

For 3D thin-walled shell structures, a 6-axis robot-based WAAM system is employed. The kinematic setup comprises of 6-axis "M-710iC/12L" robot by FANUC with a fixed mounting table. with a provision of installing an additional 2 degrees of freedom manipulator instead of the fixed table. The welding torch is the end effector of the robot. The welding setup consists of a "TransPuls Synergic 3200 CMT R" welding power source with a water-cooled welding torch and a "VR 7000 CMT" wire feeder with a push-pull mechanism. The Welding setup is manufactured by Fronius International GmbH. For all WAAM experiments, 100 % Argon is
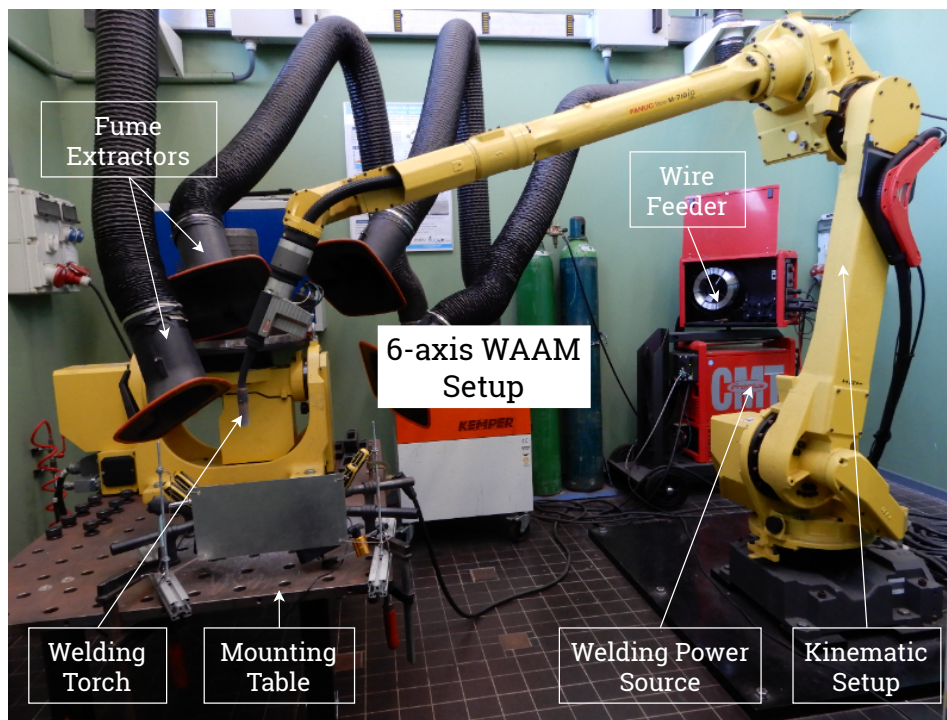
used as shielding gas.

Figure B.3: Pulsed Synergic Welding Program in TransPuls Synergic 3200 CMT R and TransPuls Synergic 5000 R welding source machines by Fronius International GmbH

For all WAAM experiments, Pulsed Synergic welding is used, in the TransPuls Synergic 3200 CMT R and TransPuls Synergic 5000 R welding setups this synergic welding adjusts the current and voltage according to the chosen filler wire and its diameter. For Al 5356, the filler wire option is AlMg5, therefore, in the welding controller the filler material is set to AlMg5, diameter is set to 1.2mm. The controller interface is shown in Fig.B.3.

B.3. Single Bead Experiments

Bead Geometric Data Measurement

Start						Middle						End						Avg		
Face one			Face two			Face one			Face two			Face one			Face two					
Width (mm)	Height (mm)	Area (mm2)	Width (mm)	Height (mm)	Area (mm2)	Width (mm)	Height (mm)	Area (mm2)	Width (mm)	Height (mm)	Area (mm2)	Width (mm)	Height (mm)	Area (mm2)	Width (mm)	Height (mm)	Area (mm2)	Avg Width (mm)	Avg Height (mm)	Avg Area (mm2)
8.08	3.938	26.28	8.704	4.376	32.037	6.201	4.169	21.447	5.947	4.196	20.892	5.886	4.165	20.026	6.011	3.911	19.679	6.80483	4.12583	23.3935
8.6	4.255	29.862	9.571	4.871	37.219	6.561	4.825	27.648	6.832	5.196	29.288	6.431	4.751	24.62	6.568	4.808	25.34	7.42717	4.78433	28.99616667
9.459	5.598	42.835	9.832	5.989	47.349	7.811	5.279	35.232	7.634	5.394	35.096	7.995	5.338	35.493	8.053	5.108	33.865	8.464	5.451	38.31166667
9.162	4.179	30.215	9.28	4.02	29.246	7.361	3.316	19.112	6.877	3.435	19.352	7.718	3.119	19.169	7.905	3.259	19.571	8.0505	3.55467	22.7775
10.226	4.269	34.892	10.228	4.068	31.583	7.671	3.398	21.067	8.071	3.5	21.403	8.031	3.589	21.795	8.067	3.5	21.626	8.71567	3.72067	25.39433333
10.691	4.604	39.974	10.003	4.482	35.196	8.35	4.046	26.935	8.333	3.966	26.508	8.698	3.809	25.295	8.635	3.842	26.078	9.11833	4.12483	29.99766667
9.131	4.067	29.923	9.853	4.163	30.191	9.757	3.515	24.33	9.994	3.593	23.537	10.064	3.569	23.568	10.036	3.303	22.902	9.80583	3.70167	25.74183333
10.367	4.307	36.053	10.63	4.451	37.29	11.058	3.862	27.752	10.946	3.759	26.74	11.365	3.454	26.349	11.352	3.48	27.175	10.953	3.8855	30.2265
10.801	4.51	40.019	11.019	4.796	41.423	12.882	3.945	35.148	12.836	3.89	34.176	13.415	3.343	31.819	13.852	3.298	32.268	12.4675	3.96367	35.80883333

Table B.2: Dimension measurements for 9 beads printed for shape analysis

C

MEASUREMENT AND DATA ACQUISITION

C.1. DIGITAL IMAGE CORRELATION

To capture and study the strain development during fabrication in situ non-contact type measurements are performed using Digital Image Correlation equipment by LIMESS GmbH. In digital image correlation, the movement of non-repetitive, isotropic, high-contrast pattern, so-called *"Speckle Pattern"* is traced throughout the deformation process, in this case during the deposition of the layers. Such a pattern is spray painted on the component in situ during fabrication as shown in Fig C.1.
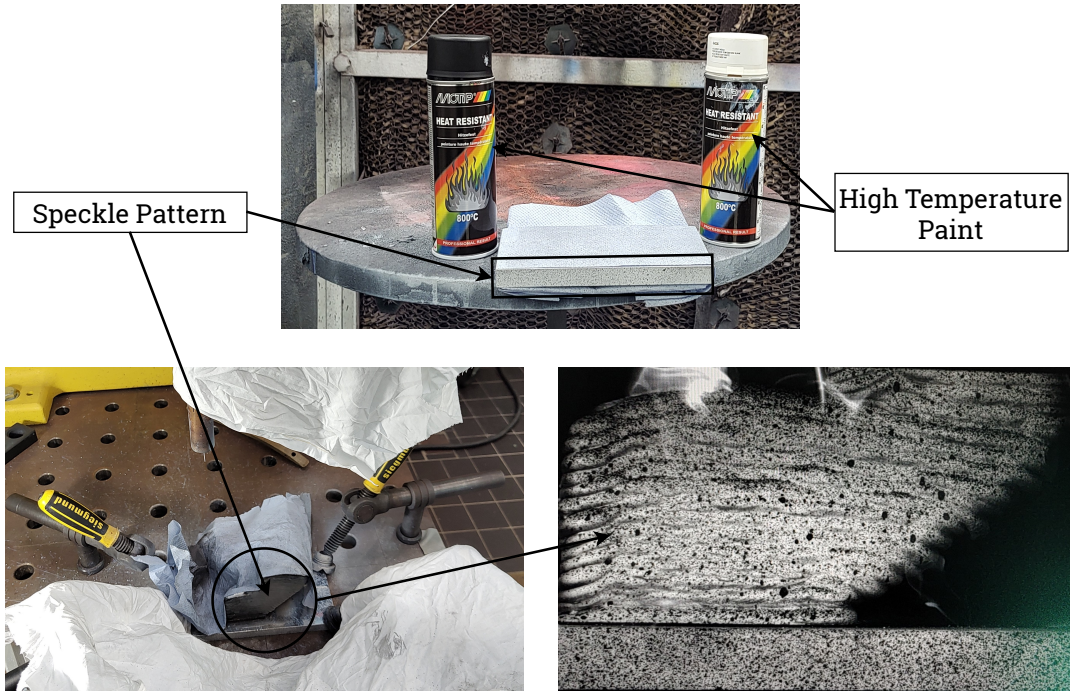

Figure C.1: Speckle Pattern Printing using High-Temperature Paint. Top Row: Pattern Printing on machined substrate, Bottom Row: In Situ Pattern Printing on Partly Fabricated Structure

To illustrate the tracking of the speckle pattern, consider a 9 x 9 binary image as illustrated in Fig. C.2 with a facet of size 5 x 5 pixels with a center point at (5,5). The correlation of this point along all points in the facet after a motion (u,v) is given by [92],

$$C(x, y, u, v) = \sum_{i,j=\frac{-n}{2}}^{\frac{n}{2}} \left(I(x+i, y+j) - I^{'}(x+u+i, y+v+j) \right)^2 \tag{C.1}$$

67

Where, x and y are the reference location of the pixel of interest inside of a facet of size nxn, u and v are displacement along x and y respectively, C are correlation functions, I and $I^{'}$ are image before and after motion respectively.
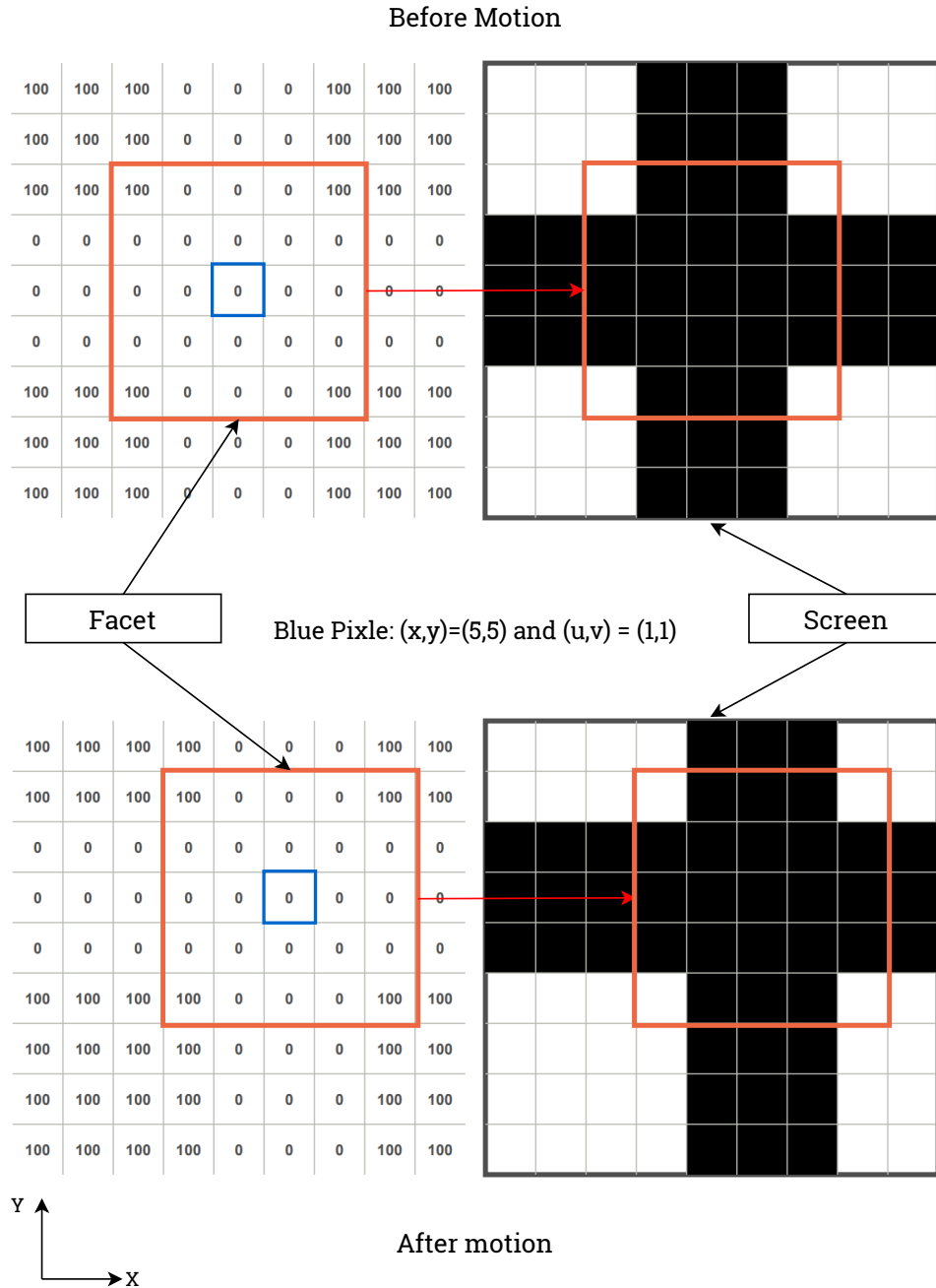
Figure C.2: Digital Image Correlation Basics [92]

C.1.1. DIC Measurement Procedure

The DIC system used in this research follows a systematic procedure targeting specific system characteristics at each step. The detailed steps are given as follows:

Step 1: Connect the camera to the data acquisition system and then connect the data acquisition system to the main computer. Then turn on the power for the entire system. Then open the DIC software, to create/open an existing repository to save all the files during measurement as well as post-processing.

Step 2: Adjust the camera such that the frame covers the entire measurement area, in this case, the substrate as well as the partly fabricated structure.

Step 3: Illuminate the measurement area using a single wavelength blue light source. On the camera, set the aperture to max resulting in an excessively bright picture on the computer screen.

Step 4: In the DIC software, run an auto shutter speed function, it will change the brightness of the image on the computer screen, however, the image may go out-of-focus, in that case, adjust the focus to get a sharp image with a clearly visible contrast in the speckle pattern.

Step 5: Once the image is in focus, change the aperture to min or a setting suitable for the required field of view based on the size of the measurement object. After changing the aperture, rerun the auto shutter speed function to get a sufficiently bright and visible image on the computer screen. With this, the camera brightness settings are applied correctly for accurate measurements.

Step 6: Select a calibration target such that when placed near the measurement object it is fully visible in the images on the computer. In the DIC software, run a calibration program. First, select the target by choosing among available options or by importing a new one. Based on the size of the target, camera brightness settings may need to be updated. With the correct brightness setting, now run the calibration tool. The calibration tool captures a series of images (usually 8) to calibrate the distance and orientation of the calibration drawing embedded in the target. On the computer screen, a counter shows how many images are captured. For a good calibration, change the orientation of the target for each image as shown in Fig.C.3.

Step 7: Once the calibration programs capture sufficient images, manually stop the calibration process to see the calibration results as shown in Fig.C.4. The global residual should be less than 0.1 as suggested by the manufacturer. If it is more than 0.1, then repeat step 6 to redo the calibration again else save the calibration file in the repository.

Step 8: After a successful calibration, the DIC system is ready for measurements. In the software open the measurement tab. In this tab, select the frame rate and total number of frames based on the desired measurement duration. The total number of frames is subjected to the hardware capabilities, in the system used for this research this limit is 4200 frames. Also, set the trigger settings to begin the recording during measurements.

Step 9: Once the recording and trigger settings are set. Press the trigger to start the recording. In the DIC software, there is no provision to stop the recording prior to capturing all frames defined in step 8, if stopped early the captured data is lost. The recording stops automatically after capturing all frames. There is a possibility to pause the recording in between the measurement process. Once the recording is finished, save all the frames in the repository by clicking the save button.

Step 10: Open the post-processing tab to start a new correlation study, load the captured frames, and select a reference frame among the captured frames, by default, the first frame is set as reference. Define the facet size and grid spacing, as a rule of thumb, facet size = $\frac{4}{3}$ grid spacing and each facet has evenly distributed multiple speckles. Define a region of interest/s by drawing polygon/s and assign a starting marker to each polygon. Now start the post-processing, depending on the facet size and number of facets the post-processing might take several hours to process.

Step 11: After the post-processing, open the visualization tab, select a suitable output among displacement/strain, etc. and the software will generate those measurements for the predefined region of interest/s for all frames with respect to the reference frame. The data can be exported in the form of individual frames or an AVI format video as well as a comma-separated value (CSV) file for reporting purposes.

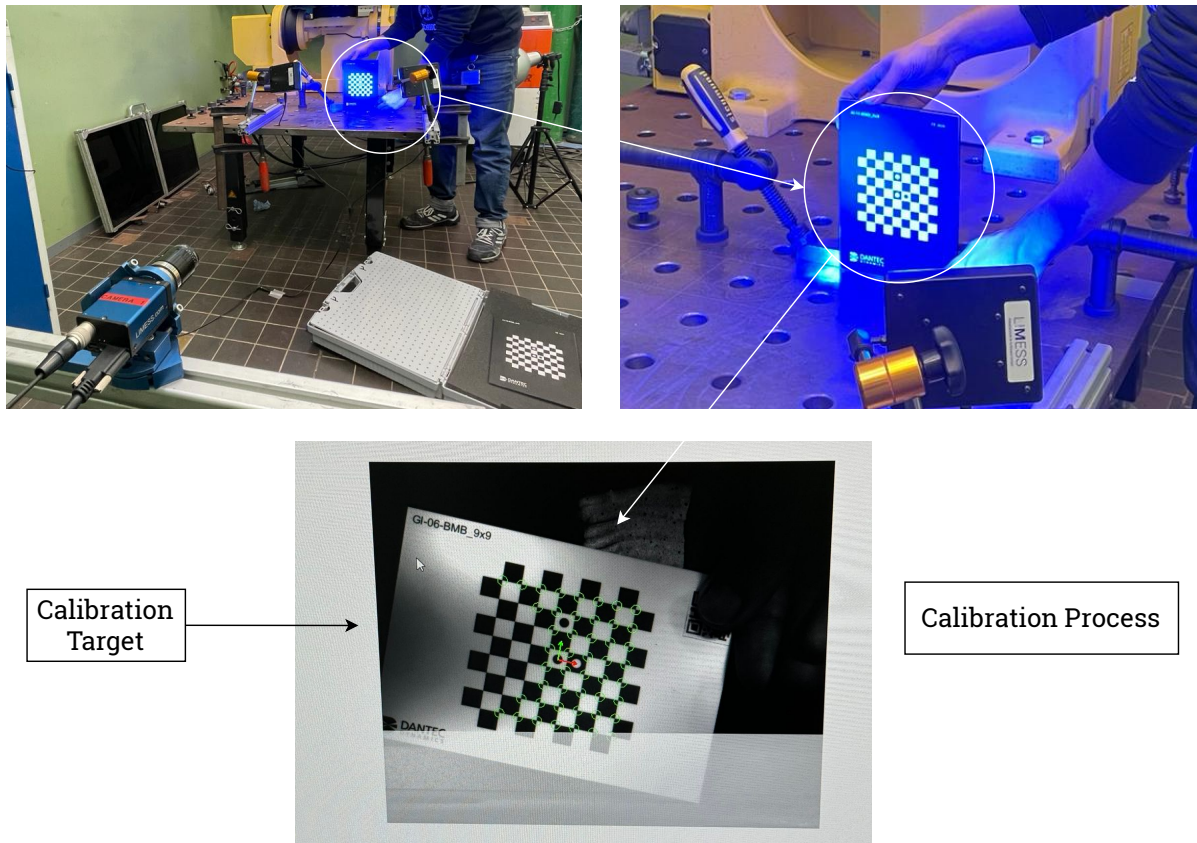During the post-processing, multiple correlation studies can be run from a single set of captured frames.

Calibration Target

Calibration Process
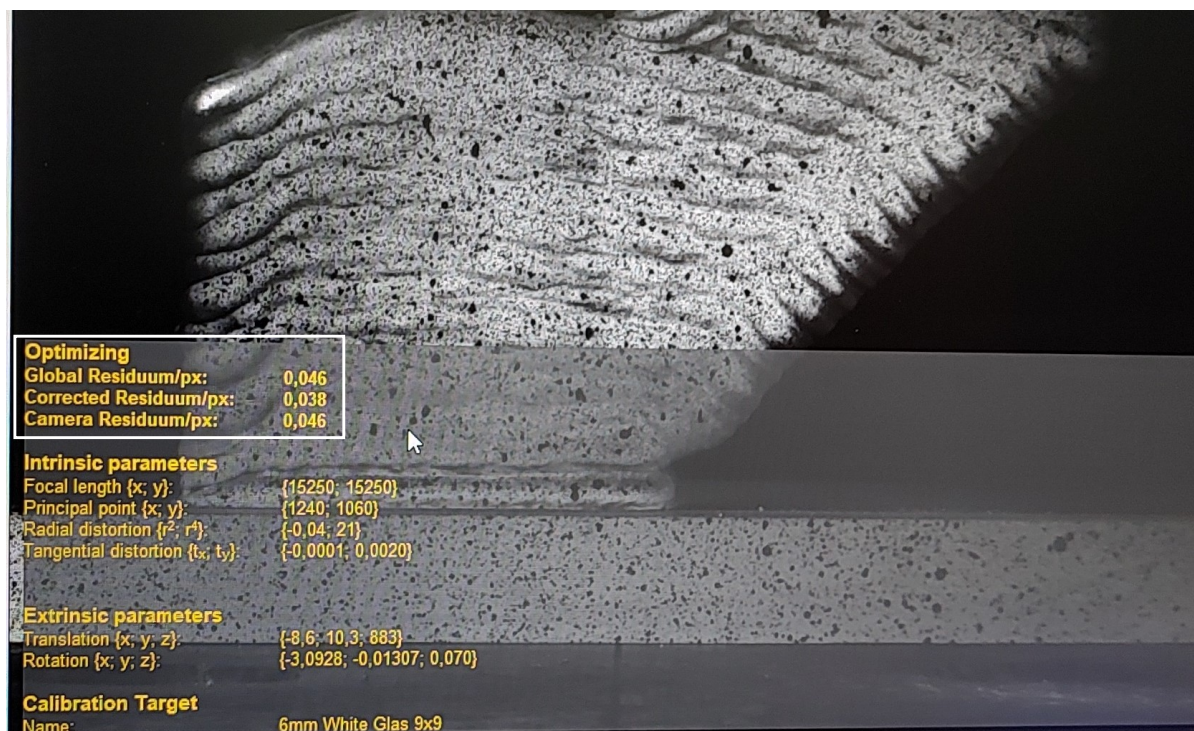
Figure C.3: DIC Calibration Process

Figure C.4: Residuam error values after calibration

C.1.2. 3D SCANNING

The 3D scanning process is relatively simpler than DIC measurements. However, there are several crucial steps that need to follow to generate a high-quality accurate 3D model of the scanned part. The Sample preparation is a crucial first step in this process. A part to be scanned should be free of dust, oil, or any other substance that can cause errors during scanning. Clean the part using a plastic/metal brush, then use compressed air to blow off dust/particulate matter from intricate features. Since the 3D scanner is based on optical scanning, the surface finish of the part to be scanned directly impacts the quality of the scanned model. A medium matt surface finish is proffered, however, for shiny surfaces like the aluminum WAAM parts in this case, an appropriate surface coating has to be applied before the scanning.

Unlike the DIC, the calibration of the 3D scanner need not be performed every time before scanning, however, it is recommended to calibrate the scanner before a set of new scanning procedures. The calibration process is simple, there is a standard calibration target, with a position template and mounting stand for the scanner as shown in Fig.C.5. In the software, there is a calibration tool, that guides the user to move the target at 14 pre-defined positions to capture the image for each target position. This pre-determined target orientation along with the fixed distance between target points is used to calibrate the spatial resolution of the optical scanner. The success or failure of the calibration is prompted by the software at the end process.
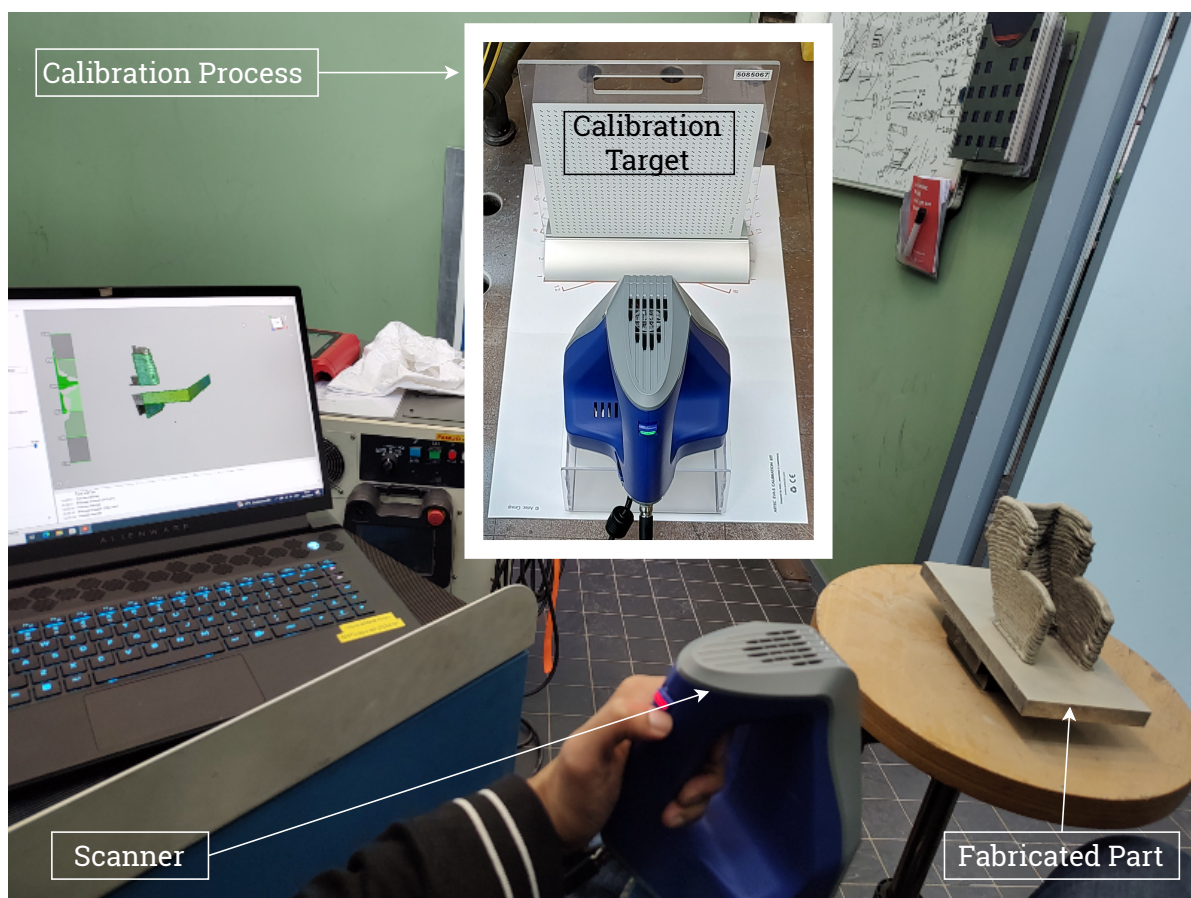

Figure C.5: 3D Scanning Process using Artec Space Spider Industrial 3D Scanner

With a calibrated scanner the scanning and model building consists of the following steps:

Step 1: Sample preparation: For the aluminum WAAM parts, evenly apply a special white powder coating to make sure that there are no reflecting shiny surfaces exposed.

Step 2: Connect the scanner to the computer and power up the scanner for at least 15 min to reach the optimal scanning temperature. Meanwhile, place the part on a rotating platform in a suitable orientation. Once the scanner is ready, trigger the scanner once to see the scanning preview in the software. Pay close attention to the distance scale in the software, the scale should show a red color if the scanner is kept

too close or too far from the part. A green color indicates the correct distance. if everything is green, trigger the scanner once again to start the scanning process. Rotate the table as well as the scanner to scan the complete part.

Step 3: Once the part is fully scanned with a sufficient number of frames, trigger the scanner to stop the scanning. Then in the software, check for the error if it is more than 0.5 then repeat the scanning.

Step 4: If the error is below 0.5, then change the orientation of the part and perform the scanning again. Based on the complexity of the part, repeat the scanning for different orientations covering all intricate features.

Step 5: After completing the scanning, turn off and discount the scanner. In the software, go to the post-processing section. Standard post-processing involves base removal for individual scans, aligning different scans to create the desired model, global registration of the aligned scan, followed by outlier removal, and final fusion of aligned scans. Usually, the fusion file consists of a large number of mesh and can take up a lot of memory, to tackle this it is possible to simply the mesh to a desired size using a mesh simplification tool.

Step 6: When the mesh is reduced without losing the model's accuracy, the mesh files can be converted into STL / Obj files that can be opened in most CAD software including SOLIDWORKS and Fusion 360 for further analysis.

SELF REFLECTION

The main objective of this research was to experimentally validate fabrication sequence optimization using multi-axis Wire Arc Additive Manufacturing (WAAM). Upon commencing the project, I realized the broad scope and the tricky material choice would require extensive preliminary work. Given that my research group primarily focused on computational design and mechanics rather than WAAM, I had to assume full responsibility for the project's success. This autonomy, while empowering, also meant that I had to meticulously plan and execute every aspect of the research, from literature review to initial experimentation. The autonomy allowed for significant creative freedom but also left ample room for error. One of the major technical hurdles was accurate temperature measurement. Contact-based methods were unsuitable, leading me to use an IR thermal camera. However, the reflective nature of the hot metal posed accuracy issues. To overcome this, I innovatively used deposited soot as a matt black surface with an emissivity of 0.9, which significantly improved measurement accuracy. Validation against thermocouple readings showed minimal error, demonstrating the efficacy of this approach. Additionally, designing the tool path for multi-axis WAAM involved empirical assumptions due to the ongoing development of the fabrication optimization code. The Digital Image Correlation (DIC) measurements required a disturbance-free setup, which I meticulously designed and implemented.

Resource management posed its own set of challenges, particularly since the lab facilities were shared with other students and researchers. I adeptly managed material procurement and scheduling to ensure uninterrupted experimentation, demonstrating effective foresight. Time management was another significant challenge due to personal health and financial issues. These problems impacted my academic progress, necessitating a proactive approach to balancing health, finances, and research responsibilities. Despite these obstacles, I was able to maintain a steady workflow and keep my project on track. Collaboration was crucial for my project. I coordinated with lab supervisors and professors for access to advanced WAAM facilities and received support from various departments, including material science, aerospace, and industrial engineering. This interdisciplinary collaboration enriched my research experience and facilitated the successful execution of complex tasks. Additionally, I provided support to a fellow master's student, fostering a collaborative and mutually beneficial research environment. These interactions not only enhanced my technical knowledge but also underscored the importance of effective communication and teamwork.

Throughout this journey, I learned and adapted continuously. I acquired skills in both contact and non-contact temperature measurement, DIC, WAAM coding, and troubleshooting minor hardware and software issues. Learning welding and successfully fabricating structures using aluminum on multi-axis WAAM were significant achievements, especially given my lack of prior experience in metal additive manufacturing. These accomplishments were highly rewarding and validated the extensive effort invested in the project. Reflecting on my journey, I made several mistakes but consistently corrected them through careful analysis and introspection. This iterative learning process was crucial for my development, teaching me that mistakes are an integral part of success. The experience supported the importance of structured problem-solving, effective time and resource management, and the value of seeking help when needed. This project has not only enhanced my technical skills but also solidified my interest in pursuing a Ph.D. in metal additive manufacturing. For future students embarking on similar projects, I recommend robust planning and proactive problem-solving. My resilience, shaped by personal challenges, enabled me to thrive under pressure. However, meticulous planning can help mitigate many issues and prevent delays. Engaging with peers and exchanging knowledge is invaluable, as collaborative efforts can significantly enhance the research experience. In conclusion, this research project was a transformative journey that honed my technical abilities, problem-solving skills, and resilience. The lessons learned and the achievements realized have laid a solid foundation for my future endeavors in the field of metal additive manufacturing.

Adhiraj Ravindra Pimpalkar
Delft, May 2024